



Universiteit
Leiden
The Netherlands

Nano-scale electronic structure of strongly correlated electron systems

Tromp, W.O.

Citation

Tromp, W. O. (2022, December 20). *Nano-scale electronic structure of strongly correlated electron systems*. *Casimir PhD Series*. Retrieved from <https://hdl.handle.net/1887/3503554>

Version: Publisher's Version

License: [Licence agreement concerning inclusion of doctoral thesis in the Institutional Repository of the University of Leiden](#)

Downloaded from: <https://hdl.handle.net/1887/3503554>

Note: To cite this publication please use the final published version (if applicable).

*Nano-Scale Electronic Structure of Strongly Correlated
Electron Systems*

Proefschrift

ter verkrijging van
de graad van doctor aan de Universiteit Leiden,
op gezag van rector magnificus prof.dr.ir. H. Bijl,
volgens besluit van het college voor promoties
te verdedigen op dinsdag 20 december 2022
klokke 12.30 uur

door

Willem Olivier Tromp

geboren te Hilversum
in 1994

Promotores:

Dr. M.P. Allan

Prof. dr. J. Aarts

Promotiecommissie:

Prof. dr. F. Baumberger

Prof. dr. N.E. Hussey

Dr. A. Grubisic-Cabo

Prof. dr. K.E. Schalm

Prof. dr. E.R. Eliel

Dr. S. Bhattacharyya

Université de Genève

Radboud Universiteit Nijmegen

Rijksuniversiteit Groningen



Universiteit
Leiden
The Netherlands



Casimir PhD series, Delft-Leiden 2022-37

ISBN 978-90-8593-547-6

An electronic version of this thesis can be found at

<https://openaccess.leidenuniv.nl>

Printed by Gildeprint - Enschede

This work is supported by the European Research Council (ERC StG SpinMelt) and by the Netherlands Organisation for Scientific Research (NWO) as part of the Frontiers of Nanoscience program (NanoFront).

Copyright © 2022 Willem Olivier Tromp

The cover depicts ripples in the Fermi sea caused by lattice defects, reminiscent of a stone thrown in a pond.

Contents

1	Introduction	1
1.1	Complexity in Strongly Correlated Electron Systems	2
1.2	Copper-Oxide Superconductors	3
1.3	Scanning Tunneling Microscopy	8
1.4	Outline of this Thesis	13
1.5	References	14
2	Direct Comparison of ARPES, STM, and Quantum Oscillation Data for Band Structure Determination in Sr_2RhO_4	19
2.1	Introduction	20
2.2.	Results & Discussions	21
2.2.1	<i>ARPES and QPI Fermi Surface</i>	21
2.2.2	<i>Shubnikov de Haas Oscillations</i>	22
2.2.3.	<i>Quasi-particle Dispersion</i>	26
2.2.4.	<i>Lifetime Analysis</i>	29
2.A	Appendix	33
2A.1	<i>Methods</i>	33
2A.1.1	<i>Sample Preparation</i>	33
2A.1.2	<i>Quantum Oscillations</i>	33
2A.1.3	<i>ARPES</i>	34
2A.2	<i>Supplementary Figures</i>	36
2.3	References	41
3	Puddle Formation, Persistent Gaps, and non-mean-field Breakdown of Superconductivity in Overdoped $(\text{Pb,Bi})_2\text{Sr}_2\text{CuO}_{6+\delta}$	45
3.1	Introduction	46
3.2.	Results & Discussions	47
3.2.1	<i>Gap Closure vs. Gap Filling</i>	48
3.2.2	<i>Persistent Superconducting Gap & Gap Filling</i>	50
3.2.3	<i>Cooper Pair Decay in a Metallic Matrix</i>	54
3.3	Conclusion & Outlook	56
3.A	Appendix	57
3A.1	<i>Experimental Methods</i>	57
3A.2	<i>The Phenomenological Model to fit Spectra</i>	58
3A.2.1	<i>The d-wave Gap Model</i>	58
3A.2.2	<i>Statistical Analysis with and without the Excluded Spectra</i>	58

3A.2.3	<i>Fit Parameters Fig. 3.2c</i>	61
3A.2.4	<i>Energy Range for Fitting and Approximations for the Normal Density of States</i>	62
3A.2.5	<i>An Alternative Model</i>	63
3A.3	<i>Temperature Dependence</i>	66
3A.4	<i>Intrinsic Metal-Induced Pair-Breaking Effects within a Superconducting Puddle Embedded in a Metallic Matrix</i>	66
3A.5	<i>Rigid Band Shift in Overdoped Bi2201</i>	73
3A.6	<i>Gap Filling and DOS from other Experiments</i>	74
3.4	References	76
4	Quasi-particle Interference in Overdoped $(\text{Pb,Bi})_2\text{Sr}_2\text{CuO}_{6+\delta}$: Application of Noise Suppression through Self-Supervised Machine Learning	81
4.1	Introduction	82
4.2	Methods	84
4.2.1	<i>QPI Measurements</i>	84
4.2.2	<i>Self-supervised Machine Learning for Noise Suppression</i>	84
4.3	Results	89
4.3.1	<i>Fermi Surface</i>	89
4.3.2	<i>Anti-nodal Dispersion</i>	91
4.4	Discussion	95
4.4.1	<i>Artifacts of Noise Suppression</i>	95
4.4.2	<i>Carrier Concentration and Bandshifts</i>	98
4.4.3	<i>Density Waves in Overdoped $\text{Bi}_2\text{Sr}_2\text{CuO}_{6+\delta}$</i>	99
4.5	Conclusion & Outlook	100
4.6	References	101
5	Hydrodynamic Transport Description of the Strongly Correlated Electron System Sr_2RuO_4	105
5.1	Introduction	106
5.2	Sr_2RuO_4 as a Hydrodynamic System: the Relevant Length Scales	109
5.3	Hydrodynamic Transport Simulations	112
5.3.1	<i>Momentum Diffusion in the Navier-Stokes Equation</i>	112
5.3.2	<i>COMSOL Implementation</i>	114
5.4	Hydrodynamic Transport in Sr_2RuO_4	117
5.4.1	<i>Negative Backflow Resistance</i>	117
5.4.2	<i>Boundary Effects: the Slip-length</i>	120
5.5	Towards Strange Metal Hydrodynamics	123
5.5.1	<i>Transport Parameters</i>	123
5.5.2	<i>Absence of Whirlpool Formation</i>	125

5A	Appendix	128
5.6	References	132
Summary		137
Samenvatting		141
Acknowledgements		145
Curriculum Vitae		147
List of publications		149

1 Introduction

1.1 Complexity in Strongly Correlated Electron Systems

1 One of the oldest questions in science, dating back to at least as far back as Leucippus & Democritus in the 5th century BCE¹, is “What is matter made of?”. This question has slowly morphed into a way of thinking, a method of tackling new problems: the reductionist approach. When faced with a system of unknown nature, physicists very naturally ask themselves what are the building blocks, in the hope that the properties of the building blocks easily translate into properties of the larger system. How those building blocks fit together, the glue that binds them, is often only a secondary consideration.

Perhaps no field of research embodies this approach as well as condensed matter physics. The building blocks here are the atoms forming the lattice, and the electrons moving through it. The approach of neglecting or heavily approximating the interactions between the building blocks is a necessity for an otherwise intractable problem. A centimetre sized piece of material is made up of 10^{23} atoms and electrons! Tracking every interaction among them is simply impossible. The field, therefore has a long history of approximations to deal with this problem, with successes some might call unreasonable. For example, even the Fermi gas, where the lattice is completely ignored together with any interaction between electrons, already has some of the essential features, such as a parabolic dispersion and a Fermi surface.

Departing from there each new interaction treated properly adds a new level of detail, but they all share a common theme: finding a particular angle to the problem so that the language of single particles still applies. For example, when treating the interactions between electrons and lattice vibrations, or phonons, one that the system still very much looks like free electrons, albeit with a modified dispersion relation for energies below the phonon frequency². This strategy forms the foundation of much of the field and its application, though particularly electron-electron interactions are more stubborn to this approach.

In recent years condensed matter physicists have started asking questions moving away from this approach, in part motivated by the challenges posed by electron-electron interactions. A question like “Where does complexity come from?”³⁻⁵ appears to be better suited for the category of systems scientists increasingly deal with, often called strongly correlated systems, where the

older approach no longer seems applicable. In these cases, the interactions, most commonly electron-electron interactions, are so dominant that the language of single electrons is no longer suitable. The physics of such a system are often emergent of collective phenomena, as they only appear when a large number of particles interact with each other. Properties of such systems can vary wildly, summarized beautifully by Philip Anderson: More is Different³. For example, electrons can freeze themselves in place in what should be a good metal⁶ (Mott insulators), single particles can seize existing altogether⁷ (strange metals), or the system shows behavior more associated with bosons⁸ (superconductivity) or something in between called anyons⁹.

One of the core concepts of condensed matter physics takes a rather peculiar place in this view: the quasi-particle. This concept is born from Landau's Fermi Liquid theory stating (rather simplified) that in the presence of interactions a system of electrons on a lattice can often be mapped back to a single particle physics of newly defined quasi-particles, provided the interactions aren't too strong. What those quasi-particles are depends on the exact system and nature of interactions. This is quite remarkable! The applicability of single particle physics extends farther than naively expected based on the number of particles involved. Still, this is not quite the victory for the reductionist approach as it seems, or perhaps just a surface level victory. Rather, the properties of a quasi-particle can be quite far removed from those of a regular electron. There is a whole zoo of quasi-particles that physicists have studied: plasmons, anyons, holons, basically anything ending with -on. It is this gap between regular electrons and quasi-particles, and the zoo of possible quasi-particles, where many-body physics most often shows itself and which a reductionist view often struggles to fill. In this sense, the quasi-particle itself is the emergent phenomenon. And yet there are limits to Fermi Liquid theory. For example, in the copper-oxide superconductors the concept of quasi-particles is certainly useful, but it doesn't cover the full story and sometimes seemingly does not even apply at all. Exactly how to understand and describe the copper-oxide superconductors is one of the major challenges of condensed matter physics.

1.2 Copper-Oxide Superconductors

One of the most notorious examples of emergent phenomena in condensed matter physics, and a primary subject of this thesis, are the copper oxide,

or cuprate, high-temperature superconductors. These superconductors are composed of alternating layers of CuO square lattices, where the charge carriers reside, and insulating buffer layers (see **Fig. 1.1a**). The electronic state underlying these compounds is a Mott insulator, itself a prime example of a system where interactions dominate the properties. The insulating state arises when the CuO square lattice, schematically shown in **Fig. 1.1b** has one carrier per unit cell, i.e. the lattice is half-filled. Without any interactions the half-filled square lattice would yield a metallic state. The cuprate superconductors however feature a strong on-site electron-electron repulsion, often called U , meaning that the presence of two electrons on a single lattice site is penalized by an energy cost U . This energy scale is in competition with the natural tendency of electrons to delocalize, parametrized by the hopping energy t . If the repulsion U is much stronger than the hopping term t the electrons are frozen in place, unable to leave their lattice site. The result is a strongly insulating state. Additionally, these electrons are arranged antiferromagnetically. This is the result of the Pauli principle adding an extra energy cost for virtual hopping events were the electrons to have a ferromagnetic alignment.

The seemingly odd choice to start a discussion of a compound family most famous for their superconductivity by discussing a strongly insulating state is a sign for things to come when we dope the Mott insulating state (for the purposes of this thesis hole-dope specifically). The insulating state quickly melts with doping, and superconductivity emerges (see **Fig. 1.2a**). One important feature of the superconducting state is its d-wave symmetry⁷, meaning the wavefunction flips sign upon 90 degree rotation. As a result, the superconducting gap has nodes where it goes to zero, lying on the diagonals in k-space. This splits k-space into two regions (**Fig. 1.2b**): the nodal direction in the neighborhood of the diagonals, and the anti-nodes near the Brillouin zone edges $k = (\pm\pi/a, 0)$ and $k = (0, \pm\pi/a)$. Another important feature of cuprates is the strong spatial inhomogeneity of the electronic state. This can be attributed to Mott physics still being at play, despite the insulating state being suppressed. From this emerges a disposition towards phase separation and the emergence of multiple ordered states on extremely short length scales.

In the region of the phase diagram where T_c is increasing with doping, called the *underdoped* regime, the system is dominated by another salient feature called the pseudogap. This phase features a partial gap, with anti-nodal states being strongly suppressed. As a result, there is no conventional Fermi surface:

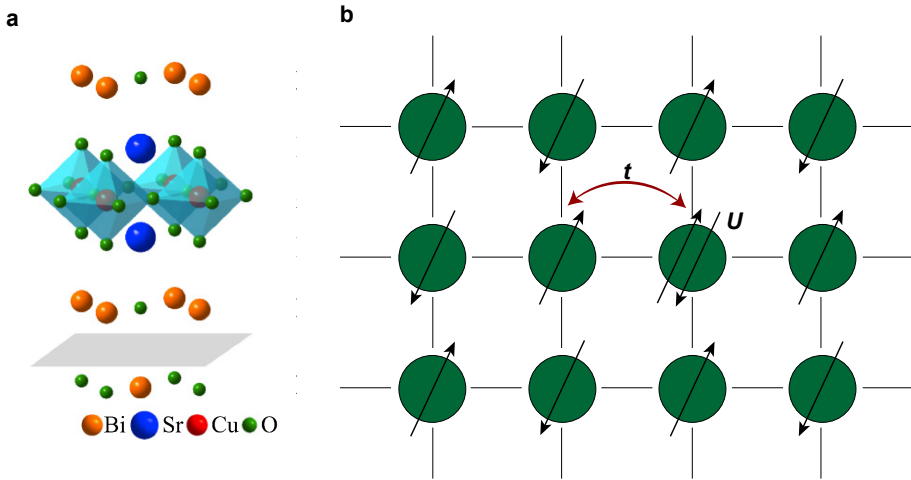


Figure 1.1: Cuprate unit cell.

a) The unit cell of the cuprate superconductor $\text{Bi}_2\text{Sr}_2\text{CuO}_{6+\delta}$ (Bi2201), subject of Chapters 3 & 4. The charge carriers reside in the CuO planes, while the BiO and SrO planes act as insulating buffer layers hosting the dopants. Image adapted from Ref.10. **b)** Schematic of a Mott insulator, showing one electron per unit cell with spins aligned antiferromagnetically. When the energy cost of a doubly occupied lattice site U is larger than the hopping energy t the system turns insulating.

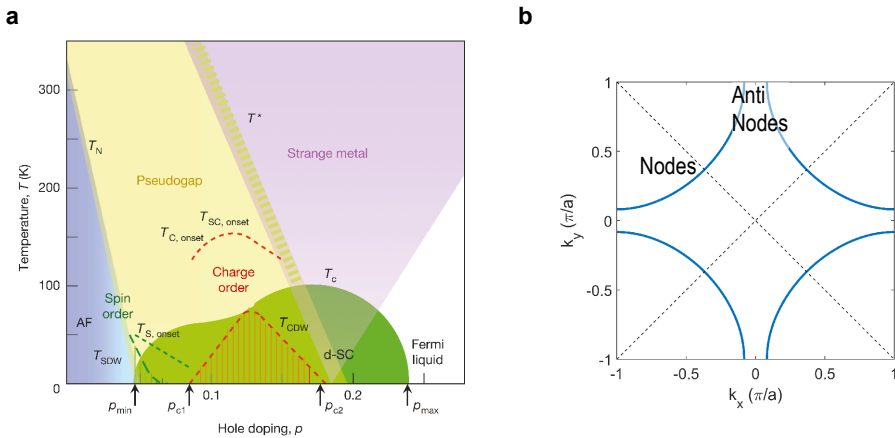


Figure 1.2 Electronic phases of cuprate.

a) Phase diagram of the many different electronic phases cuprates have been shown to host. Image adapted from Ref. 7. **b)** Sketch of the cuprate Fermi surface. The Brillouin zone diagonals (dashed lines) divide the Fermi surface in two parts: the nodal region, where the gap function goes to zero, and the anti-nodal region, where the gap function reaches its maximum.

near the anti-nodes there are no discernable quasiparticles in spectroscopy¹¹⁻¹³, while near the nodes there are still quasiparticles present at E_F . When looking at the Fermi level with momentum resolved spectroscopy, one finds four sets of disconnected states near the nodes called Fermi arcs. Complicating matters further, this phase also features a multitude of different ordered phases¹⁴⁻¹⁹ and possibly precursor pairing, where Cooper pairs have already formed but have not yet condensed into a single state²⁰⁻²³. How all of the pieces of puzzle fit together is still unknown, leaving the nature of the pseudogap state still an open question.

At a doping level of 16% (referred to as optimal doping) the T_c reaches a maximum. In this regime the pseudogap state gives way to a perhaps even more poorly understood state. This is the so-called strange metal phase. It is characterized by a linear in temperature resistivity over the full range spanning from T_c to the highest measured temperatures^{24,25}. This particular temperature dependence is present over a broad doping range, even at low temperatures^{26,27}. This is in contrast to quantum critical behavior, where this phenomenology would reduce down to a single doping point at zero temperature²⁸. Perhaps the strangest features of this state is that it seems to no longer feature coherent quasi-particles^{29,30}. Instead, charge is carried by a fully incoherent fluid. One framework to model this state is based around the AdS/CFT correspondence from string theory^{7,31,32}. With this correspondence a class of quantum theories (so-called conformal field theories, or CFTs) can be mapped onto a gravitational problem of a particular geometry (problems in an anti de sitter space, or AdS) in one higher spatial dimension. The metallic states emerging from this construction share some similarities with the strange metal behavior found in the cuprates. A particularly interesting prediction is that transport in this state features hydrodynamic flow as opposed to the ohmic transport of regular metals³³⁻³⁵. Additionally, the incoherent fluid is proposed to have an extremely low viscosity, raising the possibility of turbulent flow even on the nanometer scale. This is all despite the high levels of disorder cuprates are known to have³⁵.

When increasing the doping level even further into the overdoped regime, the T_c drops again. At some point a Fermi liquid metallic state is recovered, as is evidenced by the visibility of a full Fermi surface in spectroscopy^{11,30,36,37} and the observation of quantum oscillations^{38,39}. The reversion back to a more conventional Fermi liquid is not without its own mysteries however. For example, signs of incoherent carriers associated with the strange metal phase

have been found even when T_c has dropped to nearly zero²⁷. Furthermore, the decrease of T_c also features a drop of the number of condensed carriers, the superfluid density⁴⁰⁻⁴². In more regular superconductors, the superfluid density scales with the total number of carriers in the system. This means that as the doping increases, i.e. more carriers are introduced, the superfluid density should go up, whereas the exact opposite is found to occur in the cuprates. Instead, an increasingly large number of uncondensed carriers emerge with overdoping⁴³⁻⁴⁵. Furthermore, signs of fluctuating superconductivity above T_c have been seen through the persistence of a gap above T_c ⁴⁶⁻⁴⁸ and through AC and DC transport signatures^{22,49}. An important role in these phenomena is played by disorder^{50,51}, which naturally increases as more dopants are introduced in the overdoped regime.

One proposal to explain these observations involving disorder is the formation of a granular superconductor^{52,53}. In such a system superconducting islands are separated by metallic regions. A key ingredient of this proposal is enhanced anti-nodal scattering due to a Van Hove singularity (vHS) close to Fermi level at the anti-nodes. Neighboring anti-nodes have opposite sign due to the d-wave symmetry. This particular type of scattering therefore breaks Cooper pairs. The presence of the Van Hove singularity enhances this scattering to the point it locally breaks down superconductivity all together, leaving behind a metallic region. The existence of the metallic regions would explain the anomalously low superfluid and uncondensed carriers, as parts of the system is not superconducting at all. The superconducting regions of the system become more dilute with increased doping. At some point, the macroscopic properties of the system are no longer a consequence the properties of the wavefunction within a single region, but rather a consequence of the coupling of these regions to each other. Finally, when the coupling becomes sufficiently weak, or when the superconducting islands become sufficiently dilute, macroscopic superconductivity has vanished. Some traces of superconductivity may however still remain in this otherwise metallic state.

Complicating this proposal, or the breakdown of overdoped superconductivity in general, are observations of additional ordered states, specifically ferromagnetic fluctuations^{54,55} and charge order near the edge of the superconducting dome⁵⁶⁻⁵⁸. The latter is of particular interest as it has only been observed for doping levels around the level where superconductivity vanishes altogether. Additionally, the wavelength observed in real space

suggests a close tie to the vHS which exists near the Fermi level in the same doping range. It should be noted however that RIXS experiments disagree on the charge order wavelength⁵⁷, and, while visible in real space, STM results find no clear feature in momentum space⁵⁸. How this relates to the breakdown of superconductivity remains an open question.

1.3 Scanning Tunneling Microscopy

A common feature of strongly correlated electron systems is their nanoscale electronic inhomogeneity⁵⁹⁻⁶¹. A careful study of these systems therefore requires an accurate mapping of their real space electronic structure on an atomic scale. It is for this purpose that scanning tunneling microscopy, or STM, is invented⁶².

The principle of operation for STM is quantum tunneling of electrons between the sample and an atomically sharp tip used to study it⁶³. When the two are brought together sufficiently close to each other (typically meaning less than a nm) and a voltage is applied between them, called the bias voltage, electrons can jump between them without them being in physical contact (see **Fig. 1.3a**). The current that starts to flow as a result can be used to both image the surface of the sample, and measure the DOS directly below the tip.

The bias voltage shifts the Fermi levels of the tip and sample with respect to each other (**Fig 1.3b**) so that electron move from the occupied states on one side to the unoccupied states on the other (which side is which depends on the sign of the applied voltage). The resulting current is then given by the overlap of the occupied DOS on one side and the unoccupied DOS on the other:

$$I(V_b) = \frac{4\pi e}{\hbar} \int_{-\infty}^{+\infty} |M|^2 g_t(\epsilon - eV_b) g_s(\epsilon) [f(\epsilon) - f(\epsilon - eV_b)] d\epsilon \quad (1.1)$$

Where $g_{t,s}$ denotes the density of states of the tip and the sample, f the Fermi-Dirac distribution, V_b the bias voltage, and M the tunneling matrix elements controlled by the details of the tunneling process. Often, simplifications can be made to this equation by assuming the density of states of the tip to be constant in energy (as can be done by choosing the appropriate material for the STM tip), and the Fermi-Dirac functions to be step-functions. The latter is only valid at low temperatures, a point we will come back to when

discussing tunneling spectroscopy and energy resolution. Doing this reduces the expression for the tunneling current to:

$$I(V_b) \propto \frac{4\pi e}{\hbar} g_t |M|^2 \int_0^{eV_b} g_s(\epsilon) d\epsilon \quad (1.2)$$

Where the step-function shape of the Fermi-Dirac distribution was used to change the integration bounds. For simplicity's sake M is also assumed to be constant in energy. The matrix elements M are largely determined by the overlap of the orbitals of the tip and the sample, which is often energy independent. The orbital overlap decays exponentially with the distance z between tip and sample, meaning the tunneling current is extremely sensitive to the distance between tip and sample. This distance is controlled by a feedback mechanism. The tunneling current is constantly recorded and the tip height constantly adjusted so that the current stays constant. When the tip is moved across the surface, an image of the surface is reconstructed by recording the changes in the tip height needed to keep the current constant. Despite the feedback loop, STM is still extremely sensitive to outside influences disturbing the tip-sample distance, such as vibrations or sound waves. New STM setups are continuously being developed to minimize outside disturbances, with

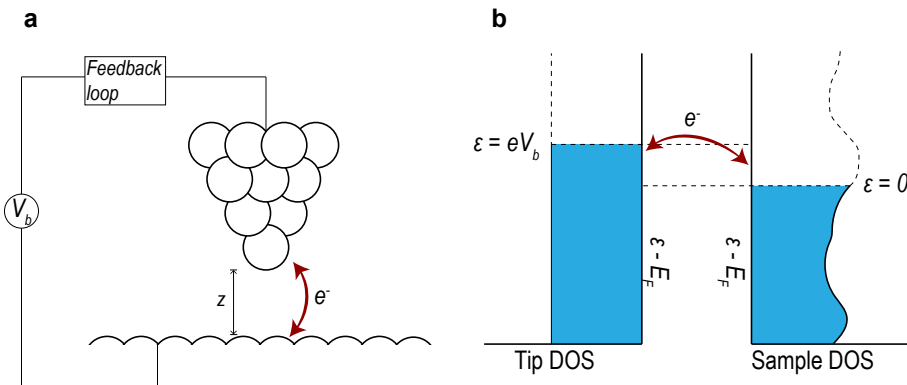


Figure 1.3 Basics of STM.

a) Schematic of the tip-sample system for STM. At sufficiently close distance z between tip and sample, regulated via the feedback loop, electrons can jump the gap when a bias voltage V_b is applied. **b)** Diagram of the DOS on the tip and sample sides. Current can flow between the tip and the sample when electrons can jump from occupied states on one side (here the tip) to unoccupied sides on the other side (here the sample). The total current is proportional to the size of the tunneling window given by eV_b and the total number of states inside said window.

the state-of-the-art system used for the majority of this thesis' experiments reaching a vibration level⁶⁴ as low as 6 fm Hz^{-1/2}.

Accessing the DOS of the sample, i.e. doing tunneling spectroscopy, is done by taking the derivative of eq. 1.2 with respect to the bias voltage V_b . This yields the following expression:

$$\frac{\partial I}{\partial V_b}(V_b) = \frac{4\pi e}{\hbar} |M|^2 g_t g_s(\epsilon V_b) \quad (1.3)$$

Measuring this quantity as a function of V_b is called a dI/dV spectrum, giving direct information about the local DOS (or LDOS) of the sample. To do this, the tip position above the sample is stabilized using the feedback loop at a current I_s and voltage V_s called the setup current and voltage. The feedback is then switched off and the bias voltage is swept while recording the tunneling current. The dI/dV could of course then be calculated through numerical differentiation. Doing so however enhances the noise in a spectrum. Instead, the dI/dV is directly measured by adding a small modulation ΔV at a given frequency to the bias voltage, and measuring the resulting oscillations ΔI at that frequency using a lock-in amplifier. The ratio $\Delta I/\Delta V$ gives then the DOS in a window ΔV around V_b . After the sweep is finished the feedback is enabled again so the tip can safely be moved to another location.

All of the above is combined into a single technique called Scanning Tunneling Spectroscopy (STS, although spectroscopic imaging STM or SI-STM is also used). Here, a finely spaced grid of 10^4 - 10^5 points or pixels is defined on a small section of sample surface (in the range of 10×10 nm). At each point both the tip height and the LDOS are measured by first stabilizing the tip position with feedback on and then measuring the dI/dV . As such, a 2D map of the surface is created simultaneously with a 3D map of the electronic structure, where the third dimension are the energies at which the LDOS was measured. The ability to measure the electronic structure with such a high spatial resolution is especially well suited for studying strongly correlated systems which naturally tend to inhomogeneous electronic structures.

The energy resolution of spectroscopic imaging is largely set by how the approximation of Fermi-Dirac distributions as step-functions works. Going through the derivation more carefully, one finds that the expression for dI/dV contains a derivative of the Fermi-Dirac distribution, which is a Gaussian with

a FWHM of $3.53k_bT$. Furthermore, the modulation used to measure dI/dV adds its own resolution given by the amplitude of the modulation. These two values add quadratically to give the total resolution. For example at a temperature of 4.2K and a modulation of 1.5mV, the total resolution is 2.58meV.

While STS is most often used to image the real space electronic structure, it can also measure a momentum resolved structure with a technique called Quasi-Particle Interference or QPI. This technique makes use of the standing waves around impurities or defects in the material that STS can observe^{65,66}, caused by electrons scattering off the defects (see Fig. 1.4a for a simulation) An

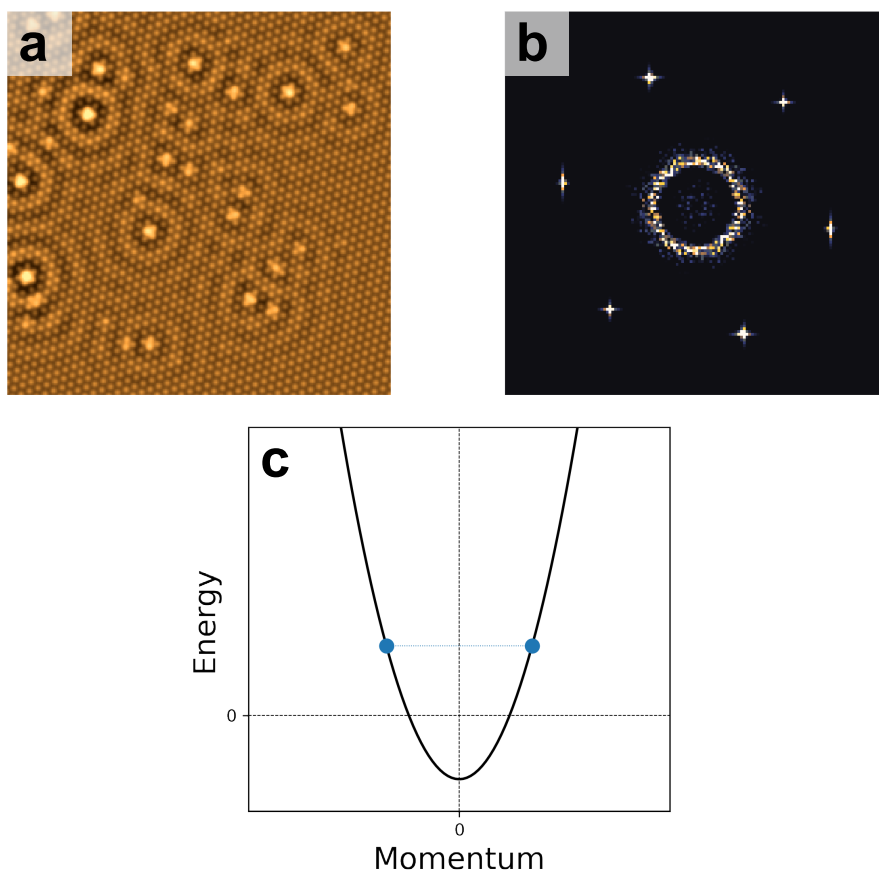


Figure 1.4 Basics of QPI.

a) Simulation of a Cu(111) lattice with defects showing QPI rings from electron interference. b) Fourier transform of a) clearly showing 6 isolated Bragg peaks from the lattice and the a ring-shaped feature from the QPI waves. c) The wavevector of the QPI waves, and with it the size of the ring in b), is determined by bandstructure (here parabolic) of the system. The blue dots show the momentum of the carriers at the energy used for a,b). Credit: K. Fujita.

incoming electron with momentum \mathbf{k}_1 and energy $\varepsilon(\mathbf{k}_1)$ will scatter into a final state with momentum \mathbf{k}_2 and energy $\varepsilon(\mathbf{k}_2) = \varepsilon(\mathbf{k}_1)$. The interference between these states causes an oscillation in the DOS with a wavevector $\mathbf{q} = \mathbf{k}_1 - \mathbf{k}_2$. The value of the wavevector \mathbf{q} can be measured by imaging the oscillation pattern in real space and taking a Fourier transform.

For the case that the system has a only a single band electrons will simply scatter from one side of the Fermi surface to the other: $\mathbf{q} = \mathbf{k}_F - (-\mathbf{k}_F) = 2\mathbf{k}_F$. Measuring \mathbf{q} as a function of energy then directly yields the bandstructure of the material (see **Fig. 1.4b, c**). For multiband systems, the situation is more complicated. Not only are there multiple values for $\mathbf{q} = 2\mathbf{k}_F$, one for each band, but also multiple different \mathbf{q} 's resulting from interband scattering. While in principle tracking the dispersions of these scattering vectors contains all the information on the bandstructure, extracting the exact dispersion is often impossible without some prior knowledge of the bandstructure. More generally, QPI will measure the scattering vector between states with a high joint density of states (JDOS). These are often states whose constant energy contours are parallel^{67,68} or parts of the bandstructure which feature a flat dispersion which increases the DOS, a useful fact for determining gapped bandstructures^{69,70}.

Viewing QPI through the lens of the JDOS gives a way to better approximate what a QPI measurement will look like. To do this, it is most useful not to think in terms of DOS but of the spectral function $A(\mathbf{k}, \omega)$. This quantity is a generalized version of the DOS suitable for correlated systems, giving the probability there is a quasi-particle excitation with momentum \mathbf{k} and energy ω ⁷¹. The JDOS is then well approximated by:

$$JDOS(\mathbf{q}, \omega) = \int A(\mathbf{k}, \omega) A(\mathbf{k} + \mathbf{q}, \omega) d\mathbf{k} \quad (1.4)$$

Although simple, this allows for quick estimation of QPI measurements, especially given the fact that the spectral function $A(\mathbf{k}, \omega)$ for occupied states is directly accessible in ARPES measurements⁷². By taking the autocorrelation of constant energy ARPES measurements, or results from the computational method for bandstructure of choice, a good first guess for the QPI signal is obtained. Of course more complicated, and more precise, methods to calculate QPI patterns exist^{67,73}, but the autocorrelation method is often good enough to identify the visible scattering vectors without the need of any further aids.

High quality QPI measurements push the technique of STS to its limits, primarily due to the length of such a measurement. The field of view used needs to be large enough, as this directly sets the resolution in q . Still, the spectroscopy grid needs to be fine enough to resolve features with higher q . Preferably, the atomic lattice is still resolved, as the subsequent Bragg peaks in the QPI signal are ideal for calibrating lengths of scattering vectors. Lastly, the signal-to-noise ratio of each spectrum needs to be sufficient so that the oscillations in the LDOS are not washed out. The result is that QPI measurements take a long time, the ones presented in this thesis often taking 2-3 days, occasionally up to 5 days. As such, stability of the STM setup is paramount, both in terms of temperature stability and vibration isolation.

Even when these issues are properly addressed, QPI measurements are prone to artifacts, the most important of which is the setup effect^{74,75}. This is a direct consequence of the choice to enable the feedback loop again after measuring each dI/dV spectrum. This introduces a normalization factor into the spectrum, which can be thought of as a 'leak' of the signal at the setup bias into the signal at other bias levels. For QPI measurements, this results in a constant-in- q , or non-dispersive, signal in the measurement⁷⁵. The exact shape and position of the artifact depends on what the visible q -vector is at the setup bias. Armed with this knowledge, it is in principle possible to design the QPI measurement in such a way that there is no setup effect present, although this can require impractical values for the setup bias.

1.4 Outline of this Thesis

In this thesis we will closely examine how we study strongly correlated systems, and apply that knowledge to the study of cuprate superconductors. Finally, we propose new experiments to explore the properties of strongly correlated systems. This thesis is structured as follows:

In Chapter 2 we study how electronic structures are determined by studying a prototypical example of a correlated 2D Fermi Liquid, Sr_2RhO_4 . We do this by applying three commonly used spectroscopic techniques, STS, ARPES, and quantum oscillations, and find them to be in good agreement. We argue that discrepancies between these methods in other systems are a reflection of the physics of those systems.

In Chapters 3 & 4, we study the electronic structure of the overdoped cuprate $(\text{Pb,Bi})_2\text{Sr}_2\text{CuO}_{6+\delta}$ both in real space and in momentum space, using STS and QPI measurements. In Chapter 3, we study the real space structure by tracking the evolution of the superconducting gap across and beyond the superconducting dome. We find that the magnitude of the spectroscopic gap no longer follows the superconducting dome, and instead levels out. Furthermore, we find that a metallic matrix forms and grows with increasing doping on the nm scale in this system, and that the mechanism of pair breaking in this system falls outside the scope of mean field theories. In Chapter 4 we employ a combination of QPI and state-of-the-art machine learning noise suppression to probe the momentum space structure of $(\text{Pb,Bi})_2\text{Sr}_2\text{CuO}_{6+\delta}$. We find an anti-nodal band rigidly shifting with doping, in line with earlier results. We also observe the bending of the band due to the gap and find shoulder-like features near the gap edge suggesting the presence of an additional density wave in these samples.

Finally, in Chapter 5 we discuss how strong correlations between electrons can give rise to a rare form of transport called hydrodynamic transport. We model the transport behavior in this regime for an experiment designed to detect hydrodynamic transport using the Navier-Stokes equation modified to include disorder effects. We carefully calculate the expected signal for this experiment for the Fermi Liquid normal state of the unconventional superconductor Sr_2RuO_4 , and find a crossover between Ohmic and hydrodynamic transport over a range of disorder levels. Finally, we discuss the application of this experiment to the cuprate strange metal phase, which has been proposed to show hydrodynamical behavior with an extremely low viscosity. We show that the same experiment will show only Ohmic behavior due to the combination of disorder and low viscosity in cuprate strange metals.

1.5 References

- [1] Berryman, S. Democritus, in *The Stanford Encyclopedia of Philosophy*. (Metaphysics Research Lab, Stanford University, 2016).
- [2] Ashcroft, N. W. & Mermin, N. D. *Solid State Physics*. (Brooks/Cole, Cengage Learning, 1976).
- [3] P. W. Anderson, More is Different. *Science* **177**, 393–396 (1972).
- [4] Laughlin, R. B. & Pines, D. The Theory of Everything. *Proc. Natl. Acad. Sci.* **97**, 28–31 (1999).

- [5] Elbio, D. Complexity in Strongly Correlated Systems. *Science* **309**, 257–262 (2005).
- [6] Imada, M., Fujimori, A. & Tokura, Y. Metal-insulator transitions. *Rev. Mod. Phys.* **70**, 1039–1263 (1998).
- [7] Keimer, B., Kivelson, S. A., Norman, M. R., Uchida, S. & Zaanen, J. From quantum matter to high-temperature superconductivity in copper oxides. *Nature* **518**, 179–186 (2015).
- [8] Bardeen, J., Cooper, L. N. & Schrieffer, J. R. Theory of Superconductivity. *Phys. Rev.* **108**, 1175–1204, (1957).
- [9] Nakamura, J., Liang, S., Gardner, G. C. & Manfra, M. J. Direct observation of anyonic braiding statistics. *Nat. Phys.* **16**, 931–936 (2020).
- [10] Lv, Y. F. *et al.* Electronic structure of the ingredient planes of the cuprate superconductor $\text{Bi}_2\text{Sr}_2\text{CuO}_{6+\delta}$: A comparison study with $\text{Bi}_2\text{Sr}_2\text{CaCu}_2\text{O}_{8+\delta}$. *Phys. Rev. B* **93**, 140504 (2016).
- [11] He, Y. *et al.* Fermi Surface and Pseudogap Evolution in a Cuprate Superconductor. *Science* **344**, 612–616 (2014).
- [12] Hashimoto, M. *et al.* Direct spectroscopic evidence for phase competition between the pseudogap and superconductivity in $\text{Bi}_2\text{Sr}_2\text{CaCu}_2\text{O}_{8+\delta}$. *Nat. Phys.* **10**, 483–495 (2014).
- [13] Vishik, I. M. Photoemission perspective on pseudogap, superconducting fluctuations, and charge order in cuprates: a review of recent progress *Reports Prog. Phys.* **81**, 062501 (2018).
- [14] Fujita, M., Goka, H., Yamada, K., Tranquada, J. M. & Regnault, L. P. Stripe order, depinning, and fluctuations in $\text{La}_{1.875}\text{Ba}_{0.125}\text{CuO}_4$ and $\text{La}_{1.875}\text{Ba}_{0.075}\text{Sr}_{0.050}\text{CuO}_4$. *Phys. Rev. B* **70**, 104517 (2004).
- [15] Kohsaka, Y. *et al.* An intrinsic bond-centered electronic glass with unidirectional domains in underdoped cuprates. *Science* **315**, 1380–1385 (2007).
- [16] Lawler, M. J. *et al.* Intra-unit-cell electronic nematicity of the high-T_c copper-oxide pseudogap states. *Nature* **466**, 347–351 (2010).
- [17] Ghiringhelli, G. *et al.* Long-Range Incommensurate Charge Fluctuations in $(\text{Y,Nd})\text{Ba}_2\text{Cu}_3\text{O}_{6+x}$. *Science* **337**, 821–825 (2012).
- [18] Hamidian, M. H. *et al.* Detection of a Cooper-pair density wave in $\text{Bi}_2\text{Sr}_2\text{CaCu}_2\text{O}_{8+x}$. *Nature* **532**, 343–347 (2016).
- [19] Tranquada, J. M. Cuprate superconductors as viewed through a striped lens. *Adv. Phys.* **69**, 437–509 (2020).
- [20] Yang, H. B., Rameau, J. D., Johnson, P. D., Valla, T., Tselvik, A. & Gu, G. D. Emergence of preformed Cooper pairs from the doped Mott insulating state in $\text{Bi}_2\text{Sr}_2\text{CaCu}_2\text{O}_{8+\delta}$. *Nature* **456**, 77–80 (2008).
- [21] Li, L. *et al.* Diamagnetism and Cooper pairing above T_c in cuprates. *Phys. Rev. B* **81**, 054510 (2010).
- [22] Bilbro, L. S., Aguilar, R. V., Logvenov, G., Pelleg, O., Bozovic, I. & Armitage, N.

- P. Temporal correlations of superconductivity above the transition temperature in $\text{La}_{2-x}\text{Sr}_x\text{CuO}_4$ probed by terahertz spectroscopy. *Nat. Phys.* **7**, 298–302 (2011).
- [23] Zhou, P. *et al.* Electron pairing in the pseudogap state revealed by shot noise in copper oxide junctions. *Nature* **572**, 493–496 (2019).
- [24] Martin, S., Fiory, A. T., Fleming, R. M., Schneemeyer, L. F. & Waszczak, J. V. Normal-state transport properties of $\text{Bi}_{2+x}\text{Sr}_{2-y}\text{CuO}_{6+\delta}$ crystals. *Phys. Rev. B* **41**, 846 (1990).
- [25] Gurvitch, M. & Fiory, A. T. Resistivity of $\text{La}_{1.825}\text{Sr}_{0.175}\text{CuO}_4$ and $\text{YBa}_2\text{Cu}_3\text{O}_7$ to 1100K: Absence of Saturation and Its Implications. *Phys. Rev. Lett.* **59**, 1337 (1987).
- [26] Cooper, R. A. *et al.* Anomalous Criticality in the Electrical Resistivity of $\text{La}_{2-x}\text{Sr}_x\text{CuO}_4$. *Science* **323**, 603–607 (2009).
- [27] Ayres, J. *et al.* Incoherent transport across the strange-metal regime of overdoped cuprates. *Nature* **595**, 661–666 (2021).
- [28] Sachdev, S. & Keimer, B. Quantum criticality. *Phys. Today* **64**, 29 (2011).
- [29] Damascelli, A., Hussain, Z. & Shen, Z. X. Angle-resolved photoemission studies of the cuprate superconductors. *Rev. Mod. Phys.* **75**, 473–541 (2003).
- [30] Chen, S.-D. *et al.* Incoherent strange metal sharply bounded by a critical doping in Bi2212 . *Science* **366**, 1099–1102 (2019).
- [31] Maldacena, J. The Large N Limit of Superconformal field theories and supergravity. *Adv. Theor. Math. Phys.* **2**, 231–252 (1998).
- [32] Hartnoll, S. A. Lectures on holographic methods for condensed matter physics. *Class. Quantum Gravity* **26**, 224002 (2009).
- [33] Davison, R. A., Schalm, K. & Zaanen, J. Holographic duality and the resistivity of strange metals. *Phys. Rev. B* **89**, 245116 (2014).
- [34] Lucas, A. & Hartnoll, S. A. Resistivity bound for hydrodynamic bad metals. *Proc. Natl. Acad. Sci. U. S. A.* **114**, 11344–11348 (2017).
- [35] Zaanen, J. Planckian dissipation, minimal viscosity and the transport in cuprate strange metals. *SciPost Phys.* **6**, 061 (2019).
- [36] Fujita, K. *et al.* Simultaneous transitions in cuprate momentum-space topology and electronic symmetry breaking. *Science* **344**, 612–616 (2014).
- [37] Drozdov, I. K. *et al.* Phase diagram of $\text{Bi}_2\text{Sr}_2\text{CaCu}_2\text{O}_{8+\delta}$ revisited. *Nat. Commun.* **9**:5210 (2018).
- [38] Hussey, N. E., Abdel-Jawad, M., Carrington, A., Mackenzie, A. P. & Balicas, L. A coherent three-dimensional Fermi surface in a high-transition-temperature superconductor. *Nature* **425**, 814–817 (2003).
- [39] Vignolle, B. *et al.* Quantum oscillations in an overdoped high- T_c superconductor. *Nature* **455**, 952–955 (2008).
- [40] Uemura, Y. J. *et al.* Magnetic-field penetration depth in $\text{Ti}_2\text{Ba}_2\text{CuO}_{6+\delta}$ in the overdoped regime. *Nature* **364**, 605–607 (1993).

- [41] Lemberger, T. R., Hetel, I., Tsukada, A., Naito, M. & Randeria, M. Superconductor-to-metal quantum phase transition in overdoped $\text{La}_{2-x}\text{Sr}_x\text{CuO}_4$. *Phys. Rev. B* **83**, 140507 (2011).
- [42] Bozovic, I., He, X., Wu, J. & Bollinger, A. T. Dependence of the critical temperature in overdoped copper oxides on superfluid density. *Nature* **536**, 309–311 (2016).
- [43] Ohsugi, S., Kitaoka, Y. & Asayama, K. Temperature dependence of Spin Susceptibility of $\text{La}_{2-x}\text{Sr}_x\text{CuO}_4$. *Physica C* **282–287**, 1373–1374 (1993).
- [44] Wang, Y. *et al.* Weak-coupling d-wave BCS superconductivity and unpaired electrons in overdoped $\text{La}_{2-x}\text{Sr}_x\text{CuO}_4$ single crystals. *Phys. Rev. B* **76**, 064512 (2007).
- [45] Mahmood, F., He, X., Bozovic, I. & Armitage, N. P. Locating the Missing Superconducting Electrons in the Overdoped Cuprates $\text{La}_{2-x}\text{Sr}_x\text{CuO}_4$. *Phys. Rev. Lett.* **122**, 027003 (2019).
- [46] Kondo, T. *et al.* Disentangling Cooper-pair formation above the transition temperature from the pseudogap state in the cuprates. *Nat. Phys.* **7**, 21–25 (2011).
- [47] Kondo, T. *et al.* Point nodes persisting far beyond T_c in Bi2212 . *Nat. Commun.* **6**:7699 (2015).
- [48] He, Y. *et al.* Superconducting Fluctuations in Overdoped $\text{Bi}_2\text{Sr}_2\text{CaCu}_2\text{O}_{8+\delta}$. *Phys. Rev. X* **11**, 031068 (2021).
- [49] Rourke, P. M. C. *et al.* Phase-fluctuating superconductivity in overdoped $\text{La}_{2-x}\text{Sr}_x\text{CuO}_4$. *Nat. Phys.* **7**, 455–458 (2011).
- [50] Lee-Hone, N. R., Özdemir, H. U., Mishra, V., Broun, D. M. & Hirschfeld, P. J. Low energy phenomenology of the overdoped cuprates: Viability of the Landau-BCS paradigm. *Phys. Rev. Res.* **2**, 013228 (2020).
- [51] Maier, T. A., Karakuzu, S. & Scalapino, D. J. The overdoped end of the cuprate phase diagram. *Phys. Rev. Res.* **2**, 033132 (2020).
- [52] Spivak, B., Oreto, P. & Kivelson, S. A. d-Wave to s-wave to normal metal transitions in disordered superconductors. *Phys. B Condens. Matter* **404**, 462–465 (2009).
- [53] Li, Z. X., Kivelson, S. A., & Lee, D. H. Superconductor-to-metal transition in overdoped cuprates *npj Quantum Mater.* **6**:36 (2021).
- [54] Kopp, A., Ghosal, A. & Chakravarty, S. Competing ferromagnetism in high-temperature copper oxide superconductors. *Proc. Natl. Acad. Sci.* **104**, 6123–6127 (2007).
- [55] Sonier, J. E. *et al.* Direct search for a ferromagnetic phase in a heavily overdoped nonsuperconducting copper oxide. *Proc. Natl. Acad. Sci.* **107**, 17131–17134 (2010).
- [56] Li, X. *et al.* Quasiparticle interference and charge order in a heavily overdoped non-superconducting cuprate. *New J. Phys.* **20**, 063041 (2018).
- [57] Peng, Y. Y. *et al.* Re-entrant charge order in overdoped $(\text{Bi,Pb})_{2.12}\text{Sr}_{1.88}\text{CuO}_{6+\delta}$ outside the pseudogap regime. *Nat. Mater.* **17**, 697–702 (2018).

- [58] Li, X. *et al.* Evolution of Charge and Pair Density Modulations in Overdoped $\text{Bi}_2\text{Sr}_2\text{CuO}_{6+\delta}$. *Phys. Rev. X* **11**, 011007 (2021).
- [59] Fischer, Ø., Kugler, M., Maggio-Aprile, I., Berthod, C. & Renner, C. Scanning tunneling spectroscopy of high-temperature superconductors *Rev. Mod. Phys.* **79**, 353–419 (2007).
- [60] Hoffman, J. E. Spectroscopic scanning tunneling microscopy insights into Fe-based superconductors. *Reports Prog. Phys.* **74**, 124513 (2011).
- [61] Yazdani, A., Da Silva Neto, E. H. & Aynajian, P. Spectroscopic Imaging of Strongly Correlated Electronic States. *Annu. Rev. Condens. Matter Phys.* **7**, 11–33 (2016).
- [62] Binnig, G. & Rohrer, H. Scanning Tunneling Microscopy—from Birth to Adolescence (Nobel Lecture). *Rev. Mod. Phys.* **59**, 615 (1987).
- [63] Chen, C. J. *Introduction to Scanning Tunneling Microscopy*. (Oxford University Press, 2000).
- [64] Battisti, I., Verdoes, G., Van Oosten, K., Bastiaans, K. M. & Allan, M. P. Definition of design guidelines, construction, and performance of an ultra-stable scanning tunneling microscope for spectroscopic imaging. *Rev. Sci. Instrum.* **89**, 123705 (2018).
- [65] Crommie, M., Lutz, C. & Eigler, D. Imaging standing waves in a 2D electron gas *Nature* **363**, 524–527 (1993).
- [66] Petersen, L. *et al.* Direct imaging of the two-dimensional Fermi contour: Fourier-transform STM *Phys. Rev. B* **57**, R6858 (1998).
- [67] Wang, Z. *et al.* Quasiparticle interference and strong electron-mode coupling in the quasi-one-dimensional bands of Sr_2RuO_4 . *Nat. Phys.* **13**, 799–805 (2017).
- [68] Li, H. *et al.* Rotation symmetry breaking in the normal state of a kagome superconductor KV_3Sb_5 *Nat. Phys.* **18**, 265–270 (2022).
- [69] Hoffman, J. E. *et al.* Imaging Quasiparticle Interference in $\text{Bi}_2\text{Sr}_2\text{CaCu}_8$ *Science* **297**, 1148–1151 (2002).
- [70] Allan, M. P. *et al.* Anisotropic Energy Gaps of Iron-Based Superconductivity from Intraband Quasiparticle Interference in LiFeAs . *Science* **336**, 563–567 (2012).
- [71] Coleman, P. *Introduction to Many-body Physics*. (Cambridge University Press, 2015).
- [72] Hufner, S. *Photoelectron Spectroscopy*. (Springer-Verlag, 2003).
- [73] Sulangi, M. A. & Zaanen, J. Self-energies and quasiparticle scattering interference. *Phys. Rev. B* **98**, 094518 (2018).
- [74] Feenstra, R. M., Stroscio, J. A. & Fein, A. P. Tunneling spectroscopy of the $\text{Si}(111)2\times 1$ surface. *Surf. Sci.* **181**, 295–306 (1987).
- [75] Macdonald, A. J. *et al.* Dispersing artifacts in FT-STs: A comparison of set point effects across acquisition modes. *Nanotechnology* **27**, 414004 (2016).

2 Direct Comparison of ARPES, STM, and Quantum Oscillation Data for Band Structure Determination in Sr_2RhO_4

This chapter has been published as
Battisti et. al. *npj Quant. Mat.* **5**: 91 (2020)

Discrepancies in the low-energy quasiparticle dispersion extracted from angle resolved photoemission, scanning tunneling spectroscopy and quantum oscillation data are common and have long haunted the field of quantum matter physics. Here, we directly test the consistency of results from these three techniques by comparing data from the correlated metal Sr_2RhO_4 . Using established schemes for the interpretation of the experimental data, we find good agreement for the Fermi surface topography and carrier effective masses. Hence, the apparent absence of such an agreement in other quantum materials, including the cuprates, suggests that the electronic states in these materials are of different, non-Fermi liquid like nature. Finally, we discuss the potential and challenges in extracting carrier lifetimes from photoemission and quasiparticle interference data.

2.1 Introduction

2

Strongly correlated electrons are at the root of some of the most mysterious quantum materials, including unconventional superconductors, strange metals, and heavy fermion materials¹⁻⁵. Most of the exotic phases of electronic matter in these systems emerge from collective behavior of the electrons. A universally accepted understanding of these systems is still lacking, and requires close cooperation between scientists using different theoretical and experimental methods. From the experimental side, many insights to date have come from spectroscopic techniques that probe the band structure and many-body renormalizations of electrons close to the Fermi level, including angle-resolved photoemission (ARPES), scanning tunneling microscopy (STM), and quantum oscillations (QO), which are the focus of this article.

In the most widely used interpretations, spectroscopic-imaging STM (SI-STM) and ARPES probe the spectral function in real and reciprocal space⁶⁻¹⁰. Quantum oscillations probe the Fermi surface area and the k -averaged cyclotron mass which can in turn be related to the pole of the spectral function at energies close to the Fermi level¹¹. There should thus be well-defined relations between the quantities measured by these three techniques¹².

Surprisingly though, several apparent contradictions between results based on these techniques can be found in the literature. Such contradictions can involve very fundamental properties of the electronic structure: for example, quantum oscillation studies on underdoped cuprate high-temperature superconductors claim the existence of Fermi surface pockets while STM and ARPES reported disconnected Fermi arcs^{13,14}. Similarly, the strength of gap inhomogeneities seen by STM in several unconventional superconductors appears to be inconsistent with gap broadening in ARPES spectra that average over large areas. These and other discrepancies between results of different techniques have previously been discussed in cuprate superconductors¹⁵⁻¹⁸, heavy fermion systems¹⁹ and topological insulators²⁰. However, it often remains unknown if these apparent differences are a consequence of some inherent limitations of the techniques or if they are due to challenges of data interpretation, also connected to the exotic non-Fermi-liquid nature of some of these systems. Given this lack of understanding, discrepancies are frequently attributed to the use of samples grown in different research laboratories or are ignored because of a lack of trust in one of the techniques.

With this article, we aim to test the consistency of data from ARPES, STM and QO experiments by making an unbiased comparison on the same correlated electron material. The ideal candidate for such a comparison should be a quasi-two-dimensional (2D) metal in which electron correlations still play an important role, but without the mysteries associated with materials like unconventional superconductors. Ideally it should further be structurally similar to the cuprates, ruthenates and iridates. Such a material could then act as a representative for the wider class of transition metal oxides, but -in contrast to cuprates, ruthenates and iridates- is well understood and simple enough that it can clearly be described within Fermi liquid theory. With this in mind, we chose Sr_2RhO_4 , a layered perovskite that fulfills the conditions above.

2.2 Results & discussions

2.2.1 ARPES and QPI Fermi Surface

In **Figs. 2.1 and 2.2**, we compare Fermi surface data from the three techniques. Consistent with previous reports^{11,21,22}, the ARPES k -space map (**Fig. 2.1a**) shows two nearly circular contours that are backfolded to form 3 pockets; a hole-like α pocket centered at Γ , a lens-shaped electron pocket at M (β_M) and a square-shaped hole pocket at X (β_X). The backfolding is of structural origin and arises from a staggered rotation of the RhO_6 octahedra around the c -axis, which doubles the in-plane unit cell. Hybridization with e_g states pushes the xy band of Sr_2RhO_4 below the chemical potential, leaving a Fermi surface with out-of-plane xz/yz character, containing 3 electrons per Rh site^{11,22,23}. Despite the quasi-1D hopping associated with the out-of-plane orbitals, the Fermi surface is nearly isotropic. This change arises from a strong level repulsion of states that would be degenerate in the absence of spin-orbit coupling^{24,25}. The marked anticrossing can be attributed to an enhancement of spin-orbit splittings in the presence of electronic correlations²⁵⁻²⁷.

Figs. 2.1b,c show an STM topography and a constant energy conductance layer, where spatial modulations attributed to quasiparticle interference are neatly resolved. The few atomic defects in the field of view clearly act as scattering centers for quasiparticles, creating the interfering standing wave patterns. The Fourier-transform of the normalized conductance layer at the Fermi level $E=0$ meV is shown in **Fig. 2.1d**. To mitigate the set-up effect, we

take the Fourier transform not of the conductance layers $dI/dV(\mathbf{r}, eV)$, but of the normalized conductance data, $dI/dV(\mathbf{r}, eV)/(I(\mathbf{r}, eV)/V)$, where $I(\mathbf{r}, eV)$ is the tunnelling current and V is the bias voltage (see discussion in the methods and **Fig 2A.1**)^{28–32}. For the β band, we directly observe the STM ‘Fermi surface’ with wave-vector $\mathbf{q}=2\mathbf{k}_F$. More generally, we expect to observe features corresponding to scattering vectors \mathbf{q} that connect points of high spectral weight in momentum space. For the present case, we can readily connect these \mathbf{q} vectors with the Fermi surface measurement from ARPES. Interestingly, different scattering processes have different strength. While some scattering processes are very clear, others are less visible or completely absent. Varying intensities or absences of scattering processes have been observed in other materials^{33–35} and can stem from the differences in the scattering process. For example, different QPI scattering intensities are expected from magnetic versus potential scattering or from broad coulombic potentials versus localized impurity potentials^{36–40}. In principle, theoretical tools exist to predict QPI intensities based on both the electronic structure of the material, and the nature of the scattering potential^{36–40}. A comparison with such QPI simulations could allow us to learn more about the defect states in Sr₂RhO₄.

In **Fig. 2.1e**, we use the Fourier transform of the SI-STM data discussed above to reconstruct the entire FS of Sr₂RhO₄ from the QPI pattern. To this end, we first extract peaks in the data by fitting the intensity profiles in radial cuts (see **Fig 2A.2**). We then obtain the fundamental β band in k -space by rescaling the \mathbf{q} -vectors by a factor of two. The backfolded β bands are obtained by translating the fundamental band by reciprocal lattice vectors determined from the STM topography. The α band is reconstructed by subtracting the interband vector $\mathbf{q}_{\alpha-\beta}$ from the intraband scattering $\mathbf{q}_{\beta-\beta}$. In **Fig. 2.1e**, we display in blue the data points derived in this way, and in grey the direct interband scattering vectors $\mathbf{q}_{\alpha-\beta}$ that we used for the derivation. The identification of the grey scattering vectors as $\mathbf{q}_{\alpha-\beta}$ is corroborated by the Fermi velocity we obtain for this vector (see below). The direct comparison of these contours with the ARPES Fermi surface shows good agreement for all Fermi surface pockets, as further illustrated in **Fig. 2A.3**.

2.2.2 Shubnikov de Haas Oscillations

Next, we use QO to find the Fermi surface areas and quasiparticle masses. The inset of **Fig. 2.2a** shows a trace of quantum oscillations in the magnetoresistance at 0.1 K (Shubnikov de Haas (SdH) oscillations). To extract

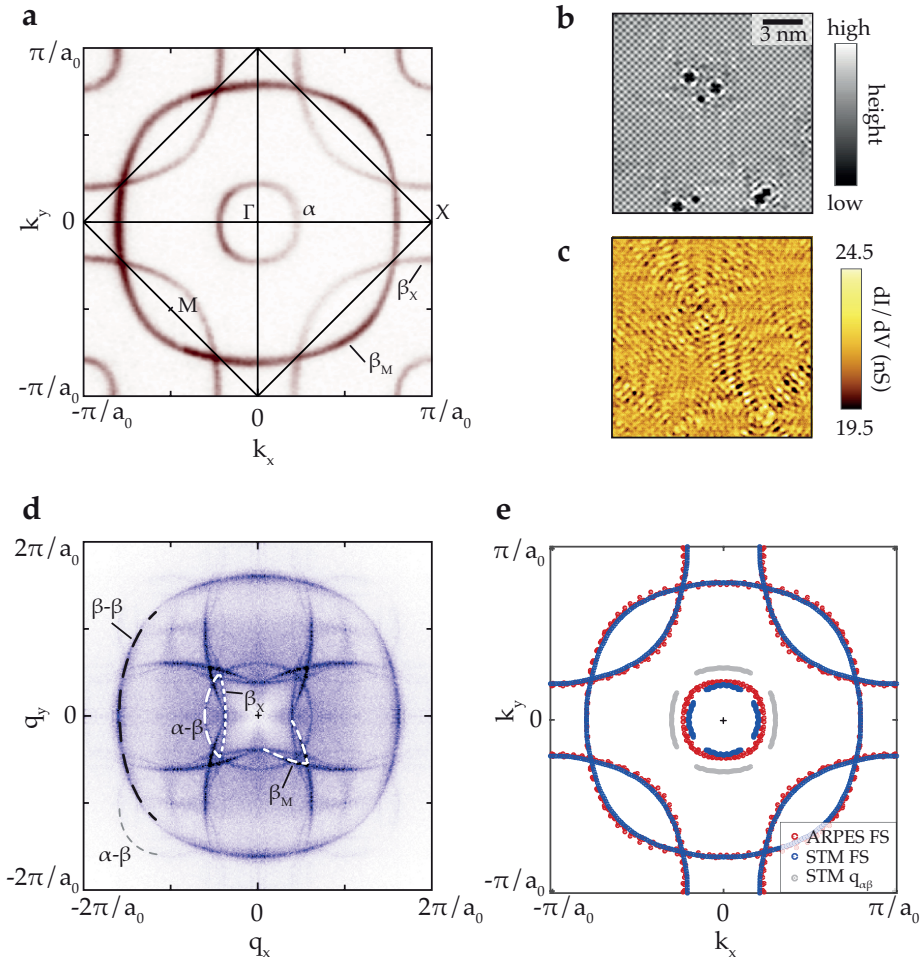


Figure 2.1 Sr_2RhO_4 Fermi surfaces.

a) ARPES Fermi surface. **b)** STM topograph with atomic resolution showing presence of impurities. **c)** STM conductance layer $dI/dV(r, eV)$ at energy $eV = -20 \text{ meV}$, acquired simultaneously to the topograph in panel b, showing interference between quasiparticles standing waves patterns. **d)** STM 'Fermi surface', obtained by a two-dimensional Fourier transform of the conductance layer corresponding to the Fermi level of a spectroscopic map measured over a field of view of $70 \times 70 \text{ nm}^2$. Here and for all QPI data, we show the normalized data, i.e. the Fourier transform of $dI/dV(r, eV)/(I(r)/eV)$, to mitigate the set-up effect (see Methods). The data is additionally symmetrized and the low- q components are suppressed with a 2D gaussian: raw data is shown in Supplementary Figure 1. **e)** Comparison between extracted Fermi surfaces of ARPES and STM. For completeness, we also show the QPI signal of $q_{\alpha\beta}$ which was used in the derivation (see text and Figs. 2A.2 and 2A.3).

Fermi surface information from the quantum oscillations measurement, we analyse the frequency components plotted in **Fig. 2.2a**. Seven closely spaced peaks are resolved, corresponding to seven frequencies between 0.9 kT and 1.3 kT. This might be surprising at first, as from our previous analysis we expect only three distinct Fermi surface pockets. We attribute the higher number of QO frequencies to two effects. Firstly, the finite interlayer hopping implies that the Fermi surface of Sr₂RhO₄ is quasi-cylindrical, and thus has multiple extremal orbits per sheet. The characteristic signature of such a remnant 3D Fermi surface warping is an overall $1/\cos(\theta)$ field angle dependence of the frequencies (consistent with quasi-2D electronic structure) with small splittings that disappear for certain angles, as observed in **Fig. 2.2b**. The quasi-2D nature of the quasiparticle band structure is confirmed directly by photon energy dependent ARPES measurements (**Fig. 2.2c**) probing the Fermi surface along k_z . Secondly, the ARPES measurements resolve a small splitting in the β -band along ΓM . This small degeneracy lifting can be attributed to the doubling of the unit cell along the c -axis and is reproduced by LDA+U+SO band structure calculations²⁵. Hence, there are four primary frequencies up to the measured out-of-plane angle of 40°. We can then use multiple facts to constrain the band assignments: (i), Following ARPES and STM data, the extremal orbit areas increase in size from the α (hole), β_M (electron) and β_X (hole). (ii), The total electron count should be 3 electrons per Rh atom. (iii), The experimental specific heat γ can be calculated in the 2D approximation from:

$$\gamma = (\pi N_A k_B^2 a^2) (3\hbar^2)^{-1} (m_\alpha + 2m_{\beta M} + m_{\beta X}) \quad (2.1)$$

where N_A is Avogadro's number, k_B is Boltzmann's constant, a is the tetragonal lattice parameter (3.857 Å) and \hbar is Planck's constant. (iv), Following the ARPES data, the β_M band should be split leading to two frequencies.

Combining these conditions, we draw the conclusion that α corresponds to the lowest frequency (0.93 kT, corresponding to 1.934 electron/Rh, see methods), β_M to the two middle frequencies (average 1.068 kT, 0.152 electrons/Rh) and β_X to the highest frequency (1.288 kT, 0.908 electrons/Rh). The calculated $\gamma = 17.4 \pm 0.8$ mJ/Rh mol K² then agrees with the directly observed value of 17.7 ± 0.7 mJ per Rh mol K², and the total electron count is 2.994 electrons per Rh. A quantitative comparison of the Fermi surface volumes extracted from ARPES, QO and STM based on this assignment can be found in **Table 2.1**. QO amplitudes also yield the Dingle temperatures (1.5K for the α pocket, 1.5K for

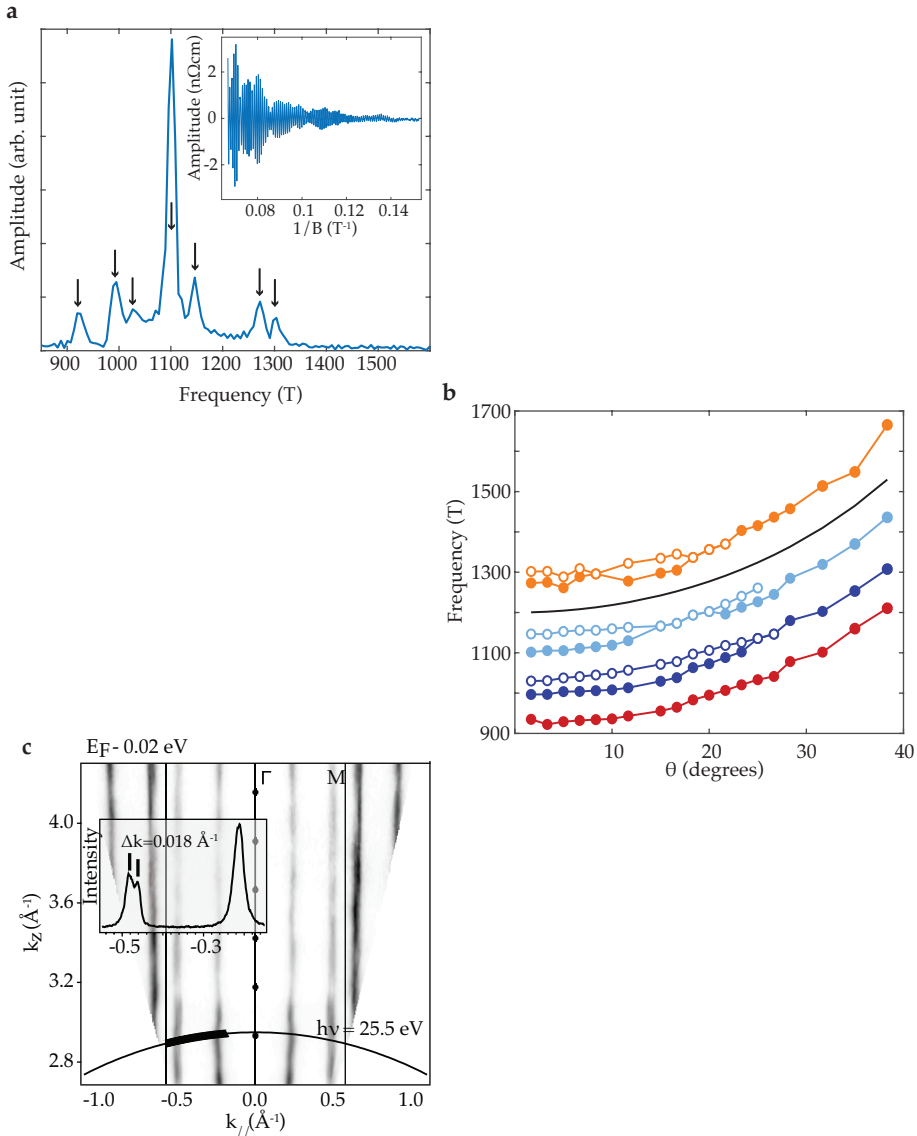


Figure 2.2 Quantum oscillations and k_z dispersion.

a) Shubnikov-de Haas oscillations at 0.1 K for a magnetic field parallel to the c -axis. The main panel shows the frequency components obtained by Fourier transform of the quantum oscillation trace shown in the inset. The peaks correspond to Fermi surface pockets. The background subtraction used was a third order polynomial and the field sweep rate was 0.05 T/min. The noise level is 50 pVHz^{-1/2}. **b)** Angle dependence of the QO frequencies for angle θ from the c -axis. The solid black line is a $1/\cos\theta$ dependence expected for a quasi-two-dimensional Fermi surface. **c)** ARPES k_z dependence in the $M\Gamma$ high symmetry direction at $E = -20$ meV, showing only slight modulations of the band along the c -axis.

the β_M pocket, and 1.9K for the β_X pocket), which can be related to the mean free path of the electrons. We refer to the literature for a detailed discussion on the challenges of such an interpretation⁴¹.

2.2.3. Quasi-particle Dispersion

We now turn our attention to the low-energy dispersion. In **Fig. 2.3**, we show constant energy layers for selected energy levels and the energy-momentum dispersion along the two high symmetry directions for both ARPES and SI-STM. These data confirm that β_M is an electron pocket while α and β_X are

		α	β_M	β_X	
v_F (eV Å)	QO	0.41*	0.47*	0.49*	
	ARPES	0.41	0.57/0.77	0.55	
	STM	0.41*	0.70	0.55	
$\langle A \rangle$ (%)	ARPES	7.7%	7.9%	9.1%	
	STM	6.8%	7.1%	7.9%	
	QO <peaks>	6.6%	7.6%	9.2%	
	QO single peak		6.6%	7.1%	9.1%
				7.3%	9.3%
				7.9%	
			8.2%		
$\langle m \rangle$ (m_e)	QO	3.1	2.9	3.1	
	ARPES	3.3	2.2	3.3	
	STM	-	2.4	2.9	

Table 2.1 Summary of band structure parameters from different techniques.

Comparison between values obtained from the three techniques. v_F is the Fermi velocity, A (in % of the reduced tetragonal Brillouin zone) and $\langle m \rangle$ (in units of m_e) are the Brillouin zone filling and average mass for each of the three sheets, respectively. The pocket-averaged Fermi velocities from QO (marked with *) are extracted using $\hbar k_F = m v_F$ using the pocket-averaged Fermi wave vector. The Fermi velocity for the α band from STM (also marked with *) was extracted from the slope of the $q_{\alpha\beta}$ and $q_{\beta\beta}$ signals. The QO values for A are given both as average over the multiple peaks for each pocket, and for every peak.

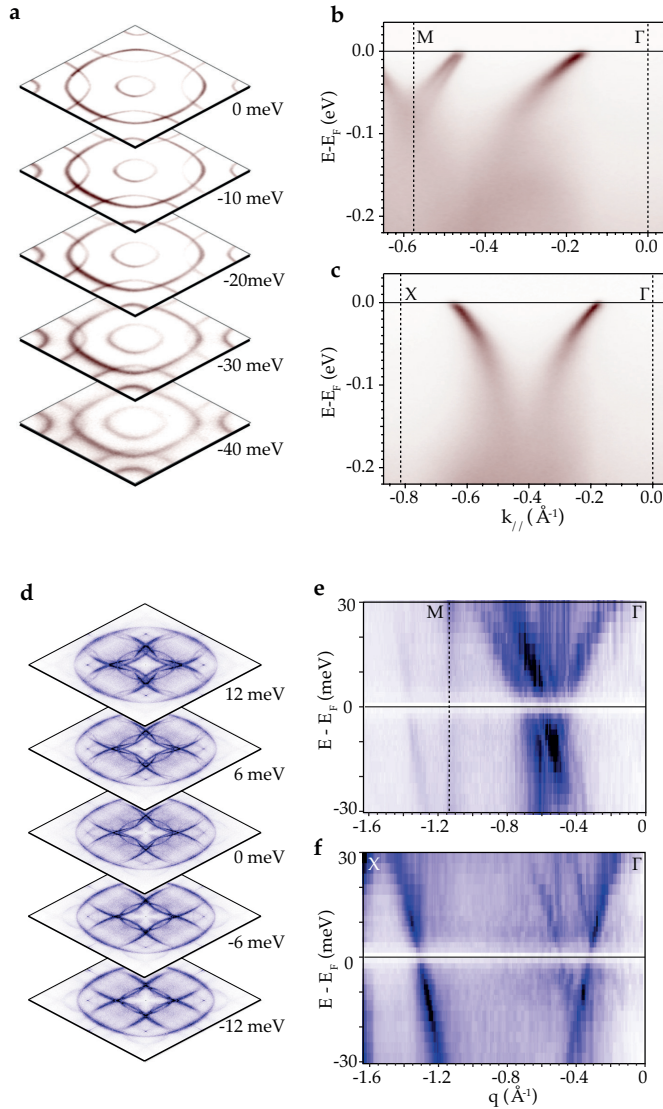


Figure 2.3 ARPES and QPI dispersions along high symmetry directions.

a) ARPES constant energy layers at selected energies at and below the Fermi level. **b-c)** ARPES dispersions along the high symmetry directions M Γ and X Γ . **d)** Fourier transform of normalized STM conductance layers $dI/dV(\mathbf{r}, eV)/(I(\mathbf{r})/V)$ at selected energies around the Fermi level. **e-f)** Dispersions of the scattering vectors \mathbf{q} obtained from STM QPI for the two high symmetry directions M Γ and X Γ , where X and M are defined as for ARPES but at double the reciprocal vectors. To improve signal-to-noise, the dispersions are obtained by averaging 10 cuts in a radial span of $\pm 5^\circ$ from the high symmetry direction. The intensity around the Fermi level is suppressed due to the normalization with the total conductance $(dI/dV)/(I/V)$, as explained in the Methods.

hole-like. The ARPES data also reproduce the splitting of the β band along ΓM observed in **Fig. 2.2**. The STM dispersions plots show several features that are not observed by ARPES. These can all be assigned to different β - β intraband and α - β interband scattering vectors translated by reciprocal lattice vectors. The q vector which is most clearly resolved by STM along both high-symmetry directions arises from β - β intraband scattering. Comparing its dispersion with the β -band measured by ARPES, we find quantitative agreement along ΓX , where both techniques lead to measured Fermi velocities $v_F = 0.55\text{eV}\text{\AA}$. Along ΓM , where band structure calculations find a small splitting in the Fermi surface, our ARPES data resolves both bands and shows that they have slightly different dispersion with Fermi velocities of $0.57\text{eV}\text{\AA}$ and $0.77\text{eV}\text{\AA}$, respectively, compared to $v_F = 0.70\text{eV}\text{\AA}$ extracted from the STM dispersion. The lack of a noticeable splitting in the STM dispersion cannot be explained by insufficient momentum resolution, suggesting that it is due to a vanishing STM matrix element for one of the bands.

In order to extend this comparison to QO, we look at the quasiparticle cyclotron masses m^* . These masses can be deduced for individual Fermi surface pockets from the temperature dependence of the quantum oscillation amplitudes using the Lifshitz-Kosevich formula (**Fig. 2A.4**). For a 2D Fermi surface, they can also be calculated without any approximations from the full mapping of the low-energy quasiparticle band structure obtained by STM and ARPES, using

$$m^* = \frac{\hbar^2}{2\pi} \frac{dA_{FS}}{dE} \quad (2.2)$$

where A_{FS} is the Fermi surface volume. To this end, we extract the areas of the pockets not only at the Fermi energy, but at a few constant energy layers within a small window. The linear fits of these areas shown in **Fig. 2.4** yield the effective masses of the different pockets. We note that the slope dA_{FS}/dE decreases strongly near the chemical potential in the ARPES data while no such effect is observed in STM. This change of slope is a known artifact arising from the combination of a Fermi cutoff and finite energy resolution. For the quantification of m^* , we thus exclude a narrow energy range around E_F from the ARPES data. **Table 2.1** shows the values of the effective masses obtained by STM, ARPES, and QO measurements. Knowledge of m^* and the Fermi surface area also allows a sheet-averaged Fermi velocity to be calculated from QO data as

$$v_F = \hbar(A/\pi)^{1/2}/m^* \quad (2.3)$$

These values are also shown in **Table 2.1** for comparison with STM and ARPES.

2.2.4. Lifetime Analysis

Finally, we discuss the extraction of peak widths in the ARPES and STM data, which can in principle be related to quasiparticle lifetimes. Here, the two techniques face rather different challenges. In simple systems, like Sr_2RhO_4 studied here, the measured photoemission intensity appears to represent the spectral function. For a sufficiently linear band, the imaginary part of the self-

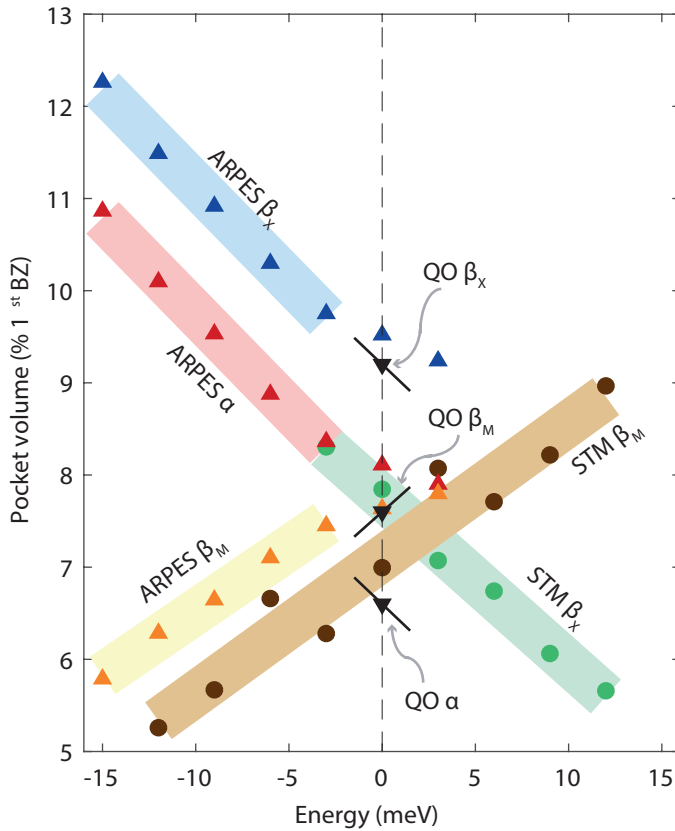


Figure 2.4 Fermi surface pockets and effective masses.

Extraction of effective masses from ARPES, STM, and QO. The data points show the volume $dA_{\text{FS}}(\omega)$ of the different pockets as a function of energy (see also Fig 2A.5). The effective masses are proportional to the slope of $dA_{\text{FS}}(\omega)$. For the fits of the ARPES data, we excluded datapoints that are closer to the Fermi level than the energy resolution of the detector. The black lines and marks around the Fermi level indicate the masses and volumes extracted from QO.

energy (which is equal to half the inverse lifetime in a Fermi liquid) can thus be obtained from the width W_k of the momentum distribution curves (MDC) as

$$\Sigma''(k, \omega) = W_k(\omega)v(\omega)/2 \quad (2.4)$$

where $v(\omega)$ is the slope of the dispersion at the same energy. In practice, the main difficulty is the treatment of the effective resolution of ARPES measurement. ARPES peak widths measured at state-of-the-art instruments are rarely limited by the instrumental energy and momentum resolution but contain a variety of other contributions that are notoriously hard to quantify. These include in particular broadening from the finite integration over perpendicular momenta, structural mosaicity in the probed area and the often-unknown quality of the surface. Additional broadening can occur from work function inhomogeneities of and around the sample which cause uncontrolled electric fields that degrade the resolution of the electron optics. Finally, in an energy range of $\sim dE/2$, where dE is the effective energy resolution, the MDC peak position starts to deviate noticeably from the intrinsic quasiparticle pole, which prohibits a model-free analysis of very low energy dispersions and self-energies. STM does not suffer from these experimental difficulties. However, it is not always clear to what extent the tunneling spectra reflect $A(\mathbf{r}, \omega)$. In particular the so-called setup effect, the dependence of the tunneling spectra on the lateral variation of the tip-sample distance, which itself is defined by the setup current and voltage, can cause complications. In many cases, the set-up effect can be mitigated by taking ratios between different quantities as we do here, but then the interpretation of the resulting data is less straight forward. In addition, analyzing self-energies from STM data can be complicated when different \mathbf{q} vectors overlap, especially for complex Fermi surfaces. We also note that a unique reconstruction of the spectral function from STM data is not always possible. Perhaps most importantly, one has to consider the scattering mechanism, which can strongly influence line-shapes and line-widths³⁶⁻⁴⁰. For this reason, only few attempts have been made to extract lifetimes from STM data⁴²⁻⁴⁵.

Despite these difficulties, an analysis of the MDC's along the ΓX direction shown in **Figs. 2.5a-c** clearly show an energy dependence of the quasiparticle lifetime in fair agreement with the expectations for a Fermi liquid-like metal. In a Fermi liquid, we expect the imaginary part of the self-energy to be a quadratic function at low energy,

$$\Sigma''(\omega) = A\omega^2 \quad (2.5)$$

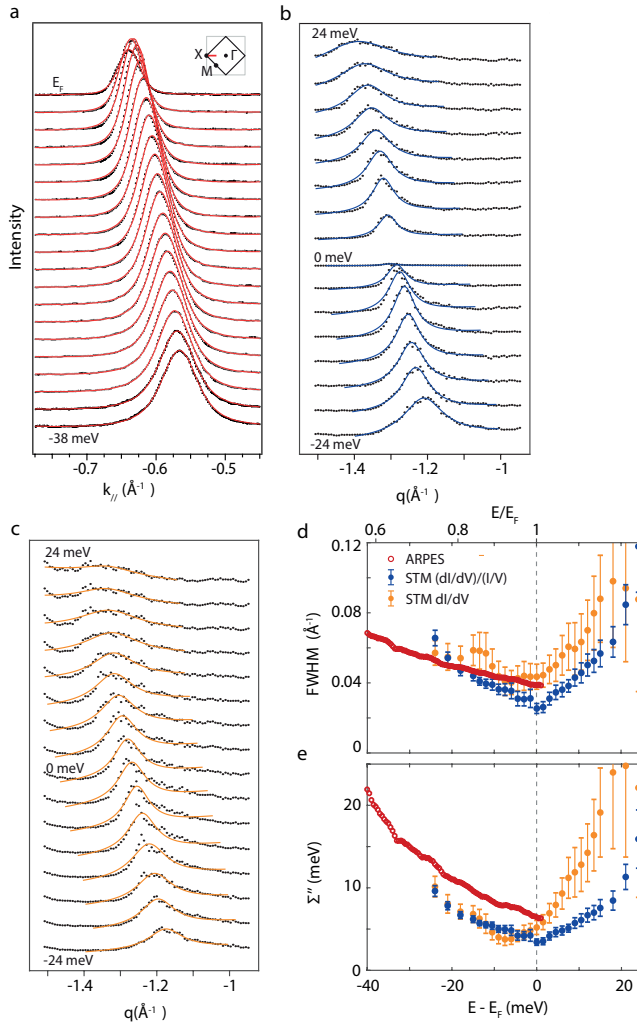


Figure 2.5 ARPES and QPI linewidths and self-energies.

Linewidth analysis for the β_x band. **a)** ARPES MDCs and Lorentzian fits (red). The inset shows the position of the cut as red line in the reduced Brillouin zone (black square). **b, c)** STM MDCs from normalized conductance $(dI/dV)/(I/V)$ (b) and conductance dI/dV (c) including Lorentzian fits (blue and orange, respectively) with a linear background. The cuts are equivalent to the one used in panel (a) at double the reciprocal lattice vectors. **d)** Comparison of the MDC widths $W_k(\omega)$ from STM and ARPES data. STM widths are phenomenological full-width-half-maximum extracted by Lorentzian fits, ARPES widths are extracted by fitting a Lorentzian convoluted with a Gaussian broadening that stems from the finite resolution. **e)** Comparison of the widths multiplied by the slope of the dispersion, which, in a simplified picture, equals to the imaginary part of the self-energy. Note that the scale of the energy axis spans a significant fraction of the Fermi energy, which is roughly 400meV for the β band (in the parabolic band approximation and before hybridization, as we assume that scattering processes that are relevant for the lifetimes do not discriminate between the β_x and β_M bands).

where A is a material specific prefactor. To compare our results with the expectation, we plot the linewidths and self-energies extracted from ARPES and STM data as a function of energy in **Figs. 2.5d,e** (for a comparison of the individual ARPES and STM spectral lines, see **Fig. 2A.6**). Indeed, our results are consistent with a quadratic dependence on energy. Further, the absolute scale of the measured self-energy is of the same order than what is obtained for Sr₂RhO₄ with dynamical mean field theory (DMFT)^{50,51} calculated for a generic two-dimensional Fermi liquid using the random phase approximation⁴⁶⁻⁴⁹. We note that the agreement holds for an energy range of that is a significant fraction of the Fermi energy, which is roughly 400meV for the β band when defined in the parabolic band approximation as

$$E_F = \hbar^2 A_{FS} / 2\pi m \quad (2.6)$$

This is encouraging for further lifetime investigations: given a good understanding of both the resolution for ARPES and the scattering process for STM, both techniques have the potential to bring insight into energy and momentum dependent correlation effects in electronic matter of quantum materials.

We show SI-STM results of Sr₂RhO₄ and extract its Fermi surface and low-energy dispersion, and present a quantitative comparison of the STM quasiparticle interference data with ARPES and QOs. Our data here reveals the previously unknown band structure above the Fermi level, and quasiparticle lifetimes for Sr₂RhO₄. We show that Fermi surface volumes agree among the three techniques within $\sim 1\%$ of an electron for all pockets, while quasiparticle masses exhibit a relative variation of $\sim 30\%$. We consider these values to be characteristic for the precision that can realistically be obtained in favorable cases with these three techniques, and therefore conclude that for the oxide Sr₂RhO₄, STM, ARPES, and QO can extract the same information regarding Fermi surface and low energy dispersion. The relevance of our study goes beyond Sr₂RhO₄: Our data suggest that apparent disagreements in the literature on cuprates do not arise from the intrinsic structural complexity of oxides but are likely a consequence of our limited understanding of materials with non-Fermi liquid electronic states and the applications of the techniques to such samples, especially ones with significant spatial inhomogeneity.

2A Appendix

2A.1 Methods

2A.1.1 Sample Preparation

Our single crystals samples were grown in a *Crystal Systems* four mirror image furnace using a flux feeding floating zone method. Dried SrCO_3 and Rh_2O_3 (3N) were ground together in a 1:0.575 ratio, pelletised and calcined at 1000°C in flowing O_2 atmosphere for 24 hours. Rods were hydrostatically pressed using the usual methods and sintered at 1100°C for 2 hours in flowing O_2 . The growth conditions in the image furnace were 100% O_2 gas at 10 bar pressure, growth speed of 10 mmhr^{-1} and a counter rotation of 30 rpm. Subsequently, the crystals were annealed 1150°C under flowing oxygen for 2 weeks, as described elsewhere.²²

The surfaces studied by STM and ARPES have been obtained by cleavage in ultrahigh vacuum.

2A.1.2 Quantum Oscillations:

Quantum oscillations measure low energy characteristics of the electron fluid in an applied magnetic field. The oscillations, caused by the Landau quantization from the magnetic field, give precise information on the size of the Fermi pockets and the effective masses of the electrons. Quantum oscillations are a true bulk probe that is generally not influenced by surface effects but they are very sensitive to disorder in the crystals and require high quality samples to be observed. Furthermore, they also require high magnetic field and low temperatures to suppress the quasiparticle-quasiparticle scattering and the interpretation is not always simple as little information is given about the loci, shape and type (electron or hole) of the Fermi pockets. When a strong magnetic field \mathbf{B} is applied to the sample, the Landau quantization of quasiparticle orbits leads to an oscillation of the density of states at the Fermi level, periodic in reciprocal field. These oscillations are reflected in most of the physical properties; in the case of magnetoresistance they are called Shubnikov–de Haas (SdH) oscillations^{41,52}. By analyzing the frequency f (in Tesla) of the oscillations across an inverse field range, the number and sizes of the Fermi surface pockets can be obtained. Moreover, the effective masses for the various pockets can be deduced from the temperature dependence of the

oscillation amplitude (**Fig. 2A.4**) via the Lifshitz-Kosevich formula, although, we note that the data analysis can be non-standard when measuring across a broad magnetic field range (for a comprehensive discussion see Ref. 22). The QO amplitudes also contain the Dingle temperature. These can be used to find mean free paths of 500 Å for the α pocket, 714 Å for the β_M pocket, and 481 Å for the β_X pocket.

2

Quantum oscillation data was acquired using a standard four probe technique in a dilution refrigerator (current $I = 300 \mu\text{A}$) for temperatures between 0.1 K and 1.0 K and magnetic fields between 7 T and 15 T. Low contact-resistance electrical connections were made to the crystals using gold wire (25 micron) and *Dupont 6838* high temperature curing paint (annealed at 470°C under O₂). The current was applied in the ab plane (the two-dimensional morphology of the crystals allowed for easy identification of the crystallographic ab plane and c axis). In the dilution refrigerator the samples were mounted on an in-situ single axis rotator for the angular quantum oscillation study. Three crystals were measured from the same batch, with consistent results.

2A.1.3 ARPES:

ARPES measures single particle excitations directly in momentum space. The most commonly used expression for the photocurrent $I(\mathbf{k}, \omega)$ is:

$$I_{ARPES} = I_0 |M_{f,i}|^2 f(\omega) A(\mathbf{k}, \omega) * R(\delta\mathbf{k}, \delta\omega) \quad (2.A1)$$

where M_{fi} represents the photoemission matrix elements, $A(\mathbf{k}, \omega)$ is the spectral function and $f(\omega)$ the Fermi function¹⁰. The expression for the intrinsic photocurrent is then convolved with the experimental momentum and energy resolution $R(\delta\mathbf{k}, \delta\omega)$. Besides experimental difficulties, complications can arise from the interference of photocurrents from different emission sites and/or from different terms in the light-matter interaction Hamiltonian. Expressing the photocurrent in terms of the spectral function further relies on the sudden approximation, i.e. the assumption that the photoexcitation is instantaneous and that there is no interaction between photoelectron and the sample during the photoemission process¹⁰. This approximation is well tested down to much lower photon energies than used in the present work.

The ARPES experiments reported in this paper have been performed at beamline I05 of Diamond Light source using photon energies in the range of 20 – 80 eV⁵³. Energy and momentum resolutions were set to $\sim 5 \text{ meV} / 0.008$

\AA^{-1} , except for the data shown in **Fig. 2.2c** where the resolution varied with photon energy and thus with k_z . All data were acquired at $T \sim 8\text{K}$.

2A.1.4 STM:

STM measures the tunneling current generated between an atomically sharp tip and a conducting sample when a voltage V is applied between the two. By scanning the tip over the sample surface, STM directly delivers real-space information with atomic resolution⁵³. The tunneling current I is directly proportional to the *integrated local* density of states (LDOS) of quasiparticles, which in the formalism of many-body physics can be defined via the *local* spectral function

$$A(\omega, \mathbf{r}) = \sum_{\mathbf{k}} A(\mathbf{k}, \omega; \mathbf{r}) \quad (2A.2)$$

The local spectral function of the sample can be accessed for both occupied and unoccupied states by measuring the local differential conductance⁵²:

$$\frac{dI}{dV}(eV, \mathbf{r}) = \frac{4\pi e^2}{\hbar} |t(\mathbf{r})|^2 A_T A_S(\omega = eV, \mathbf{r}) \quad (2A.3)$$

where $A_{s,t}$ are the spectral functions of sample and tip, respectively, and where we approximated the Fermi-Dirac distribution as a step function. $|t(\mathbf{r})|^2$ represents the position-dependent tunneling matrix element that contains the exponential dependence on tip-sample distance. Usually, the spectral function of the tip, A_T is designed to be constant and the momentum-dependence of the tunneling matrix elements is ignored.

When measuring in *spectroscopic-imaging* mode (SI-STM), for each pixel on a chosen field of view a dI/dV spectrum is acquired at the tip-sample distance determined locally by the set-up conditions (V_s, I_s). The result of such a measurement is a three-dimensional dataset representing the local density of states as function of position and energy.

Because we determine the tip-sample distance at each point by the set-up conditions, the effect of the matrix element (assuming it is energy independent) is cancelled. However, the procedure does bring in an extra denominator:

$$\frac{dI}{dV}(eV, \mathbf{r}) = \frac{I_S A_S(eV, \mathbf{r})}{\int_0^{eV_S} A(E, \mathbf{r}) dE} \quad 2A.4$$

The procedure can thus introduce additional artifacts into the measured differential conductance dI/dV ^{28,56}, the so-called *set-up effect*.

A common way to reduce this effect is to choose set-up conditions far away from the Fermi level such that inhomogeneities in the integrated density of states average out, however, this is not always experimentally possible. Other methods include the use of the ratio between quantities with positive and negative bias⁵⁷, or the division of the differential conductance by the total conductance $(dI/dV)/(I/V)$ ²⁸⁻³⁰ - the approach that we also use in this paper. See **Figs. 2.5b-c, 2A.1, 2A.6** for comparisons. The current I is the *measured* current at that particular location and bias V , which means it is small but generally non-zero at the Fermi level. The voltage V is a value set in the experiment, implying for the Fermi level that the data would be multiplied by 0 in the normalization. To circumvent this, we manually add a 10uV (negligible to the energy scale set by temperature) offset in data processing.

The STM experiments reported in this paper have been performed with an ultra-high vacuum, home-built STM with exceptional stability, described elsewhere⁵⁸. All data was taken at a base temperature of 4.2K. Measurements are performed with a chemically etched tungsten tip that is prepared by field emission on a gold surface before measuring Sr₂RhO₄.

2A.2 Supplementary Figures

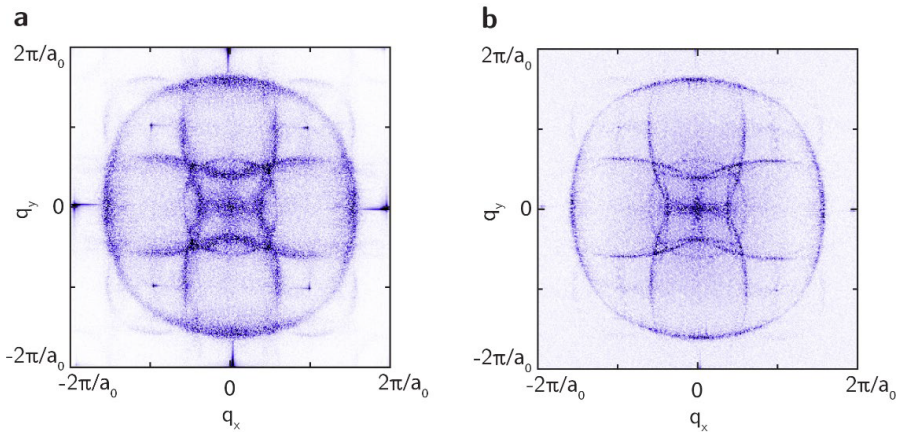


Figure 2A.1

Raw data of Fermi surfaces extracted from STM (not corrected for drift, without core suppression and not symmetrized) for both dI/dV (a) and $(dI/dV)/(I/V)$ (b).

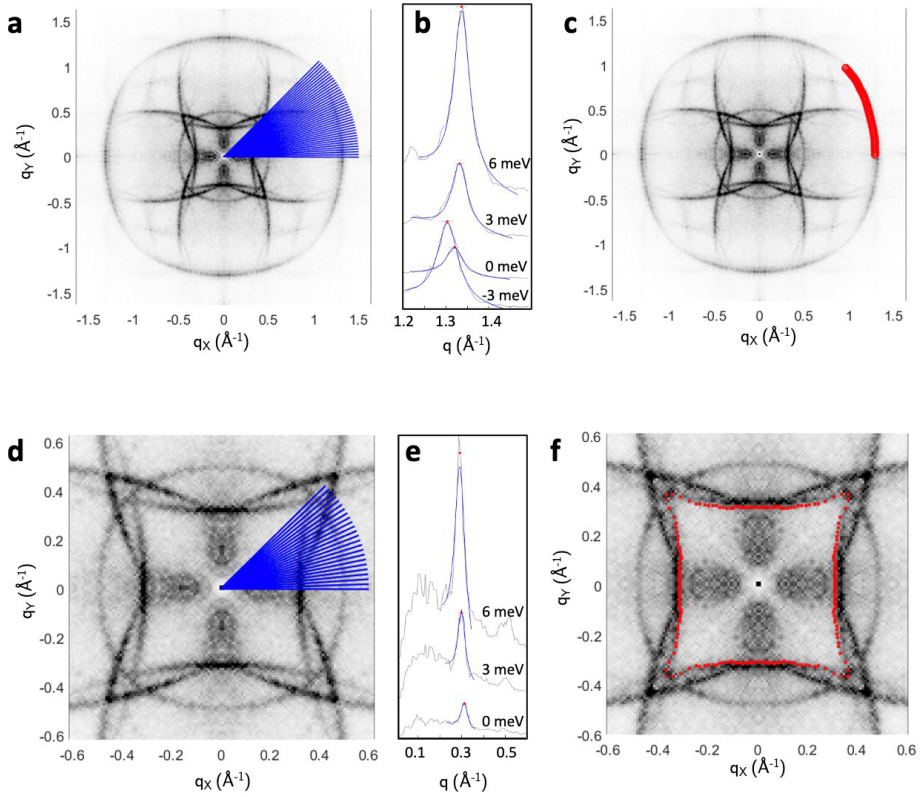


Figure 2A.2

Extraction of the points plotted in Fig. 2.1e and Fig. 2.4 for STM data. *a-c* Cuts along different angles are taken (blue lines) and fitted with Lorentzian function and a linear background. The image on the right shows the fitted points at the conductance layer at the Fermi level. *d-f* Analogous procedure for the QPI at low q .

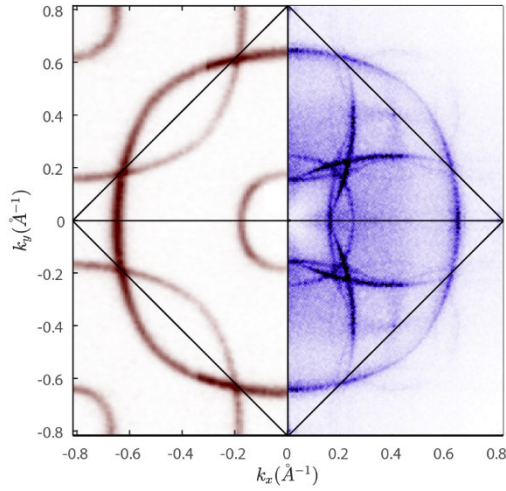


Figure 2A.3

Comparison of STM and ARPES Fermi surfaces. STM data has been processed as in Figure 1d and it is rescaled by a factor 2 to take account of the difference between scattering vectors seen with STM (q -space) and the direct momentum space probed by ARPES (k -space).

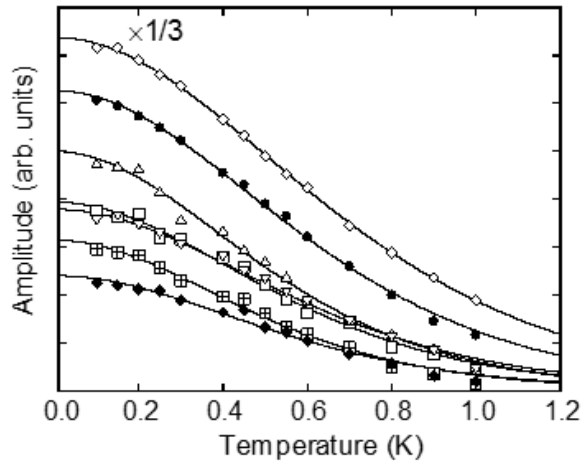


Figure 2A.4

Quantum oscillation. The dependence of the amplitude of the QO seven frequencies as a function of temperature with a Lifshitz-Kosevich fit used to extract the masses.

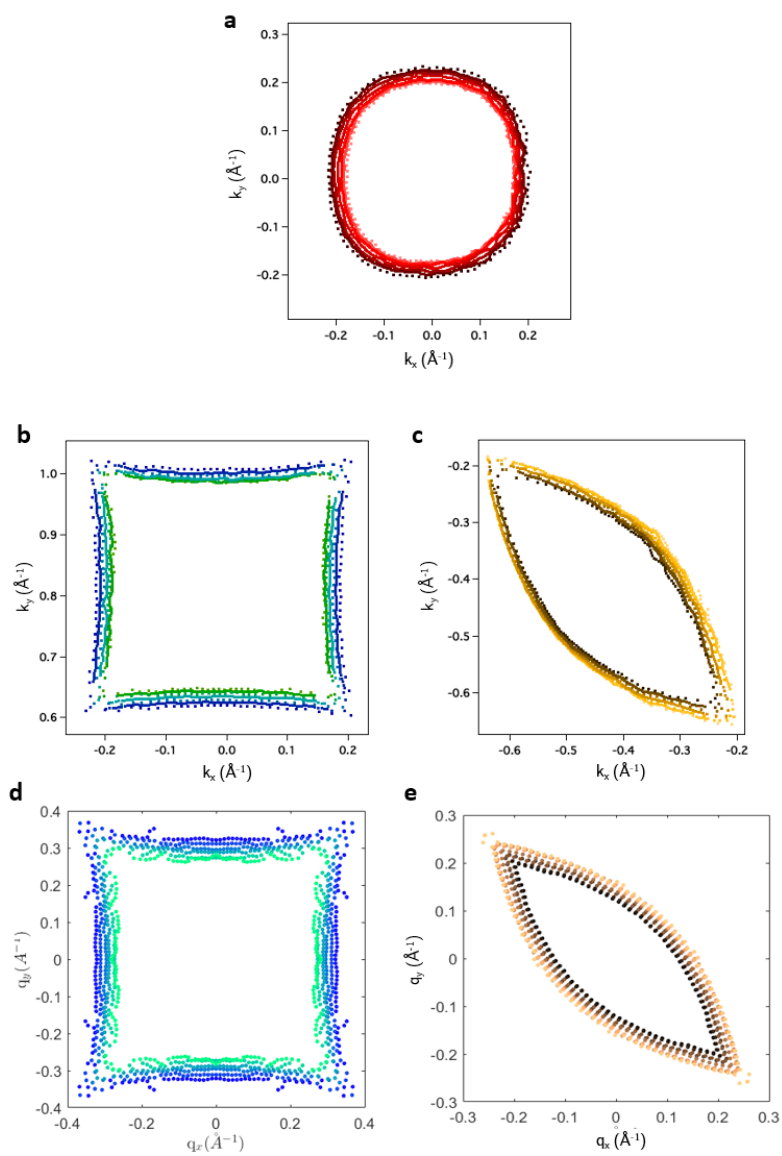


Figure 2A.5

The extracted Fermi surface pocket's volumes used for Fig. 2.4.

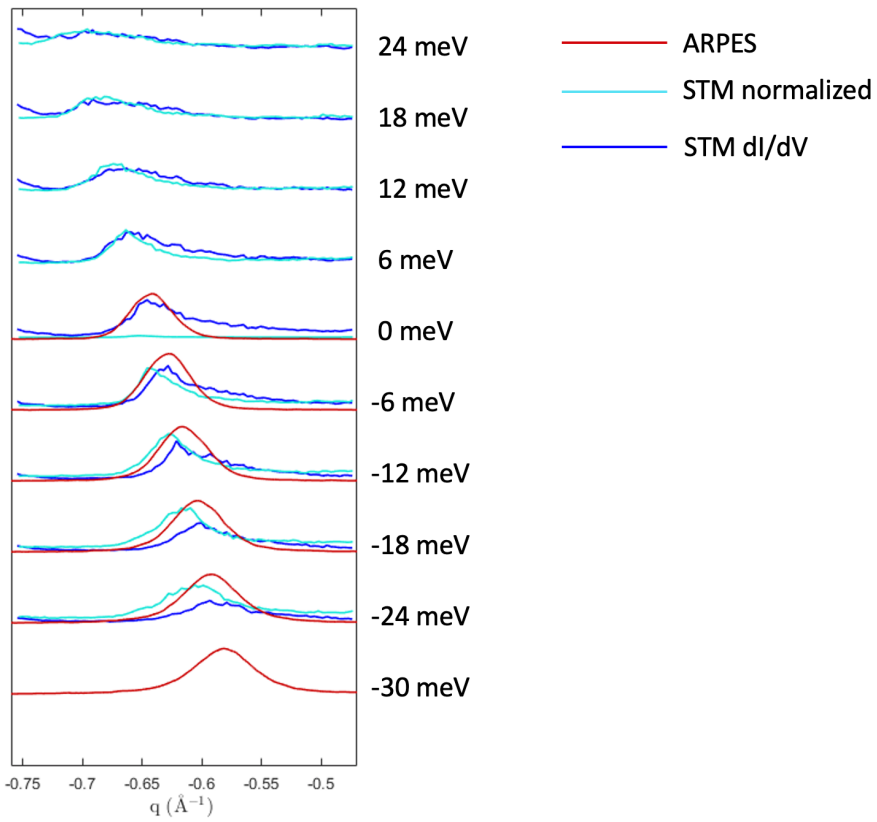


Figure 2A.6

Direct comparison of MDCs from ARPES and STM as shown in Fig. 2.5.

2.3 References

- [1] Keimer, B., Kivelson, S. A., Norman, M. R., Uchida, S. & Zaanen, J. From quantum matter to high-temperature superconductivity in copper oxides. *Nature* **518**, 179–86 (2015).
- [2] Johnston, D. C. The puzzle of high temperature superconductivity in layered iron pnictides and chalcogenides. *Adv. Phys.* **59**, 803–1061 (2010).
- [3] Coleman, P. Heavy fermions: electrons at the edge of magnetism, in *Handbook of Magnetism and Advanced Magnetic Materials* (John Wiley and Sons, 2007).
- [4] Imada, M., Fujimori, A. & Tokura, Y. Metal-insulator transitions. *Rev. Mod. Phys.* **70**, 1039–1263 (1998).
- [5] Sachdev, S. *Quantum phase transitions*. (Cambridge University Press, Cambridge, 2011).
- [6] Crommie, M. F., Lutz, C. P. & Eigler, D. M. Imaging standing waves in a two-dimensional electron gas. *Nature* **363**, 524–527 (1993).
- [7] Petersen, L., Hofmann, Ph., Plummer, E. W. & Besenbacher, F. Fourier transform–STM: determining the surface Fermi contour. *J. Electron Spectrosc. Relat. Phenom.* **109**, 97–115 (2000).
- [8] Fujita, K. *et al.* Spectroscopic Imaging STM: Atomic-scale visualization of electronic structure and symmetry in underdoped cuprates. Chapter 3 in *Theoretical methods for strongly correlated systems*, (Springer Berlin Heidelberg, 2012).
- [9] Yazdani, A., Eduardo, H., Neto, S. & Aynajian, P. Spectroscopic imaging of strongly correlated electronic states. *Annu. Rev. of Condens. Matter Phys.* **7**, 11 (2016)
- [10] Hüfner, S. *Photoelectron spectroscopy*. (Springer, Berlin, Heidelberg, 2003).
- [11] Baumberger, F. *et al.* Fermi surface and quasiparticle excitations of Sr_2RhO_4 . *Phys. Rev. Lett.* **96**, 246402 (2006).
- [12] Coleman, P. *Introduction to many-body physics*. (Cambridge University Press, Cambridge, 2013).
- [13] Damascelli, A., Hussain, Z. & Shen, Z. Angle-resolved photoemission studies of the cuprate superconductors. *Rev. Mod. Phys.* **75**, (2003).
- [14] Sebastian, S. E. & Proust, C. Quantum oscillations in hole-doped cuprates. *Annu. Rev. Condens. Matter Phys.* **6**, 411–430 (2015).
- [15] McElroy, K. *et al.* Elastic scattering susceptibility of the high temperature superconductor $\text{Bi}_2\text{Sr}_2\text{CaCu}_2\text{O}_{8+\delta}$: a comparison between real and momentum space photoemission spectroscopies. *Phys. Rev. Lett.* **96**, 067005 (2006).
- [16] Markiewicz, R. S. Bridging k and q space in the cuprates: Comparing angle-resolved photoemission and STM results. *Phys. Rev. B - Condens. Matter Mater. Phys.* **69**, 1–10 (2004).
- [17] Vishik, I. M. *et al.* A momentum-dependent perspective on quasiparticle interference in $\text{Bi}_2\text{Sr}_2\text{CaCu}_2\text{O}_{8+\delta}$. *Nat. Phys.* **5**, 718–721 (2009).
- [18] Hashimoto, M. *et al.* Reaffirming the d -wave superconducting gap using the

- autocorrelation angle-resolved photoemission spectroscopy. *Phys. Rev. Lett.* **106**, 167003 (2011).
- [19] Kirchner, S. *et al.* Heavy-electron quantum criticality and single-particle spectroscopy. *Rev. Mod. Phys.* **92**, 011002 (2020)
- [20] Matt, C. E. *et al.* Consistency between ARPES and STM measurements on SmB₆. *Phys. Rev. B* **101**, 085142 (2020).
- [21] Kim, B. J. *et al.* Missing *xy*-band Fermi surface in 4d transition-metal oxide Sr₂RhO₄: Effect of the octahedra rotation on the electronic structure. *Phys. Rev. Lett.* **97**, 106401 (2006).
- [22] Perry, R. S. *et al.* Sr₂RhO₄: a new, clean correlated electron metal. *New J. Phys.* **8**, 175–175 (2006).
- [23] Baumberger, F. *et al.* Nested Fermi surface and electronic instability in Ca₃Ru₂O₇. *Phys. Rev. Lett.* **96**, 107601 (2006).
- [24] Haverkort, M. W., Elfimov, I. S., Tjeng, L. H., Sawatzky, G. A. & Damascelli, A. Strong spin-orbit coupling effects on the Fermi surface of Sr₂RuO₄ and Sr₂RhO₄. *Phys. Rev. Lett.* **101**, 26406 (2008).
- [25] Liu, G., Antonov, V. N., Jepsen, O. & Andersen, O. K. Coulomb-enhanced spin-orbit splitting: the missing piece in the Sr₂RhO₄ puzzle. *Phys. Rev. Lett.* **101**, 026408 (2008).
- [26] Kim, M., Mravlje, J., Ferrero, M., Parcollet, O. & Georges, A. Spin-orbit coupling and electronic correlations in Sr₂RuO₄. *Phys. Rev. Lett.* **120**, 126401 (2018).
- [27] Tamai, A. *et al.* High-resolution photoemission on Sr₂RuO₄ reveals correlation-enhanced effective spin-orbit coupling and dominantly local self-energies. *Phys. Rev. X* **9**, 021048 (2019).
- [28] Feenstra, R. M., Stroscio, J. A. & Fein, A. P. Tunneling spectroscopy of the Si(111)2x1 surface. *J. Vac. Sci. Technol. B* **5**, 295–306 (1987).
- [29] Hanaguri, T. *et al.* Two distinct superconducting pairing states divided by the nematic end point in FeSe_{1-x}S_x. *Sci. Adv.* **4**, 6419 (2018).
- [30] Kostin, A. *et al.* Imaging orbital-selective quasiparticles in the Hund's metal state of FeSe. *Nat. Mater.* **17**, 869–874 (2018).
- [31] Macdonald, A. J. *et al.* Dispersing artifacts in FT-STs: a comparison of set point effects across acquisition modes. *Nanotechnology* **27**, 414004 (2016).
- [32] Allan, M. P. *et al.* Imaging Cooper pairing of heavy fermions in CeCoIn₅. *Nat. Phys.* **9**, 468–473 (2013).
- [33] Wang, Z. *et al.* Quasiparticle interference and strong electron-mode coupling in the quasi-one-dimensional bands of Sr₂RuO₄. *Nat. Phys.* **13**, 799-805 (2017).
- [34] Allan, M. P. *et al.* Anisotropic energy gaps of iron-based superconductivity from intraband quasiparticle interference in LiFeAs. *Science* **336**, 563-567 (2012).
- [35] Hess, C. *et al.* Interband quasiparticle scattering in superconducting LiFeAs reconciles photoemission and tunneling measurements. *Phys. Rev. Lett.* **110**, 017006 (2013).
- [36] Wang, Q. & Lee, D. Quasiparticle scattering interference in high-temperature superconductors. *Phys. Rev. B* **67**, 020511 (2003).
- [37] Capriotti, L., Scalapino, D. J. & Sedgewick, R. D. Wave-vector power spectrum

- of the local tunneling density of states: Ripples in a d -wave sea. *Phys. Rev. B* **68**, 014508 (2003).
- [38] Nunner, T. S., Chen, W., Andersen, B. M., Melikyan, A. & Hirschfeld, P. J. Fourier transform spectroscopy of d -wave quasiparticles in the presence of atomic scale pairing disorder. *Phys. Rev. B - Condens. Matter Mater. Phys.* **73**, 1–7 (2006).
- [39] Sulangi, M. A., Allan, M. P. & Zaanen, J. Revisiting quasiparticle scattering interference in high-temperature superconductors: the problem of narrow peaks. *Phys. Rev. B* **96**, 134507 (2017).
- [40] Choubey, P., Kreisel, A., Berlijn, T., Andersen, B. M. & Hirschfeld, P. J. Universality of scanning tunneling microscopy in cuprate superconductors. *Phys. Rev. B* **96**, 174523 (2017).
- [41] Schoenberg, D. *Magnetic oscillations in metals*. (Cambridge University Press, Cambridge, 1984).
- [42] Bürgi, L., Jeandupeux, O., Brune, H. & Kern, K. Probing hot-electron dynamics at surfaces with a cold scanning tunneling microscope. *Phys. Rev. Lett.* **82**, 4516 (1999).
- [43] Allan, M. P. *et al.* Identifying the ‘fingerprint’ of antiferromagnetic spin fluctuations in iron pnictide superconductors. *Nat. Phys.* **11**, 177–182 (2014).
- [44] Dahm, T. & Scalapino, D. J. Quasi-particle interference probe of the self-energy. *New J. Phys.* **16**, 023003 (2014).
- [45] Sulangi, M. A. & Zaanen, J. Self-energies and quasiparticle scattering interference. *Phys. Rev. B* **98**, 094518 (2018).
- [46] Chaplik, A.V. Energy spectrum and electron scattering processes in inversion layers. *Sov. J. Exp. Theor. Phys.* **33**, 997 (1971).
- [47] Giuliani, G. F. & Quinn, J. J. Lifetime of a quasiparticle in a two-dimensional electron gas. *Phys. Rev. B* **26**, 4421 (1982).
- [48] Fukuyama, H. & Abrahams, E. Inelastic scattering time in two-dimensional disordered metals. *Phys. Rev. B* **27**, 5976 (1983).
- [49] Smith, N. V., Thiry, P. & Petroff, Y. Photoemission linewidths and quasiparticle lifetimes. *Phys. Rev. B* **47**, 15476 (1993).
- [50] Martins, C., Aichhorn, M., Vaugier, L. & Biermann, S. Reduced effective spin-orbital degeneracy and spin-orbital ordering in paramagnetic transition-metal oxides: Sr_2IrO_4 versus Sr_2RhO_4 . *Phys. Rev. Lett.* **107**, 266404 (2011).
- [51] Martins, C *et al*, Coulomb correlations in 4d and 5d oxides from first principles – or how spin-orbit materials choose their effective orbital degeneracies. *J. Phys.: Condens. Matter* **29**, 263001 (2017)
- [52] Bergemann, C., Mackenzie, A. P., Julian, S. R., Forsythe, D. & Ohmichi, E. Quasi-two-dimensional Fermi liquid properties of the unconventional superconductor Sr_2RuO_4 . *Adv. Phys.* **52**, 639-725 (2003).
- [53] Hoesch, M. *et al.* A facility for the analysis of the electronic structures of solids and their surfaces by synchrotron radiation photoelectron spectroscopy. *Rev. Sci. Instrum.* **88**, 013106 (2017).
- [54] Chen, C. J. *Introduction to scanning tunneling microscopy*. (Oxford University Press, Oxford, 2007).
- [55] Meevasana, W. *et al.* Hierarchy of multiple many-body interaction scales in high-temperature superconductors. *Phys. Rev. B* **75**, 174506 (2007).

- [56] Macdonald, A. J. *et al.* Dispersing artifacts in FT-STs: a comparison of set point effects across acquisition modes. *Nanotechnology* **27**, 414004 (2016).
- [57] Kohsaka, Y. *et al.* An intrinsic bond-centered electronic glass with unidirectional domains in underdoped cuprates. *Science* **315**, 1380–1385 (2007).
- [58] Battisti, I., Verdoes, G., van Oosten, K., Bastiaans, K. M. & Allan, M. P. Definition of design guidelines, construction, and performance of an ultra-stable scanning tunneling microscope for spectroscopic imaging. *Rev. Sci. Instrum.* **89**, 123705 (2018).

3 Puddle Formation, Persistent Gaps, and non-mean-field Breakdown of Superconductivity in Overdoped $(\text{Pb,Bi})_2\text{Sr}_2\text{CuO}_{6+\delta}$

This chapter has been accepted as
Tromp et al. in *Nature Materials*

The cuprate high-temperature superconductors exhibit many unexplained electronic phases, but it was often thought that the superconductivity at sufficiently high doping is governed by conventional mean-field Bardeen-Cooper-Schrieffer (BCS) theory¹. However, a series of measurements show that the number of paired electrons (the superfluid density) vanishes when the transition temperature T_c goes to zero²⁻⁴, in contradiction to expectation from BCS theory. The origin of this anomalous vanishing is unknown. Our scanning tunneling spectroscopy measurements in the overdoped regime of the $(\text{Pb,Bi})_2\text{Sr}_2\text{CuO}_{6+\delta}$ high-temperature superconductor show that it is due to the emergence of puddled superconductivity, featuring nanoscale superconducting islands in a metallic matrix⁵⁻⁷. Our measurements further reveal that this puddling is driven by gap filling, while the gap itself persists beyond the breakdown of superconductivity. The important implication is that it is not a diminishing pairing interaction that causes the breakdown of superconductivity. Unexpectedly, the measured gap-to-filling correlation also reveals that pair-breaking by disorder does not play a dominant role and that the mechanism of superconductivity in overdoped cuprate superconductors is qualitatively different from conventional mean-field theory.

3.1 Introduction

The essence of high-temperature superconductivity in the cuprates revolves around doping a Mott insulator. Superconductivity emerges when hole-doping is greater than 5% per lattice site; T_c initially increases through the underdoped (UD) region of the phase diagram, before it decreases again in the overdoped (OD) region¹. Superconductivity breaks down completely at roughly 27% doping. For the strongly overdoped region (SOD), it is often assumed that screening sufficiently reduces electron-electron correlations for a Fermi liquid to appear⁸⁻¹⁰. The superconducting state is then of the Bardeen-Cooper-Schrieffer (BCS) type, and the suppression of superconductivity is a consequence of a diminishing pairing interaction. Evidence for such conventional behavior in the OD regime comes from photoemission experiments, which suggest the existence of a full Fermi surface with superconductivity, as indicated by an energy gap that opens up in a BCS fashion below T_c ^{11,12}. As a caveat, very recent magneto-transport experiments indicate that even at high doping the normal state has strange metal features¹³.

The first surprise in this regard was the discovery that the superfluid density decreases linearly to zero with doping beyond optimal doping^{2-4,14,15}, contrary to the BCS expectation that it should be of the order of the total carrier density and hence proportional to the doping level^{1,2}. Additionally, optical conductivity measurements revealed a large density of metallic carriers below T_c ¹⁴, suggesting a filling of the superconducting gap due to pair breaking. One possible explanation for these observations involves potential disorder, reducing the electron mean free path, at length scales comparable to the small coherence length that is typical for the cuprates^{5-7,16}. According to Bogoliubov-de Gennes (BdG) theory (i.e. BCS in spatially heterogeneous systems), disorder at these length scales leads to emergent granular superconductivity^{6,17-23}, i.e. puddles of well-developed superconductivity with a size set by the coherence length, separated by regions where the gap is suppressed. The resulting weak-link superconductor will show a low superfluid density.

We investigate these issues using scanning tunneling spectroscopy which yields the spatial distribution of the electron density of states with atomic-scale precision. Our measurements show that in $(\text{Pb,Bi})_2\text{Sr}_2\text{CuO}_{6+\delta}$ (Bi2201) which has one CuO_2 layer per unit cell and is known to have a high residual resistivity¹³, such a “puddled” superconductor does indeed develop at high

doping (**Figs. 3.1,3.2**). The typical spatial extent of the puddles is a few nanometers, of the order of the small coherence length in this system (**Fig. 3.3**). Our measurements additionally reveal that the superconducting gap persists beyond the dome, and that instead the heterogeneity is driven by gap filling (**Fig. 3.4**). This strongly suggests that the breakdown of superconductivity is not a result of a vanishing pairing interaction. A comparison with BdG simulations suggests that this filling is likely due to the decay of the Cooper pairs in surrounding metallic areas, which in turn explains the observation of a large density of metallic carriers. Unexpectedly, we also find a striking violation of a basic BdG rule. Within BdG theory, pair breaking goes hand-in-hand with gap closing, because depletion of the number of Cooper pairs in a superconductor leads to a diminishment of the gap magnitude Δ as well:

$$\Delta = V \sum_{\mathbf{k}} \langle c_{\mathbf{k}\uparrow}^\dagger c_{-\mathbf{k}\downarrow}^\dagger \rangle \quad (3.1)$$

where V is the attractive interaction and the c^{\prime} 's are electron field operators. Instead, our data show that the puddles characterized by the largest gap magnitudes exhibit also the largest gap filling (**Fig. 3.4c**), and that the average gap magnitudes are barely depending on doping (**Fig. 3.4a**). We therefore conclude that the physics governing the superconducting transition is of a different, non-mean-field kind.

3.2 Results & Discussion

To arrive at these findings, we study a series of Bi2201 samples with eight different doping levels, from underdoped to beyond the superconductor-metal transition, with an emphasis on the strongly overdoped regime. We chose Bi2201 because it has only one CuO_2 plane per unit cell, and has a rather large residual resistivity²⁴, suggesting that disorder is exceptionally important. On each sample, we measure the atomic-scale-resolved differential conductance $g(E, \mathbf{r})$ as a function of bias energy E and location \mathbf{r} , which is proportional to the Bogoliubov quasiparticle density of states.

We first consider the spatially averaged $g(E)$ spectra obtained at 4.2 K (**Fig. 3.1a**). Consistent with earlier reports²⁵⁻²⁸, crossing into the overdoped regime, the spectra acquire an increasingly large non-zero Bogoliubov quasiparticle

density of states at the Fermi level. This is remarkable as this quantity should go to zero for a standard d-wave BCS superconductor, but it is consistent with results from optical conductivity measurements¹⁴. It remains to be seen whether ARPES, if performed in SOD regions with such small gaps, would observe a similar phenomenology both in Bi2201 and Bi2212. We investigate this phenomenology using individual spectra, as in a heterogeneous situation like this, the average spectra do not represent the phenomenology adequately (**Figs. 3.1b-d**).

3.2.1 Gap Closure vs. Gap Filling

Next, we use a phenomenological model to fit all spectra over the whole doping range to extract the superconducting gap and gap filling of each individual spectrum. We calculate the spectral weight on each point $\mathbf{k} = (k_x, k_y)$ on the Fermi surface using a Dynes formula with superconducting gap

$$\Delta_{\mathbf{k}} = \Delta(\cos k_x - \cos k_y)/2 \quad (3.2)$$

where Δ is the maximal gap, and then average over the Fermi surface²⁷. We use the Dynes formula³⁰⁻³² as a mere phenomenological description constructed to reveal characteristic scales for the observed gap size and the gap filling, and discuss interpretational concerns after the presentation of the data. Our model yields the following function for the modeled differential conductance:

$$g(E) = P(E) * \langle \text{Dynes}(E, \Delta_{\mathbf{k}}, \Gamma) \rangle_{FS} = P(E) * \langle \text{Re} \left(\frac{E + i\Gamma}{\sqrt{(E + i\Gamma)^2 - \Delta_{\mathbf{k}}^2}} \right) \rangle_{FS} \quad (3.3)$$

where $\langle \rangle_{FS}$ indicates the average over the Fermi surface, $P(E)$ is a third-degree polynomial function to account for background variation, and $\text{Dynes}(E, \Delta_{\mathbf{k}}, \Gamma)$ is the Dynes function with the pair-breaking parameter Γ . For this study, we concentrate on the superconducting gap and thus restrict ourselves to a ± 15 meV range (in the underdoped and optimally doped range, which are not the focus of this paper, a pseudogap exists at a larger energy scale, as indicated by the red arrows in **Fig. 3.1a**). Lastly, we convolute $g(E)$ with a Gaussian function to account for spectrum broadening due to a finite temperature and the lock-in modulation.

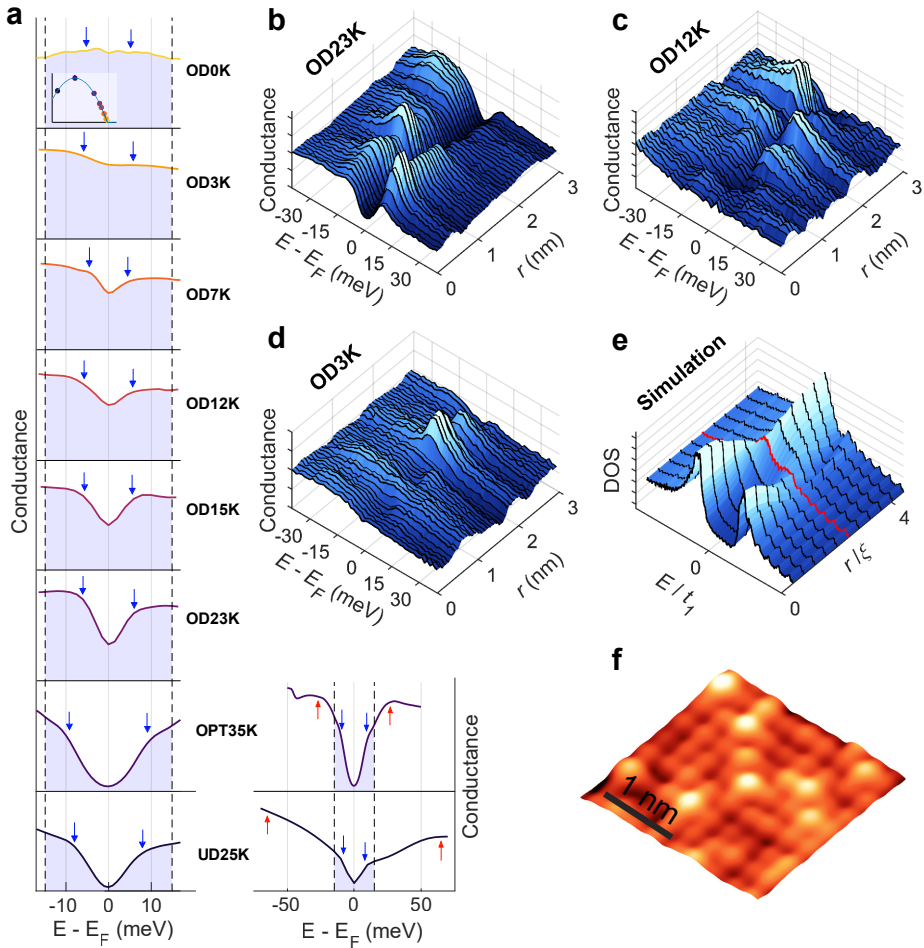


Figure 3.1 Heterogeneous gap filling in Bi2201.

a) The average spectra of eight different doping levels, labeled by their T_c . The shaded areas indicate the energy range used in the fitting procedure. The blue arrows show the average extracted gap magnitude. For the UD25K and OPT35K samples, the red arrows indicate the pseudogap as determined by He et al.²⁷. The inset in the top spectrum indicates the position of the samples on the superconducting dome. **b-d)** Spectra along 3 nm linecut for the OD23K, OD12K, and OD3K samples respectively. These raw, unprocessed spectra indicate the high degree of electronic inhomogeneity in these samples. **e)** A linecut of spectra from a self-consistent BdG simulation from the center of a superconducting puddle ($r = 0$) to the metallic environment which shows the van Hove singularity modeled to be close to the Fermi level (see Chapter 3A.4 for details). The boundary of the puddle is indicated by the red spectrum. The pairing interaction is nonzero inside the puddle (i.e., inside the red line) and is zero outside it. The energy unit is relative to the hopping parameter t_1 , and the length unit is relative to the coherence length ξ (see Chapter 3A.4). **f)** Typical topography measured on the OD12K sample on the same length scale as Figs. 3.1b-d.

We define the filling parameter F as the ratio $g(E = 0, T \rightarrow 0)/P(E = 0)$, which can be expressed in terms of our fitting parameters as:

$$F = \left\langle \frac{1}{\sqrt{1 + (\Delta_{\mathbf{k}}/\Gamma)^2}} \right\rangle_{FS} \quad (3.4)$$

Figs. 3.2a,b illustrate how the model differentiates between gap closure, controlled by Δ , and gap filling, controlled by Γ or F . **Fig. 3.2c** shows some typical spectra and fits from various locations. It is clear that, when compared to the scenarios presented in **Figs. 3.2a,b**, the measured spectra look more similar to the filling scenario as opposed to the closing scenario. We then fit roughly 10^5 spectra from 8 different doping levels with this model, and display the extracted gap size and gap filling in **Fig. 3.3**. We note that for the strongly overdoped samples, high signal-to-noise is key for successful fits; the traces shown in **Figs. 3.1b-d** and **Fig. 3.2c** are raw spectra without any averaging. A further challenge is that at higher doping, a significant fraction of spectra exhibit completely gapless regions. We identify such spectra after fitting and exclude them from subsequent analysis. In the appendix 3A, we provide details (see Chapter 3A.2 and **Fig. 3A.4**) and demonstrate that our key results are independent of these choices. We also provide a modified version of the model with an alternative definition of the gap filling, and show that our results are independent of the precise definition of gap filling.

3.2.2 Persistent Superconducting Gap & Gap Filling

We start our discussion with the spatial maps of the gap size $\Delta(\mathbf{r})$ as a function of doping (**Figs. 3.3b-d**). Strikingly, while more spectra are fully filled at higher doping, the average gap size remains roughly constant on the strongly overdoped side (**Fig. 3.3a**). Initially, the gap size increases when moving from underdoped to optimally doped. Beyond optimal doping, the gap size barely decreases anymore when going through the OD and SOD side, and instead remains roughly constant – even beyond the superconductor-to-metal transition. In particular, throughout the SOD region, we observe an almost constant average gap amplitude even though T_c is rapidly decreasing. Our study thus excludes a homogeneously diminishing pairing interaction as the cause of the superconductor-to-metal transition.

Given a constant gap, what drives the changes in spectra on the overdoped side? Our analysis indicates that it is the gap filling. We extract the gap filling,

F , using Eq. (2), for each measured sample, and present the distribution of the gap fillings in **Figs. 3.3f-h**, and their histograms in **Fig. 3.3e**. Remarkably, the mean gap filling changes considerably over the doping range. In the OP region, the spectra have a filling close to zero, i.e. they are fully gapped. Crossing into the OD regime, a subset of spectra starts to develop a finite gap filling. This subset grows with further doping, with all spectra having a

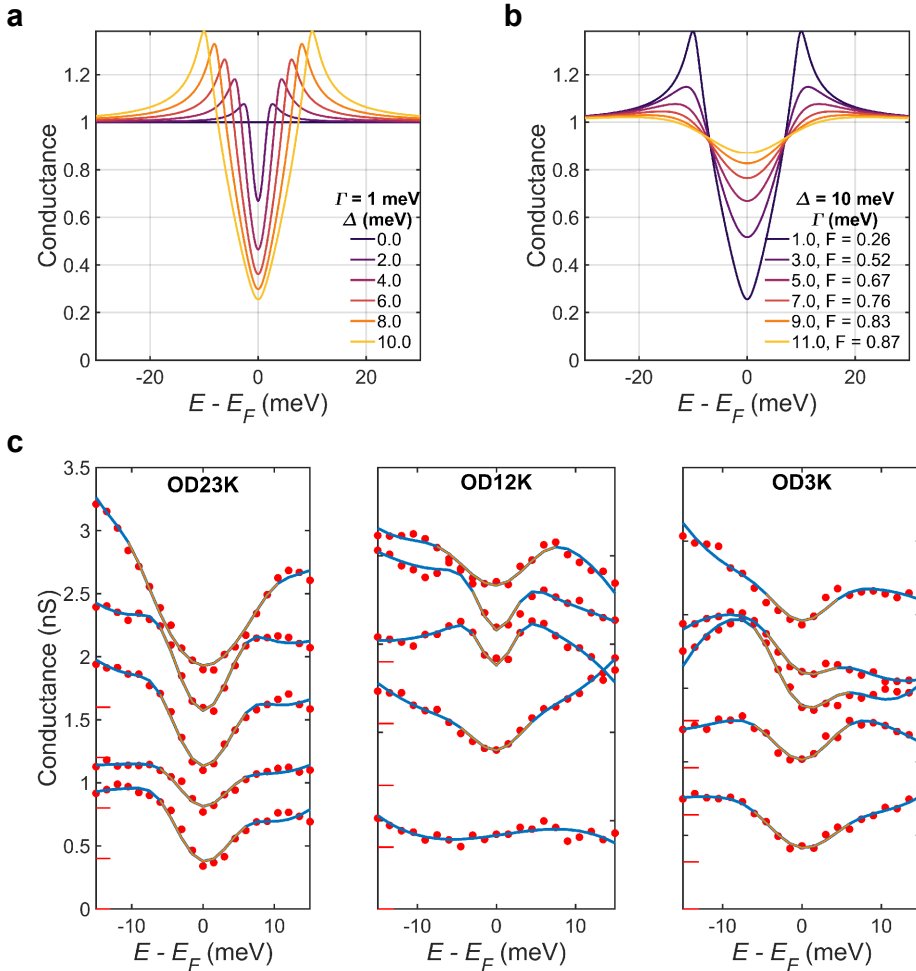


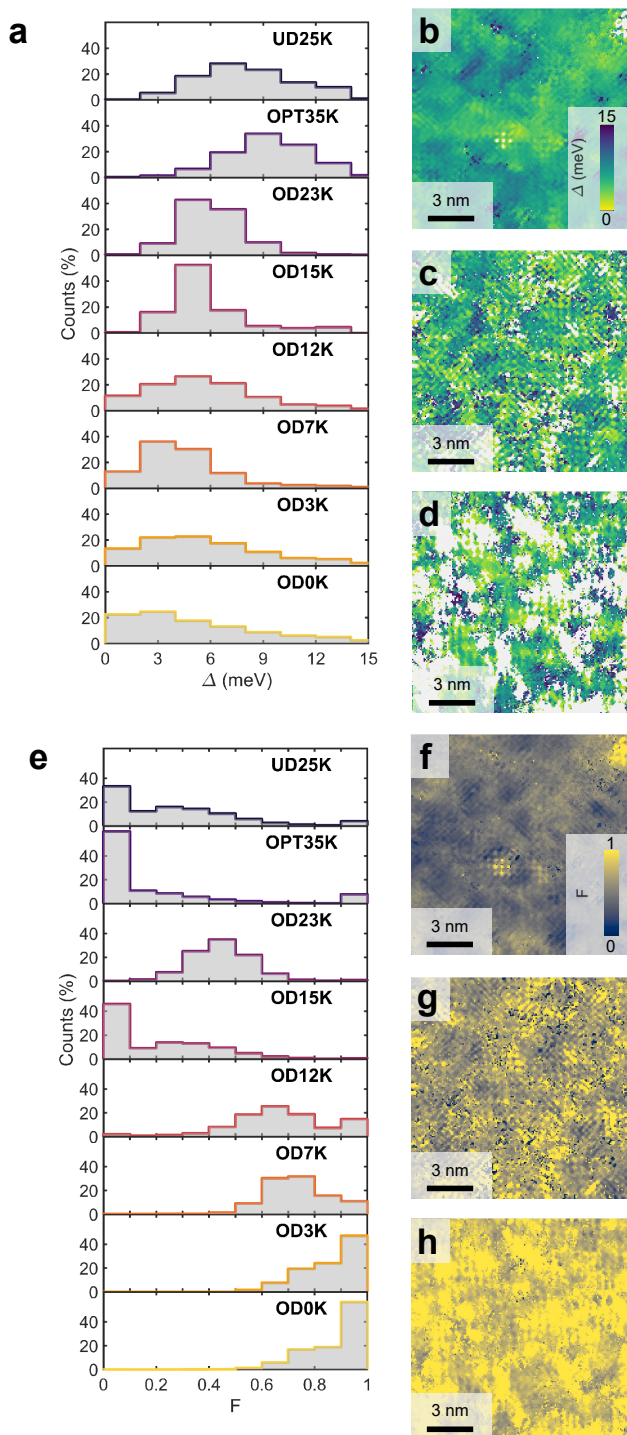
Figure 3.2 Gap filling versus gap closure.

Difference between gap closure (a) and gap filling (b) by presenting a sweep of the gap magnitude parameter Δ for constant Γ , and a sweep of the scattering rate parameter Γ for constant Δ , respectively. c) Example fits from our model applied to our raw data for the OD23K, OD12K, and OD3K data. The zeros of the spectra are offset for better visibility, as indicated by the red marks. The black marks indicate the gap width as determined by the model.

finite filling in the SOD regime. The values of F shift markedly in this doping regime from nearly fully gapped ($F = 0$) near optimal doping to almost fully filled ($F = 1$) towards the SOD regime and extending into the metallic regime. The trends in gap closing and gap filling are summarized in **Fig. 3.4a,b**: as the doping is increased into the overdoped regime, the gap size remains roughly constant; in contrast, the gap filling increases rapidly. Thus, a first key result of this paper is that it is not a decaying gap width Δ , but an increasing gap filling F that is responsible for the diminishing superconductivity and eventually drives the superconductor-to-metal transition. We also note that the persistence of the superconducting gap we observe is remarkably similar to the persistent spin gap observed in a similar doping range³³.

Notably, the gap filling is highly heterogenous, as can be seen from the width of the distributions in **Figs. 3.3e** and in the spatial maps in **Fig. 3.3f-h**. We observe areas both with and without a gap, each existing at a length scale consistent with the coherence length (~ 1.5 nm). Some spectra exhibit a peak that can be associated with a van Hove singularity (vHS) as reported previously^{25,26}; but we note that it is a highly anomalous one: both the energy and the amplitude of the peak vary in space on length-scales that are not consistent with the spatially averaged anti-nodal signature observed in photoemission^{34,35}. Further, we only find this peak in the SOD regime, whereas ARPES measurements suggest that the vHS should be observable in lower doped samples as well, at energies still easily measurable by STM. The question of the vHS in STM data remains open. Notwithstanding the vHS, our observations indicate that the breakdown of superconductivity in the overdoped regime of the single-layer bismuth cuprate is likely caused by an emergent strongly inhomogeneous superconductivity, leading to an effective weak-link physics that explains the diminishing superfluid density. Hence, at first glance, our data suggest that theoretical models involving disorder-driven breakdown of superconductivity in the BdG framework^{5-7,16-19,22,23} are a good description of the physics of strongly overdoped Bi2201, with the additional information that it is the gap filling that drives the formation of the superconducting puddles.

Figure 3.3 Doping dependence of the spatially resolved gap filling and gap magnitude. *a)* Gap magnitude histogram for each doping concentration. *b-d)* The spatial distributions of the gap magnitude for the OD23K, OD12K, and OD3K samples. The spectra that are omitted from the histograms (see Chapter 3A.2) are indicated by the white areas in **Figs. 3.3b-d.** *e)* Gap filling histogram for each doping level. *f-h)* Spatial distribution of the gap filling for the OD23K, OD12K, and OD3K samples respectively.



Next, we focus on the origin of the gap filling. According to BdG theory, the excitations that fill the gap are quasiparticles of the Fermi-liquid normal state that are released by breaking up Cooper pairs. Well-known causes for pair breaking are potential disorder^{5-7,16} (for a d-wave superconductor) and thermal phase fluctuations³⁵⁻³⁸. However, if potential disorder were the only culprit, the areas where the pair breaking is smallest (where superconductivity survives best) should have the largest gaps, which is not what we observe. We demonstrate this in **Fig. 3.4c**, where we show the local relationship between the gap size Δ and the pair breaking Γ , and find a clear positive correlation between the two. Further, we can exclude thermal phase fluctuations based on our temperature dependent measurements, up to 20 K for the OD9K sample. Thermal phase fluctuations should lead to a strongly temperature-dependent filling, in contrast to our observations (see Chapter 3A.3).

3.2.3 Cooper Pair Decay in a Metallic Matrix

We therefore consider an alternative candidate for pair breaking: the decay of Cooper pairs into smaller gap or metallic regions, as previously suggested³⁹⁻⁴¹. This can be seen as akin to an inverse proximity effect⁴². We are not aware of self-consistent simulations for this scenario in the literature, but they are possible with state-of-the-art numerical methods. We start with a large real-space supercell implementing a realistic tight-binding band structure. We then introduce the superconducting puddles by switching on a local pairing interaction characterized by a linear dimension L that is approaching the (bulk) coherence length. The BdG equations are then solved self-consistently (see Chapter 3A.4 for further details) and typical outcomes are shown in **Fig. 3.1e**. The simulated spectra are surprisingly similar to the experimental ones, and one might wonder whether this gap-filling dominated physics is connected to certain disordered superconductors^{21,22,43,44} and interface superconductors⁴⁵ with a local density of states phenomenology that is not dissimilar from what we observe here.

However, there is one aspect of our data that is markedly inconsistent with the BdG description of granular superconductors. Our data shows that the largest gaps also exhibit the strongest gap filling (**Fig. 3.4c**), while within BdG, gap filling should always go hand-in-hand with a decrease of the gap magnitude. Our self-consistent simulations confirm that this is indeed also valid for the heterogeneous case: upon application of our fitting model to the calculated spectra shown in **Fig. 3.1e**, we find that the regions with the largest gaps show the least amount of pair breaking as shown in **Fig. 3.4d**. We

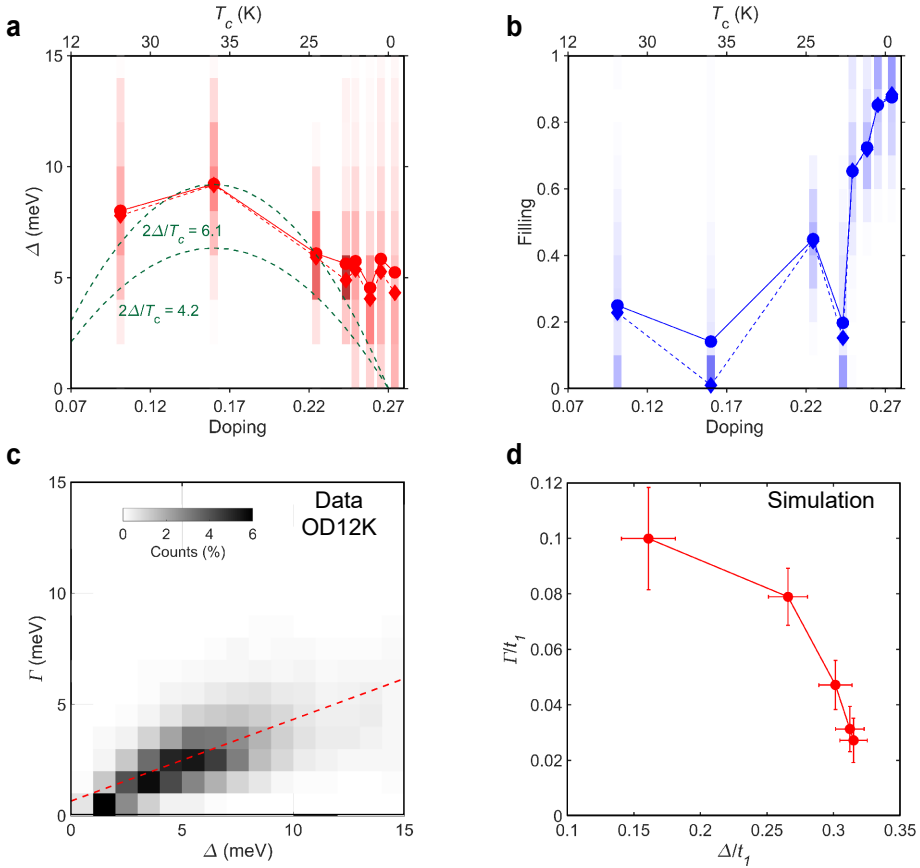


Figure 3.4 Gap filling driven breakdown of superconductivity and the contradiction to BdG.

a,b) The mean (circles) and median (diamonds) of the gap magnitude and the gap filling, respectively. The shaded areas represent the local variations in the gap magnitudes and fillings by depicting the histograms. The green dashed lines in **Fig. 3.4a** show the expectation of a gap size proportional to T_c with a proportionality constant either chosen to match the OPT35K data point, or determined by weakly coupled d -wave BCS theory. The doping levels were calculated using the Presland formula for the superconducting samples, and using the anti-nodal band shift measured by photoemission for the OD0K sample (see Chapter 3A.5). **c)** 2D histogram of the measured local relation between gap magnitude Δ and pair-breaking parameter Γ for the OD12K sample. The positive correlation between the two is indicated by the red line. **d)** The relation between the gap magnitude and pair-breaking parameter extracted from self-consistent BdG simulations (**Fig. 3.1e**) using the same fitting model. In contrast to **Fig. 3.4c** we find a clear negative correlation. The error bars indicate the uncertainty in the obtained values due to the fitting process.

note that self-consistency in the calculations is necessary here; fixing the gap magnitude artificially would obscure any effect from pair breaking on the gap magnitude. The comparison between **Fig. 3.4c** and **Fig. 3.4d** shows a striking inconsistency between the experiment and BdG expectation.

3.3 Conclusion & Outlook

In summary, our real-space imaging reveals a strongly heterogeneous superconductivity consisting of superconducting puddles with a size set by the coherence length immersed in a metallic matrix. This explains the diminishing superfluid density²⁻⁴ and the origin of the large fraction of metallic carriers¹⁴: it stems from the filling of the gap. Our data further demonstrate that superconductivity does not, as it is often assumed, become conventional in the SOD regime. The breakdown of superconductivity is not the consequence of a vanishing pairing interaction and does not follow the BdG description. Furthermore, the gap filling is entirely different from simple quasiparticles populating the gap and counting the number of broken BCS Cooper pairs. Instead, what fills the gap might be related to the strange normal state¹³, e.g. collective excitations of an unknown kind rooted in the “strange metal” physics, which at present cannot be calculated, or to electrons from a different sector, but not by means of simple pair-breaking. Last but not least, this unconventional physics may not be limited to the low-temperature, overdoped regime. STM studies at optimal doping of Bi2212 showed a rather similar puddling effect upon approaching the superconducting transition temperature^{40,46}. This may imply that the physics of the thermal transition – the “high T_c ” problem itself – is governed by unknown physics. It would be interesting to revisit this high-temperature regime to make this more precise.

3A Appendix

3A.1 Experimental Methods

We performed a systematic study on a series of $(\text{Pb,Bi})_2\text{Sr}_2\text{CuO}_{6+\delta}$ samples with 8 distinct doping levels, covering the range from underdoped (UD25K) to strongly overdoped (OD0K) side. Single crystal samples were grown by the conventional floating-zone technique^{13,27}. The UD25K, OP35K, and OD15K samples contain La doping, i.e. $(\text{Pb,Bi})_2(\text{La,Sr})_2\text{CuO}_{6+\delta}$ while the rest of the samples are without La doping. The doping levels, transition temperatures T_c , and measurement temperatures are listed in Table S1. The doping levels of the superconducting samples are determined using the Presland formula, while the doping level of the OD0K sample is extracted from the rigid band shift measured by ARPES (see Chapter 3A.5). All samples were cleaved *in situ* in a cryogenic environment and inserted immediately into the STM. The data were acquired using different home-built cryogenic STMs among three groups.

Name	Doping	T_c (K)	Measurement T (K)	Data acquired by	Samples fabricated by	Vsetup (mV)/ Isetup (pA)/ Lock-in Amplitude (mV)	Effective Energy Resolution (FWHM, meV)
UD25K	0.101	25	5.7	Hudson group	Kondo group	-100/400/1	2.7
OP35K	0.160	35	5.7	Hudson group	Kondo group	-100/400/1	2.7
OD23K	0.224	23	4.2	Allan group	UvA group	-150/150/1.5	2.58
OD15K	0.243	15	6	Hoffman group	Kondo group	-100/100 / 2	3.5
OD12K	0.249	12	4.2	Allan group	UvA group	-200/170/1.5	2.58
OD9K	0.255	9	4.2 – 20	Allan group	UvA group	-150/200/1.5	2.58 – 6.42
OD7K	0.258	7	2.2	Allan group	UvA group	-20/600/1.5	2.50
OD3K	0.265	3	4.2	Allan group	UvA group	-200/170/1.5	2.58
OD0K	0.274		4.2	Allan group	UvA group	-25/200/1.5	2.58

Table 3A.1: Samples and their measurement conditions in this study.

3A.2 The Phenomenological Model to fit Spectra

3A.2.1 The d -wave Gap Model

The d -wave gap is here modeled as a mean of multiple s -wave gaps, one for each point along the Fermi Surface. For each s -wave gap, the gap size is given by $\Delta_{\mathbf{k}}$. The points are found using the Fermi Surface of the tight-binding model for the OD15K sample²⁷ although the final shape of the spectrum varies a lot with the exact points in k -space used. Each s -wave gap is generated by using the Dynes formula

$$Dynes(E, \Delta_{\mathbf{k}}, \Gamma) = \text{Re} \left(\frac{E + i\Gamma}{\sqrt{(E + i\Gamma)^2 - \Delta_{\mathbf{k}}^2}} \right) \quad (3.A1)$$

where the same Γ is used for all s -wave gaps. The resulting d -wave gap is the mean of all s -wave gaps. To account for the normal-state density of states (DOS), the d -wave gap function is multiplied with a polynomial function, typically of the 3rd order. The resulting spectrum is then convoluted with a Gaussian function with a full width at half maximum (FWHM) given in the table above, in order to emulate the effect of finite temperature and the lock-in modulation have on the shape of the measured spectrum.

The points in momentum space are calculated only once before the fitting process to reduce computation time. The fitting parameters characterizing the gap are only Δ and Γ . To calculate the filling for the d -wave gap we calculate the mean of the filling for each individual s -wave gap using Eq. 3.4.

3A.2.2 Statistical Analysis with and without the Excluded Spectra

In the main text we “white out” certain spectra (white areas in **Figs. 3.3b-d**), and exclude them for the statistical analysis when either of the two conditions is met in the fit results: 1) $\Gamma > 20$ meV; 2) $\Delta > 15$ meV. Our interpretation is that these spectra are fully filled, for the following reason: the spectra that meet the first criterion have so much broadening that there is no well-defined gap. Similarly, for the spectra that meet the second criterion, the large “gap” is a reflection of background modulations. Such spectra are thus counted as fully filled. Still, we show here that including these spectra in the analysis does not alter our main conclusions.

Fig. 3A.1 shows, from left to right, the spatial distributions of: Δ , including “whited-out” (1st column) and excluding “whited-out” (2nd column) spectra,

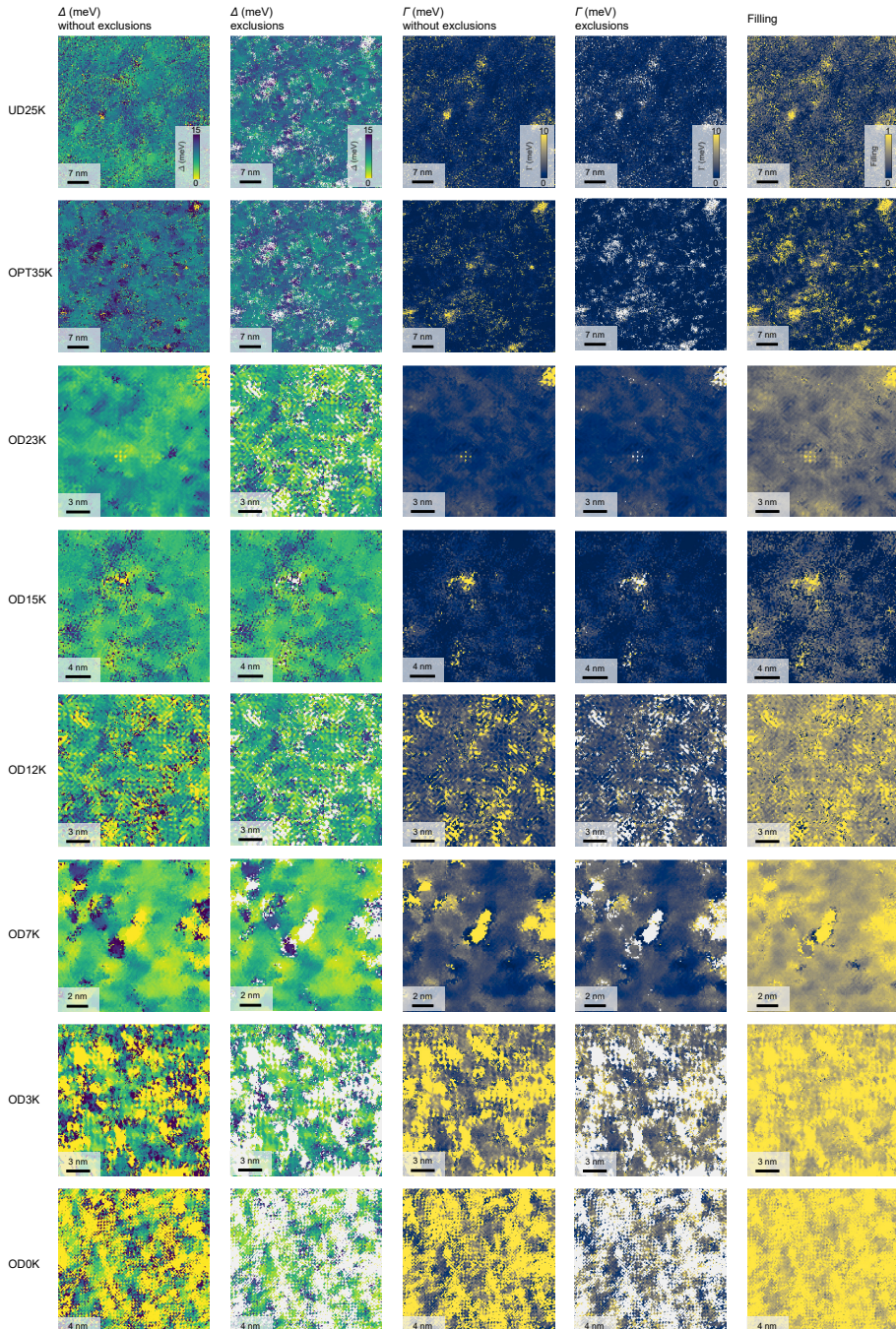


Figure 3A.1 Spatial variations of the gap size Δ with and without exclusions, parameter Γ with and without exclusions, and the calculated filling for all samples. See 3A.2 for details.

Γ , with (3rd column) and without (4th column) “whited-out” spectra, and F , the filling (5th column) for all samples. The images are ordered top to bottom, from lowest to highest doping, respectively. Following the argumentation in the preceding paragraph, the filling for “whited-out” spectra is set to 1, when they are included in the statistics. **Fig. 3A.2** shows the histograms for Δ including “whited-out” spectra, and the histograms of Γ , both with and without “whited-out” spectra. The remaining histograms of Δ excluding the “whited-

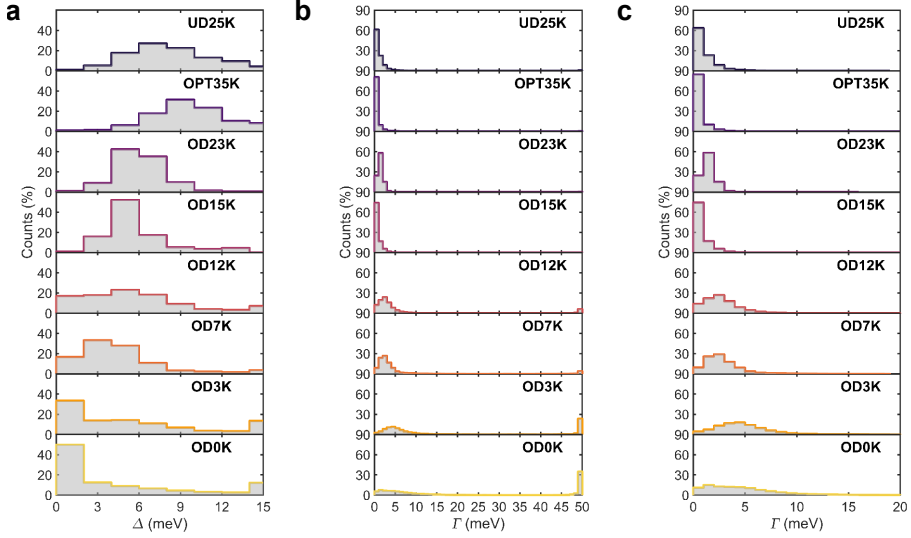


Figure 3A.2 Histograms of the gap size Δ without any spectra that are whited out (a). Histograms for Γ including (b) and excluding whited-out spectra (c). See 3A.2 for details.

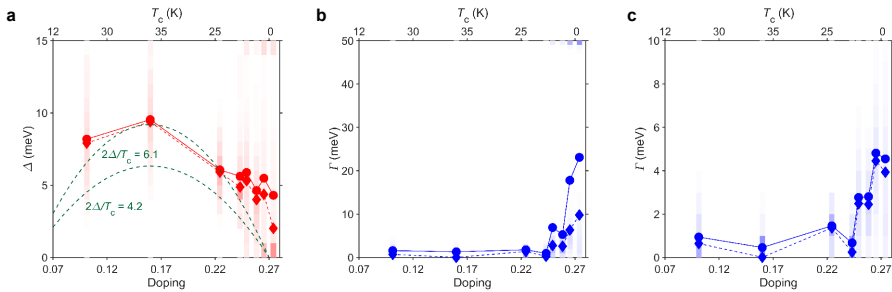


Figure 3A.3 The results for Δ without excluding any spectra, and for Γ including and excluding “whited-out” spectra are summarized (a, b, c respectively). The circles indicate the mean Δ , Γ for each sample, with the diamonds indicating the medians. The shaded areas in the background represent the spread in values these parameters have. The green dashed lines in the left figure indicate the behavior expected for Δ proportional to T_c . The value of $2\Delta/T_c$ corresponds to the dirty d -wave BCS limit, while $2\Delta/T_c$ is chosen such that it matches the OPT35K data point.

out" spectra and of the filling can be found in the main text. The histograms in **Fig. 3A.2** are summarized in **Fig. 3A.3** in a similar fashion to **Fig. 3.4**.

From the spatial distributions and histograms of Δ and Γ in **Figs. 3A.1-3**, we conclude that even when the "whited-out" spectra are considered: 1) the gap size still deviates from the behavior in the OD regime; 2) gapped spectra can still be found in the non-SC sample in significant quantities.

The spatial averages of the "whited-out" spectra and of the rest spectra are shown in **Fig. 3A.4** for each sample. We find that after whitening out all samples, even the non-SC sample, show a gap in their average spectrum. We note that the spatially-averaged "whited-out" spectra in the OD regime are fully filled, i.e. they no longer have a gap, and often show a peak near Fermi level. This further justifies our choice to assign all these spectra a filling of 1. For the UD25K and OPT35K samples, the "whited-out" spectra are made up of spectra for which the fit has failed due to limited signal-to-noise. Even though these spectra appear as gapped, we attribute this to the presence of a pseudogap. We find that the assignment of $F = 1$ to these spectra does not alter the main conclusion either, given the relatively small portions of "whited-out" spectra in these samples (see **Fig. 3A.4**). The increase of the area of "whited out spectra" in the OD as shown in **Fig. 3A.4** reaffirms the increased gap filling in these samples.

3A.2.3 Fit Parameters Fig. 3.2c'

In **Table 3A.2**, we present the values of Δ and Γ as determined by our model for the examples shown in **Fig. 3.2c** of the main text. Also indicated are the 95% confidence intervals for those values. All confidence intervals are below the effective energy resolution of the experiment (see **Table 3A.1**), with one

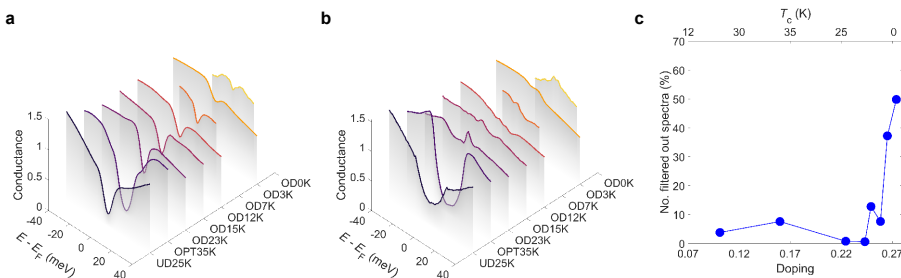


Figure 3A.4. **a)** The spatially-averaged spectra after the "whited-out" spectra have been removed. **b)** Spatial averages of the "whited-out" spectra for each doping level. **c)** The proportions of "whited-out" spectra that make up each sample as a function of doping.

exception. Spectrum number 1 of the OD12K sample does not show a gap, and therefore the values for Δ and Γ are ill-determined, as expressed by the confidence interval. This spectrum however also meets our conditions defined in Chapter 3A.2. As such, the poorly determined values for Δ and Γ are a clear indication that we in those cases we are dealing with spectra for which those parameters have no physical meaning.

3A.2.4 Energy Range for Fitting and Approximations for the Normal Density of States

The spectra in the UD and OPT samples show clear pseudogap (PG) features, with PG sizes ranging from 20 meV to over 60 meV (see **Fig. 3.1a**). Furthermore, in the OD regime, the normal-state DOS shows a peak near the Fermi level. These additional features next to the superconducting gap complicate the accurate fitting of the superconducting gap. We circumvent this complication by limiting our analysis to a small window E_{win} around the Fermi level. In this reduced energy window, the additional features are only partly visible, and can be sufficiently approximated by a polynomial DOS. The choices of E_{win} and the order of the polynomial background are arbitrary but necessary choices

Sample	Spectrum	Δ (meV)	Γ (meV)
OD23K	1	6.3 ± 1.3	1.6 ± 0.7
	2	5.4 ± 1.3	2.1 ± 0.9
	3	6.7 ± 0.8	1.1 ± 0.4
	4	6.3 ± 0.5	0.9 ± 0.3
	5	9.9 ± 1.9	2.0 ± 0.5
OD12K	1	$0.8 \pm 2E5^*$	$47 \pm 5E6^*$
	2	6.9 ± 2.0	3.0 ± 1.0
	3	3.4 ± 0.8	1.1 ± 0.8
	4	2.7 ± 0.7	0.9 ± 0.7
	5	4.2 ± 1.7	2.9 ± 1.6
OD3K	1	6.7 ± 1.7	3.1 ± 0.9
	2	4.7 ± 1.1	2.9 ± 0.9
	3	5.9 ± 1.4	3.2 ± 0.9
	4	4.9 ± 2.7	3.2 ± 2.1
	5	5.4 ± 1.4	2.6 ± 0.9

* Spectra that do not show a gap and therefore have ill-defined gap parameters.

Table 3A.2 Fitted values of Δ and Γ for the example spectra shown in fig 2c of the main text, together with the 95% confidence interval for those values. The spectra are numbered from bottom to top.

made before the fitting procedure. Here we show the influence the particular choices have on the superconducting gap size and filling in the OD samples.

In the main text, we use $E_{\text{win}} = \pm 15$ meV, which is a choice made before the fitting procedure. Altering this choice does not affect the main conclusions of our analysis, as shown in **Fig. 3A.5**. We repeat the analysis using different energy windows and find that the qualitative behavior does not change: Δ remains constant while F sharply increases in the SOD regime. Further increasing E_{win} beyond 20 meV, the highly inhomogeneous normal-state DOS becomes more significant, defeating the aim of focusing on the superconducting gap through an energy window. With an energy window smaller than 10 meV, we find that too little of a spectrum is left to characterize the superconducting gap accurately.

Another possible influential choice in the fitting procedure is the order of the background polynomial used to model the normal-state DOS. **Fig. 3A.6** shows the mean gap size and filling for the OD23K, OD12K, and OD3K samples for different orders of polynomial ranging from 1st to 4th order. The overall behavior of nearly constant gap size and increasing filling is present for all polynomial orders. We opt to use a 3rd order polynomial in the main text as it offers the best balance between underfitting and overfitting.

3A.2.5 An Alternative Model

Here we introduce an alternative approach to determining the gap filling, and show that the conclusions are the same using this model. We use a model which explicitly includes the filling F as a fitting parameter, in contrast to extracting F using fit parameters Δ and Γ in the main text:

$$g(E) = P(E) * [(1 - F) * \text{Dynes}(E, \Delta, \Gamma) + F] \quad (3.A2)$$

where $P(E)$ and $\text{Dynes}(\Delta, \Gamma)$ are defined the same as those in the main text. The gap filling is now explicitly parametrized by the parameter F , with $F = 0$ corresponding to fully gapped and $F = 1$ to fully filled. To prevent overfitting and to limit built-in correlations between fit parameters we fix the value of Γ . **Fig. 3A.8** shows the average gap size and gap filling from the fit results using this model, analogous to **Fig. 3.4** in the main text. For this alternative model, we exclude spectra with a) Δ close to 0 ($\Delta < 1$ meV), and b) F close to 1 ($F > 0.95$) from further analysis. In case a) the gap sizes become smaller than our thermally limited energy resolution, preventing an accurate determination of

Δ . In case b) F becomes ill-defined as F can be absorbed into when the gap is barely present. Fitting our data with this model, we find that the gap size remains constant in the OD regime, while the gap filling increases rapidly. Confirmation by an alternative model further strengthens the conclusions of the main text.

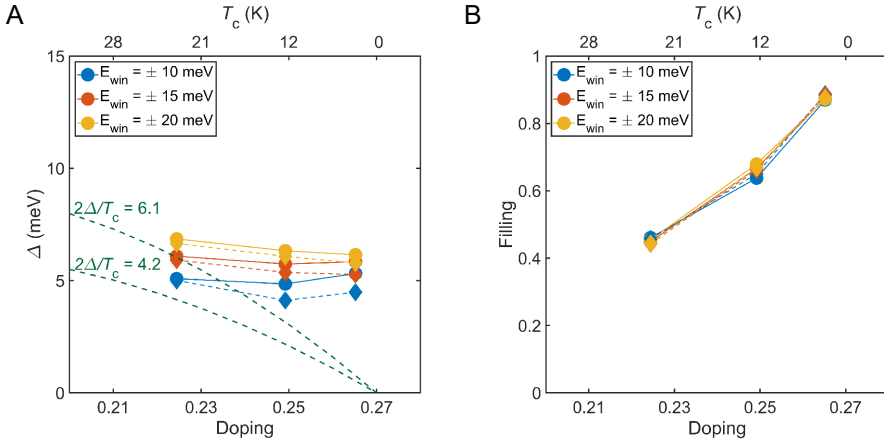


Figure 3A.5 Dependence of our conclusion on the choice of the energy window. The dependencies on the fitting energy window for the average Δ and filling (a, b respectively) for the overdoped samples OD23K, OD12K, and OD3K. While the absolute values of the averages vary slightly with the cutoff energy, the overall behavior of a constant gap size and increasing filling factor is independent of the cutoff.

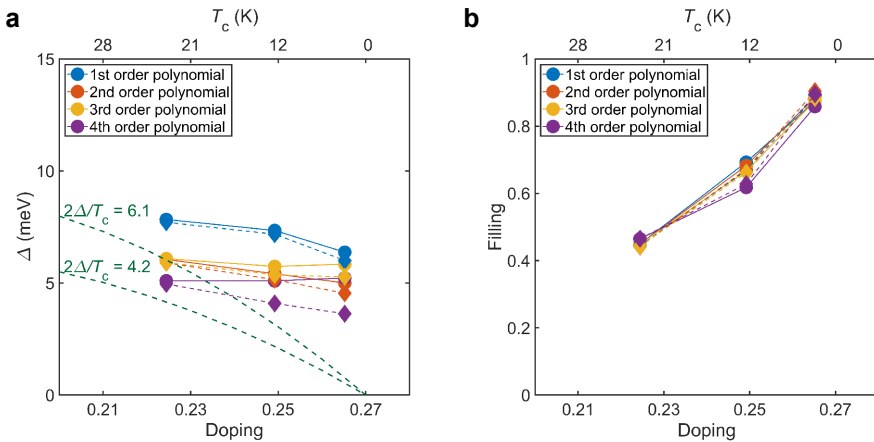


Figure 3A.6 Dependence of our conclusion on the choice of the polynomial normal-state DOS. The average gap size and filling (a, b) for the overdoped samples OD23K, OD12K, and OD3K as the order of the polynomial normal-state DOS is varied. While the absolute values of the averages vary a bit among the various polynomials, the overall qualitative behavior of a barely varying gap size and the drastic increasing filling is present in all cases.

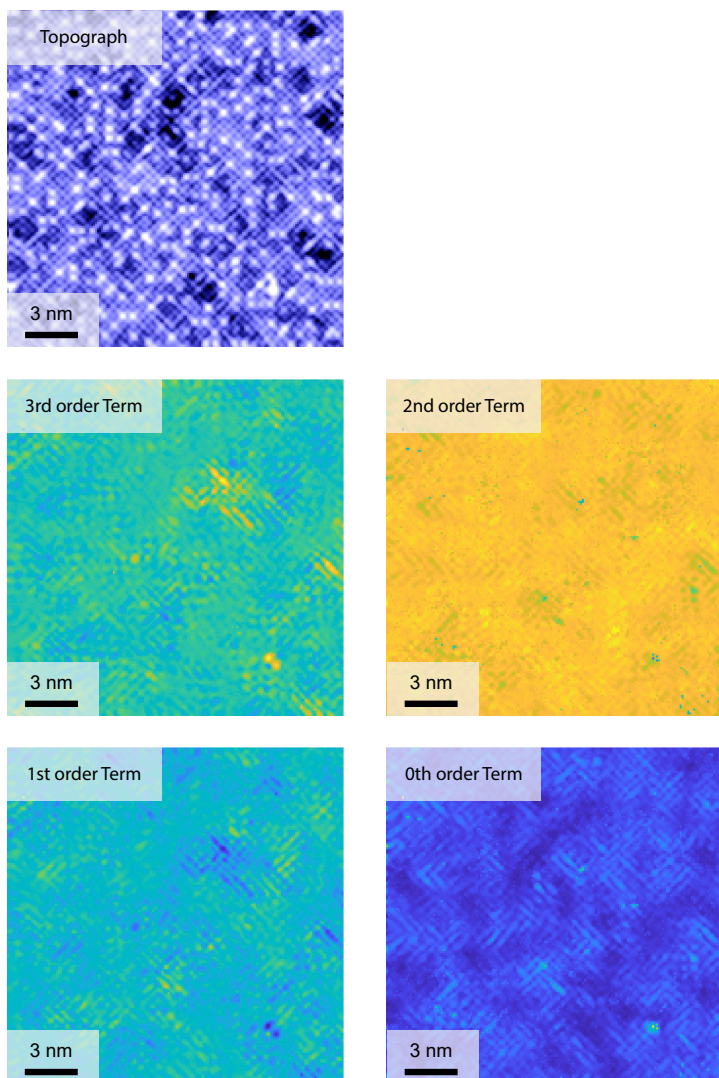


Figure 3A.7 Topography of the OD12K, together with the spatial distributions of the polynomial background terms used in the fits in the main text. The correlation coefficients of the 3rd, 2nd, and 1st order terms with the topography are 0.08, -0.11, and -0.13 respectively, meaning they do not correlate with the topography. The 0th order term (i.e. the constant term) does correlate with the topography (coefficient of 0.37). The underlying relation of this is that they both relate to the same quantity, the average LDOS of that spectrum. If this is low the constant background term will go down. A low average DOS also means there are less states to tunnel into with our STM tip, meaning that the tip will move closer to the sample to maintain the same setup current. Hence, this location will register as a suppression of the surface. This is clearly visible when comparing the topography with the spatial distribution of the constant background term. Darker regions of the topography are also visible as darker regions of the constant term.

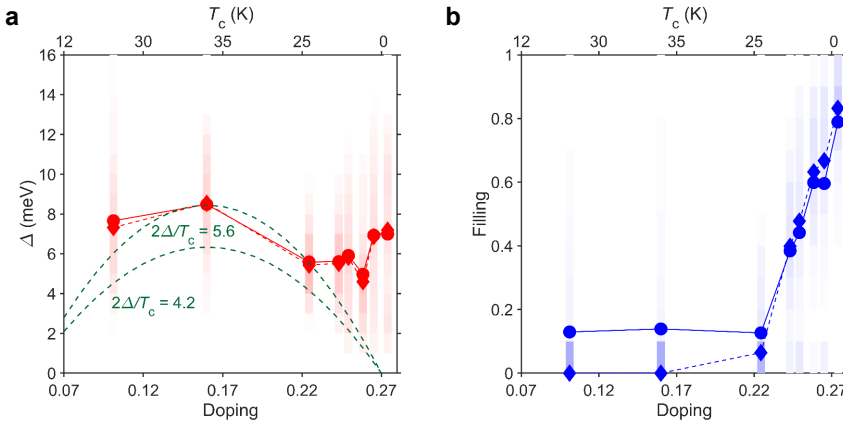


Figure 3A.8 Gap magnitude and filling versus doping using the alternative model. The gap size (a) and the gap filling (b) as determined by the application of the alternative model described above. The shaded areas indicate the histograms of the parameters at each doping level. The average gap sizes and average filling are indicated by the circles. The median (diamonds) is shown to better reflect highly asymmetric distributions as is the case for the gap filling. The robustness of the qualitative trends against the use of different models reinforces the main conclusions.

3A.3 Temperature Dependence

In Fig. 3A.9a, we show the temperature evolution of the average spectrum measured in the same field of view on the OD9K sample. Furthermore, we show the median values for the gap and filling parameters as a function of temperature in the same field of view in Figs. 3A.9b,c respectively. We find that a gap is still present up to 20K for the OD9K sample, even when the temperature-limited and lock-in broadened energy resolution is taken into account. With increasing temperature, we see that the gap magnitude and gap filling remain fairly constant up to 20K.

3A.4 Intrinsic Metal-Induced Pair-Breaking Effects Within a Superconducting Puddle Embedded in a Metallic Matrix

In this section, we consider the case of a small d -wave superconducting puddle whose size is of the order of the superconducting coherence length ξ_{0r} , embedded in a metallic matrix. This is a particularly relevant model for the strongly overdoped regime. Our treatment of this system is entirely mean-field; we employ large-scale numerical simulations of the Bogoliubov-de Gennes Hamiltonian to uncover interesting aspects of this system. To our knowledge,

such calculations have not previously been performed in the literature; similar calculations (but for a superconducting puddle in a superconducting matrix) have been reported by Fang *et al.*⁴⁰ and Nunner *et al.*⁴⁷.

We show here that one striking effect of the surrounding metallic matrix is to significantly *weaken* *d*-wave superconductivity, such that the resulting *d*-wave order parameter within the puddle is less than that of a bulk homogeneous system with the same pairing interaction. Decreasing the size of the puddle has the effect of decreasing the average *d*-wave order parameter within the puddle. We additionally find a concurrent increase in the average local density of states

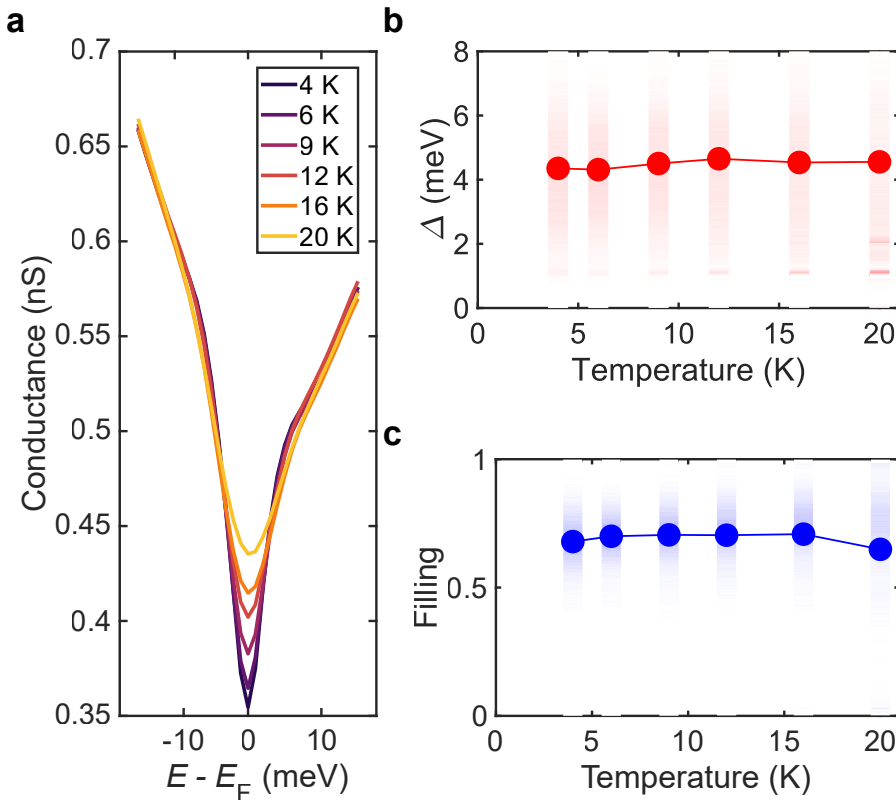


Figure 3A.9 Temperature evolution of the gap width and gap filling. **a)** Average spectra measured in the same field of view on the OD9K sample ($V = -150$ mV, $I = -200$ pA). **b)** Median values for the gap magnitude in the same field of view of **a**, as a function of temperature. The shaded areas indicate the histograms of the gap at each temperature. **c)** Median values for the Filling parameter in the same field of view of **a**, as a function of temperature. The shaded areas indicate the histograms of the Filling at each temperature.

(LDOS) at zero energy within the puddle when the puddle size is decreased. The behavior of the puddle as its size is decreased is vastly reminiscent of the effect of increasing disorder on bulk d -wave superconductivity, and originates entirely from the mixing of the superconducting states within the puddle with the metallic states of the surrounding matrix. Thus, the surrounding metal induces pair-breaking within the puddle, very similar to the effect of disorder⁴⁸⁻⁵⁰. Importantly, our calculations confirm that the negative correlation between gap size and filling expected in the mean-field theory also holds for the heterogeneous case (see **Fig. 3.4d**).

In our simulations, we assume that the d -wave superconducting puddles are square patches of size $l \times l$. We self-consistently calculate the order parameter from:

$$\Delta_{\mathbf{r}\mathbf{r}'} = V_{\mathbf{r}\mathbf{r}'} \langle c_{\mathbf{r}\uparrow} c_{\mathbf{r}'\downarrow} \rangle \quad (3.7)$$

The pairing interaction $V_{\mathbf{r}\mathbf{r}'}$ is nonzero only for nearest-neighbor bonds attached to sites within the $l \times l$ patch, and otherwise vanishes. To compute $\Delta_{\mathbf{r}\mathbf{r}'}$ and the LDOS $g(\mathbf{r}, \omega)$, we employ an exact real-space Green's function method particularly suited for very large inhomogeneous systems^{51,52}. For the calculations reported here, the system size is 100×200 , which is larger compared to what more traditional exact-diagonalization methods can access. We iterate the calculation until the order parameter is converged, and we assume that we are at $T = 0$. We take the normal-state dispersion (up to next-nearest-neighbor hopping) to be given by the following parameters: $t_1 = 1$, $t_2 = -0.33$, and $\mu = -1.22$ (from this point on we express all energies in units where $t_1 = 1$). The spatially resolved site-centered d -wave order parameter plotted throughout this section is obtained by adding the order parameter on all four bonds connected to a single site but assuming a sign difference between the order parameter on bonds along the x -direction and that on bonds along the y -direction.

We are interested in determining whether d -wave superconductivity in puddles behaves differently compared to the bulk case due to the abundance of low-energy states in the nearby metal, and we will tune the size of the puddles (from 5×5 to 17×17) in particular to isolate the effect of the nearby metal. One expects that the smaller the puddle, the stronger the effect of the metal, since a larger fraction of the puddle is in close proximity to the metal-superconductor boundary. We take the nearest-neighbor pairing interaction

strength to be $V_0 = 1.0$ inside the superconducting puddle and $V_0 = 0$ outside it. To provide a baseline for comparisons, we perform the same calculation for a bulk d -wave superconductor as well, with the same nearest-neighbor pairing interaction $V_0 = 1.0$ present throughout the entire system. We will frequently express the puddle size in terms of l/ξ_0 , where ξ_0 is the coherence length of the superconducting condensate within the puddle; this is to make clearer the effects of miniaturizing the superconducting puddle to dimensions of the order of ξ_0 itself. Note that we have suppressed here the explicit l -dependence of ξ_0 , since as it turns out the magnitude of the superconducting order parameter within the puddle, and consequently ξ_0 itself, depends sensitively on l .

Our results are collected together in **Fig. 3A.10**. In **Fig. 3A.10a**, we compare the spectral gap (here rather roughly defined as half the peak-to-peak distance in energy, measured from the LDOS) to the d -wave order parameter, with both quantities averaged within the puddle. It can be seen that the spectral gap tracks the d -wave order parameter closely for the bulk system and for larger puddles (7×7 up to 17×17 , all corresponding to $2 < l/\xi_0 < 10$), although for puddles the spectral gap slightly *overestimates* the d -wave order parameter. However, once the puddle size is small enough such that $l/\xi_0 \approx 1$ (as is the case for the 5×5 puddle), a gap is no longer visible in the spectrum, even though a nonzero superconducting order parameter remains within the puddle. The strong pair-breaking effects of the surrounding metal are most easily seen in **Fig. 3A.10b**. Here we plot the average d -wave order parameter within the puddle as a function of l/ξ_0 . The average order parameter within all seven puddles considered is considerably less than that of the bulk system, and decreases in magnitude as l/ξ_0 is made smaller. Note that when the puddle is made smaller and smaller, the mixing of metallic states into the superconducting puddle increases since more of the puddle becomes in closer proximity with the superconductor-metal boundary, and hence there is more pair-breaking. **Fig. 3A.10c** shows the average zero-energy LDOS for seven different puddle sizes. Notice that the zero-energy LDOS of all puddles is much bigger than that of the bulk system, and that it increases as the puddle size is decreased. As with the d -wave order parameter, the large zero-energy LDOS is an effect of the mixing of the metallic states into the superconducting puddle, giving the latter a much larger number of low-energy states than one would expect a bulk d -wave superconductor to have. The overall trend is succinctly captured by **Fig. 3A.10d**, which plots together with the d -wave order parameter and the zero-energy LDOS both averaged within the puddle, with the variations in both quantities due solely to the puddle size. It can be seen that these two

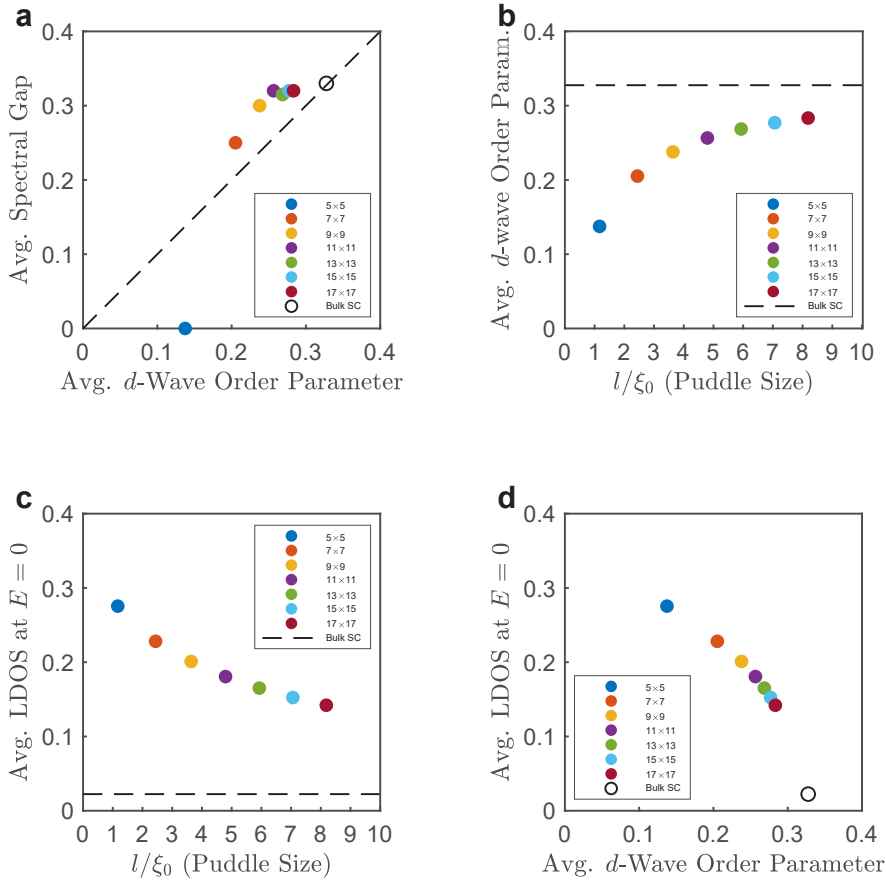


Figure 3A.10 Results for clean superconducting puddles within a metallic matrix of varying size, with $V_0 = 1.0$. **a)** plot of the average spectral gap versus the average d -wave order parameter, both averaged within the superconducting puddle, with the dashed line indicating where the two quantities are equal. It can be seen that for puddles, the spectral gap is a good indicator of the d -wave order parameter (although overestimating it, lying above the dashed line) right until the puddle becomes sufficiently small and $l/\xi_0 \approx 1$ (e.g., 5×5), at which point no gap can be seen even though a nonzero superconducting order parameter is present. **b)** plot of the average of the d -wave order parameter within the superconducting puddle versus the puddle size l/ξ_0 , with the value for the bulk system shown as a dashed line. **c)** plot of the zero-energy LDOS averaged within the superconducting puddle versus the puddle size l/ξ_0 , again with the value for the bulk system shown as a dashed line. **d)** plot of the LDOS at $E = 0$ versus the d -wave order parameter, both averaged inside the superconducting puddle. Evidently, the effect of reducing the puddle size on the superconducting condensate within the puddle is the same as that of increasing the amount of disorder: the d -wave order parameter becomes smaller, while the zero-energy LDOS increases.

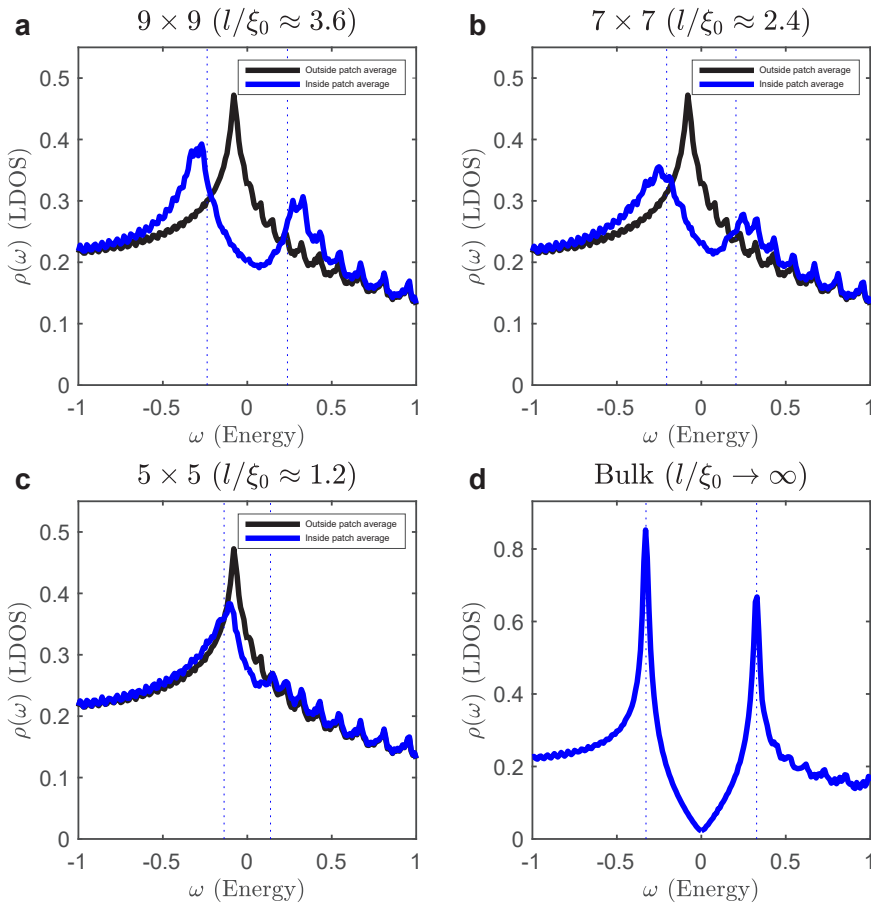


Figure 3A.11 Plots of the LDOS as a function of energy for a d -wave superconducting puddle inside a metallic matrix with decreasing puddle size, with $V_0 = 1.0$. The puddle sizes are 9×9 , 7×7 , and 5×5 (a-c), corresponding to l/ξ_0 approximately equal to 3.6, 2.4, and 1.2, respectively. Shown are LDOS averages within the puddle (blue) and outside it (black). Also shown for comparison is the average LDOS for a bulk d -wave superconductor with the same pairing interaction $V_0 = 1.0$ (d). The dashed blue lines indicate the average d -wave order parameter within the superconducting puddle. Note that as the puddle size becomes smaller, the zero-energy LDOS inside the patch becomes larger, the coherence peaks become smeared out and move to lower energies, and the gap becomes less discernible.

quantities are inversely proportional to each other, with a large d -wave order parameter corresponding to a small zero-energy LDOS and vice versa. This is behavior very similar to that expected from disorder acting on a bulk d -wave superconductor; one cannot escape the conclusion that the metallic matrix induces pair-breaking effects within the superconducting puddle very similar to that of disorder.

All of these findings are more explicitly demonstrated in **Fig. 3A.11**, wherein we show plots of the LDOS vs. energy for three puddle sizes (5×5 , 7×7 , and 9×9 , whose l/ξ_0 values are given approximately by 1.2, 2.4, and 3.6, respectively), in addition to the bulk d -wave case. We note first that for superconducting puddles, a striking feature of the LDOS is its very large value at $E = 0$ compared to that of the bulk system. One can also notice that for larger puddles, a gap is easily discerned in the spectrum, and coherence peaks are visible but are broader, less well-defined, and shorter in height compared to those of a bulk system. These features become progressively broader as the puddle is shrunk, and more spectral weight accumulates near the Fermi energy, a result of the fact that the average d -wave order parameter becomes smaller the tinier the puddles get. However, when the puddle is made sufficiently small such that $l/\xi_0 \approx 1$, such as the 5×5 case here, the gap ceases to be visible in the quasiparticle spectrum, and the LDOS resembles that of a normal metal. Nevertheless, there is still a nonzero d -wave order parameter present within the puddle.

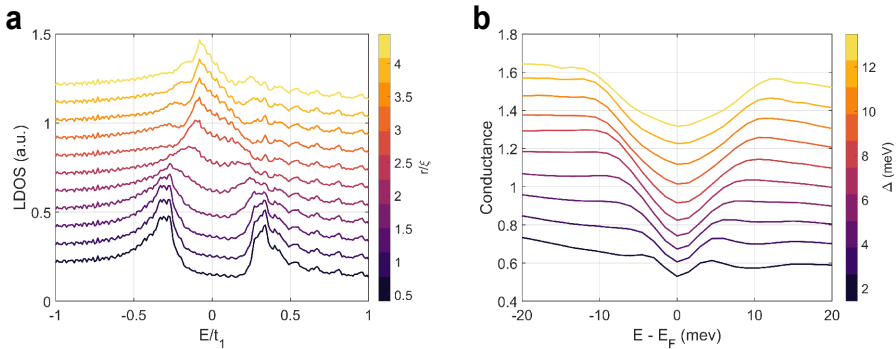


Figure 3A.12. *a)* Waterfall plot of the spectra calculated for the 9×9 puddle (the same data as presented in **Fig. 3.1f**), showing a clear correlation between the gap size going to zero and the coherence peaks disappearing. *b)* Spectra of the OD12K sample binned and averaged according to their gap size Δ , as determined by our model. The visibility of the coherence peaks here has no clear relation to the size of the gap. The spectra in **a,b**) have been shifted with respect to each other for clarity.

In sum, we have shown here some of the surprising effects of embedding a d -wave superconducting puddle within a metallic matrix. We have demonstrated that the surrounding metallic matrix has a pair-breaking effect on the superconductivity within the puddle, akin to that of disorder, that fills the gap, including at the Fermi level. We have also shown that the smallness of the puddle has a nontrivial effect on the LDOS, with the quasiparticle spectrum within the puddle showing broad signatures of a gap that progressively becomes filled up and washed out the smaller the puddle becomes. The similarity of the pair-breaking effects of the metallic matrix to disorder points to the difficulty of attributing the effects seen in the experiment and detailed in the main text to purely mean-field effects.

Our calculations show that within a mean-field picture, pair-breaking, whether it be due to disorder or the effect of metallic states on a superconducting puddle, naturally leads to an *anticorrelation* between these two quantities. Such a scenario points to the necessity of “beyond-mean-field” physics in resolving the conundrum posed by the experimental results discussed in the main text.

3A.5 Rigid Band Shift in Overdoped Bi2201

The doping levels of the superconducting samples are determined using the Presland formula, while the doping level of the OD0K sample is extracted from the rigid band shift measured by ARPES. Below, we describe this procedure more detail.

ARPES measurements on SOD samples show a rigid band shift of the anti-nodal band bottom when the doping is increased (**Fig. 3A.13**). ARPES measurements were performed using the He1 α line at 21.2 eV with linear polarization. The sample temperature for all samples was 50K, and the total experimental resolution was set to 6 meV. The k-space cut was along the face of the Brillouin zone (a line spanning the direction (π, π) - $(\pi, 0)$ - $(\pi, -\pi)$), indicated in the inset of **Fig. 3A.13a**).

Shown in **Fig. 3A.13a** as “+” symbols are the positions of the peak maxima of the Energy Distribution Curves (EDC’s), extracted after dividing out the resolution broadened Fermi-Dirac distribution from the raw data. The energy position of the band bottom as shown in **Fig. 3A.13b** is extracted by taking the average of the EDC maxima positions within a small momentum window (indicated in **Fig 3A.13a** by the two vertical red lines). Using these doping-

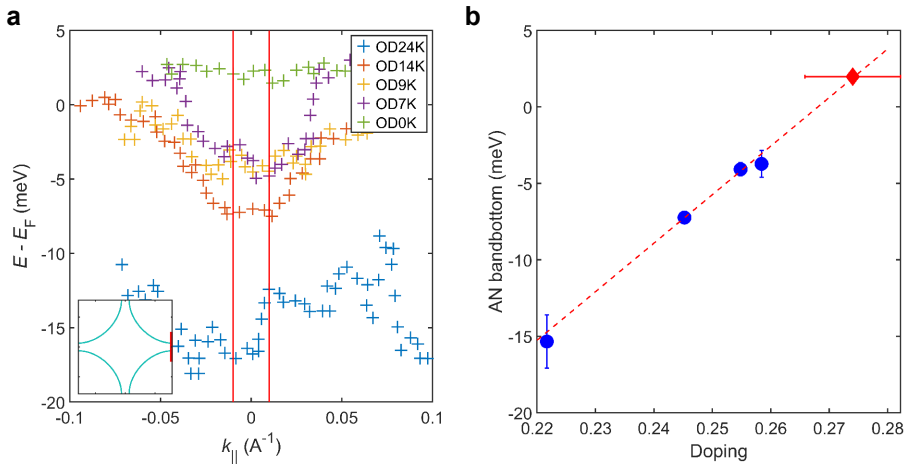


Figure 3A.13 Rigid band shift of the anti-nodal band bottom. The anti-nodal ARPES cut is indicated by the red line on the Fermi surface in the inset to panel (a). In (a) can be seen that the anti-nodal band bottom shifts towards the Fermi level as the samples are progressively overdoped. The energy position of the band bottom is shown in panel (b), and is given by the average position within the red vertical lines in panel (a). The red dashed line in (b) shows a fit through the band bottom energy position for the superconducting samples (blue circles). The fit is then extrapolated to determine the doping level of the non-superconducting sample (red diamond), given its measured band bottom.

dependent band bottom energy values, we can determine the doping level of the OD0K crystal by fitting the positions of the superconducting samples and extrapolating the result. We find that the OD0K sample has a doping level of $p=0.274\pm 0.008$.

3A.6 Gap Filling and DOS from other Experiments

Fig. 3A.14 shows the comparison of the gap filling we observe and several other experiments determining the DOS at the Fermi level: optical conductivity¹⁴ (**Fig 3A.14a**), Specific heat measurements^{53,54} (**Fig 3A.14b**), and Knight shift⁵⁵ (**Fig. 3A.14c**). All these probes measure a DOS at Fermi level increasing with overdoping, concomitant with the increased gap filling we observe. We posit that this increased DOS is due to increasingly more Cooper pairs broken by a non-mean field process (see Chapter 3.2.3).

3A.7 Pair Breaking, Gap Filling and Competing Orders.

In the overdoped cuprates several (fluctuating) orders other than superconductivity have been observed, being two distinct types of charge order^{56,57}

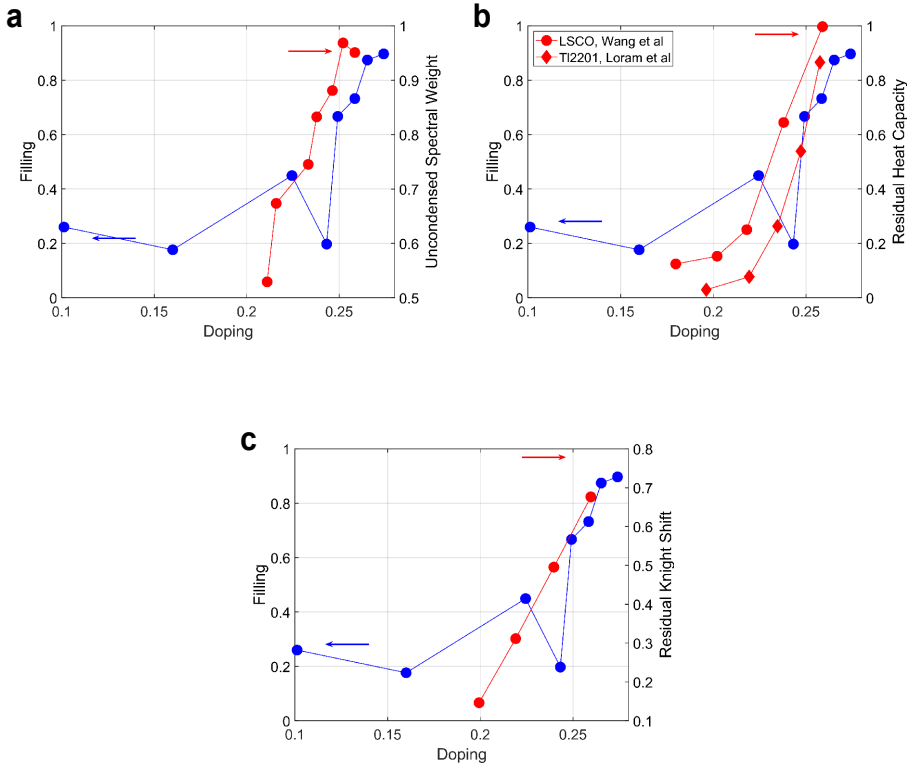


Fig 3A.14 Filling vs spectral weight from optical conductivity below T_c^{14} (a), Filling vs residual specific heat^{52,53} (b), and Filling vs residual Knight shift below T_c^{55} (c).

and fluctuating ferromagnetism^{58,59}. Here we address their possible relation with our findings.

The charge order of the UD regime continues past optimal doping in the overdoped regime, weakening as the doping increases. This doping dependence is opposite to the behavior of the gap filling, making this an unlikely candidate to participate in the gap filling. The second type of order, $\sqrt{2}$ order observed by STM. Research on this phenomenon is ongoing – as mentioned, the relationship to RIXS data is not clear. This CDW is only visible in certain areas, and thus we deduce that it is not directly connected to the phenomenology reported here. In any case, the main points of our paper – puddle formation, persistent gap, non-mean-field breakdown – remain independent on what exactly this CDW is.

References

- [1] Keimer, B., Kivelson, S. A., Norman, M. R., Uchida, S. & Zaanen, J. From quantum matter to high-temperature superconductivity in copper oxides. *Nature* **518**, 179–186 (2015).
- [2] Bozovic, I., He, X., Wu, J. & Bollinger, A. T. Dependence of the critical temperature in overdoped copper oxides on superfluid density. *Nature* **536**, 309–311 (2016).
- [3] Uemura, Y. J. *et al.* Magnetic-field penetration depth in $\text{Tl}_2\text{Ba}_2\text{CuO}_{6+\delta}$ in the overdoped regime. *Nature* **364**, 605–607 (1993).
- [4] Lemberger, T. R., Hetel, I., Tsukada, A., Naito, M. & Randeria, M. Superconductor-to-metal quantum phase transition in overdoped $\text{La}_{2-x}\text{Sr}_x\text{CuO}_4$. *Phys. Rev. B* **83**, 140507 (2011).
- [5] Lee-Hone, N. R., Dodge, J. S. & Broun, D. M. Disorder and superfluid density in overdoped cuprate superconductors. *Phys. Rev. B* **96**, 024501 (2017).
- [6] Li, Z.-X., Kivelson, S. A. & Lee, D.-H. The superconductor to metal transition in overdoped cuprates. *npj Quantum Mater.* **6**:36 (2021).
- [7] Lee-Hone, N. R., Özdemir, H. U., Mishra, V., Broun, D. M. & Hirschfeld, P. J. Low energy phenomenology of the overdoped cuprates: Viability of the Landau-BCS paradigm. *Phys. Rev. Res.* **2**, 013228 (2020).
- [8] Vignolle, B. *et al.* Quantum oscillations in an overdoped high- T_c superconductor. *Nature* **455**, 952–955 (2008).
- [9] Fujita, K. *et al.* Simultaneous transitions in cuprate momentum-space topology and electronic symmetry breaking. *Science* **344**, 612–616 (2014).
- [10] Chen, S.-D. *et al.* Incoherent strange metal sharply bounded by a critical doping in $\text{Bi}2212$. *Science* **366**, 1099–1102 (2019).
- [11] He, Y. *et al.* Rapid change of superconductivity and electron-phonon coupling through critical doping in Bi-2212 . *Science* **362**, 62–65 (2018).
- [12] Valla, T., Drozdov, I. K. & Gu, G. D. Disappearance of superconductivity due to vanishing coupling in the overdoped $\text{Bi}_2\text{Sr}_2\text{CaCu}_2\text{O}_{8+\delta}$. *Nat. Commun.* **11**:569 (2020).
- [13] Ayres, J. *et al.* Incoherent transport across the strange metal regime of highly overdoped cuprates. *Nature* **595**, 661–666 (2021).
- [14] Mahmood, F., He, X., Bozovic, I. & Armitage, N. P. Locating the Missing Superconducting Electrons in the Overdoped Cuprates $\text{La}_{2-x}\text{Sr}_x\text{CuO}_4$. *Phys. Rev. Lett.* **122**, 027003 (2019).
- [15] Zaanen, J. Superconducting electrons go missing. *Nature* **536**, 282–283 (2016).
- [16] Maier, T. A., Karakuzu, S. & Scalapino, D. J. The overdoped end of the cuprate phase diagram. *Phys. Rev. Res.* **2**, 033132 (2020).

- [17] Bouadim, K., Loh, Y. L., Randeria, M. & Trivedi, N. Single- and two-particle energy gaps across the disorder-driven superconductor-insulator transition. *Nat. Phys.* **7**, 884–889 (2011).
- [18] Trivedi, N., Loh, Y. L., Bouadim, K. & Randeria, M. Emergent granularity and pseudogap near the superconductor-insulator transition. *J. Phys. Conf. Ser.* **376**, 012001 (2012).
- [19] Spivak, B., Oreto, P. & Kivelson, S. A. Theory of quantum metal to superconductor transitions in highly conducting systems. *Phys. Rev. B* **77**, 214523 (2008).
- [20] Spivak, B., Oreto, P. & Kivelson, S. A. d-Wave to s-wave to normal metal transitions in disordered superconductors. *Phys. B Condens. Matter* **404**, 462–465 (2009).
- [21] Dodaro, J. F. & Kivelson, S. A. Generalization of Anderson’s theorem for disordered superconductors. *Phys. Rev. B* **98**, 174503 (2018).
- [22] Ghosal, A., Randeria, M. & Trivedi, N. Inhomogeneous pairing in highly disordered s-wave superconductors. *Phys. Rev. B* **65**, 014501 (2001).
- [23] Ghosal, A., Randeria, M. & Trivedi, N. Role of Spatial Amplitude Fluctuations in Highly Disordered s-Wave Superconductors. *Phys. Rev. Lett.* **81**, 3940 (1998).
- [24] Putzke, C. *et al.* Reduced Hall carrier density in the overdoped strange metal regime of cuprate superconductors. *Nat. Phys.* **17**, 826–831 (2021).
- [25] Piriou, A., Jenkins, N., Berthod, C., Maggio-Aprile, I. & Fischer, Ø. First direct observation of the Van Hove singularity in the tunnelling spectra of cuprates. *Nat. Commun.* **2**:221 (2011).
- [26] Li, X. *et al.* Quasiparticle interference and charge order in a heavily overdoped non-superconducting cuprate. *New J. Phys.* **20**, 063041 (2018).
- [27] He, Y. *et al.* Fermi Surface and Pseudogap Evolution in a Cuprate Superconductor. *Science* **344**, 612–616 (2014).
- [28] Fei, Y. *et al.* Electronic effect of doped oxygen atoms in Bi2201 superconductors determined by scanning tunneling microscopy. *Sci. China Physics, Mech. Astron.* **61**, 127404 (2018).
- [29] Allredge, J. W. *et al.* Evolution of the electronic excitation spectrum with strongly diminishing hole density in superconducting $\text{Bi}_2\text{Sr}_2\text{CaCu}_2\text{O}_{8+\delta}$. *Nat. Phys.* **4**, 319–326 (2008).
- [30] Dynes, R. C., Narayanamurti, V. & Garno, J. P. Direct measurement of quasiparticle-lifetime broadening in a strong-coupled superconductor. *Phys. Rev. Lett.* **41**, 1509 (1978).
- [31] Herman, F. & Hlubina, R. Microscopic interpretation of the Dynes formula for the tunneling density of states. *Phys. Rev. B* **94**, 144508 (2016).
- [32] Herman, F. & Hlubina, R. Consistent two-lifetime model for spectral functions of superconductors. *Phys. Rev. B* **95**, 094514 (2017).
- [33] Li, Y. *et al.* Strongly-overdoped $\text{La}_{2-x}\text{Sr}_x\text{CuO}_4$: Evidence for Josephson-coupled grains of strongly-correlated superconductor. arXiv:2205.01702 (2022).

- [34] Ding, Y. *et al.* Disappearance of Superconductivity and a Concomitant Lifshitz Transition in Heavily Overdoped $\text{Bi}_2\text{Sr}_2\text{CuO}_6$ Superconductor Revealed by Angle-Resolved Photoemission Spectroscopy. *Chinese Phys. Lett.* **36** 017402 (2019).
- [35] He, Y. *et al.* Superconducting Fluctuations in Overdoped $\text{Bi}_2\text{Sr}_2\text{CaCu}_2\text{O}_{8+\delta}$. *Phys. Rev. X* **11**, 031608 (2021). Top of FormBottom of Form
- [36] Franz, M. & Millis, A. Phase fluctuations and spectral properties of underdoped cuprates. *Phys. Rev. B* **58**, 14572 (1998).
- [37] Berg, E. & Altman, E. Evolution of the fermi surface of d-wave superconductors in the presence of thermal phase fluctuations. *Phys. Rev. Lett.* **99**, 247001 (2007).
- [38] Kondo, T. *et al.* Disentangling Cooper-pair formation above the transition temperature from the pseudogap state in the cuprates. *Nat. Phys.* **7**, 21–25 (2011).
- [39] Howald, C., Fournier, P. & Kapitulnik, A. Inherent inhomogeneities in tunneling spectra of $\text{Bi}_2\text{Sr}_2\text{CaCu}_2\text{O}_{8-x}$. *Phys. Rev. B* **64**, 100504 (2001).
- [40] Fang, A. C. *et al.* Gap-Inhomogeneity-Induced Electronic States in Superconducting $\text{Bi}_2\text{Sr}_2\text{CaCu}_2\text{O}_{8+\delta}$. *Phys. Rev. Lett.* **96**, 017007 (2006).
- [41] Pasupathy, A. N. *et al.* Electronic Origin of the Inhomogeneous Pairing Interaction in the High- T_c Superconductor $\text{Bi}_2\text{Sr}_2\text{CaCu}_2\text{O}_{8+\delta}$. *Science* **320**, 196–201 (2008).
- [42] Parker, C. V. *et al.* Nanoscale proximity effect in the high-temperature superconductor $\text{Bi}_2\text{Sr}_2\text{CaCu}_2\text{O}_{8+\delta}$ using a scanning tunneling microscope. *Phys. Rev. Lett.* **104**, 117001 (2010).
- [43] Sacépé, B., Feigel'man, M. & Klapwijk, T. M. Quantum breakdown of superconductivity in low-dimensional materials. *Nat. Phys.* **16**, 734–746 (2020).
- [44] Bastiaans, K. M. *et al.* Direct evidence for Cooper pairing without a spectral gap in a disordered superconductor above T_c . *Science* **374**, 608–611 (2021).
- [45] Bozovic, I. & Levy, J. Pre-formed Cooper pairs in copper oxides and LaAlO_3 — SrTiO_3 heterostructures. *Nat. Phys.* **16**, 712–717 (2020).
- [46] Gomes, K. K., Pasupathy, A. N., Pushp, A., Ono, S., Ando, Y. & Yazdani, A. Visualizing pair formation on the atomic scale in the high- T_c superconductor $\text{Bi}_2\text{Sr}_2\text{CaCu}_2\text{O}_{8+\delta}$. *Nature* **447**, 569–572 (2007).
- [47] Nunner, T. S., Andersen, B. M., Melikyan, A. & Hirschfeld, P. J. Dopant-modulated pair interaction in cuprate superconductors. *Phys. Rev. Lett.* **95**, 177003 (2005).
- [48] Franz, M., Kallin, C., Berlinsky, A. J. & Salkola, M. I. Critical temperature and superfluid density suppression in disordered high- T_c cuprate superconductors. *Phys. Rev. B* **56**, 7882 (1997).
- [49] Lee, P. A. Localized states in a d-wave superconductor. *Phys. Rev. Lett.* **71**, 1887 (1993).
- [50] Durst, A. C. & Lee, P. A. Impurity-induced quasiparticle transport and universal-limit Wiedemann-Franz violation in d-wave superconductors. *Phys. Rev. B*

- 62, 1270 (2000).
- [51] Sulangi, M. A., Allan, M. P. & Zaanen, J. Revisiting quasiparticle scattering interference in high-temperature superconductors: The problem of narrow peaks. *Phys. Rev. B* **96**, 134507 (2017).
- [52] Sulangi, M. A. & Zaanen, J. Quasiparticle density of states, localization, and distributed disorder in the cuprate superconductors. *Phys. Rev. B* **97**, 144512 (2018).
- [53] Wang, Y. *et al.* Weak-coupling d -wave BCS superconductivity and unpaired electrons in overdoped $\text{La}_{2-x}\text{Sr}_x\text{CuO}_4$ single crystals. *Phys. Rev. B* **76**, 064512 (2007).
- [54] Loram, J. W., Mirza, K. A., Wade, J. M., Cooper, J. R. & Liang, W. Y. The electronic specific heat of cuprate superconductors. *Physica C* **235–240**, 134–137 (1994).
- [55] Ohsugi, S., Kitaoka, Y. & Asayama, K. Temperature dependence of Spin Susceptibility of $\text{La}_{2-x}\text{Sr}_x\text{CuO}_4$. *Physica C* **282–287**, 1373–1374 (1993).
- [56] Peng, Y. Y. *et al.* Re-entrant charge order in overdoped $(\text{Bi,Pb})_{2.12}\text{Sr}_{1.88}\text{CuO}_{6+\delta}$ outside the pseudogap regime. *Nat. Mater.* **17**, 697–702 (2018).
- [57] Li, X. *et al.* Evolution of Charge and Pair Density Modulations in Overdoped $\text{Bi}_2\text{Sr}_2\text{CuO}_{6+\delta}$. *Phys. Rev. X* **11**, 11007 (2021).
- [58] Kopp, A., Ghosal, A. & Chakravarty, S. Competing ferromagnetism in high-temperature copper oxide superconductors. *Proc. Natl. Acad. Sci.* **104**, 6123–6127 (2007).
- [59] Sonier, J. E. *et al.* Direct search for a ferromagnetic phase in a heavily overdoped nonsuperconducting copper oxide. *Proc. Natl. Acad. Sci.* **107**, 17131–17134 (2010).

4 Quasi-particle Interference in Overdoped $(\text{Pb,Bi})_2\text{Sr}_2\text{CuO}_{6+\delta}$: Application of Noise Suppression through Self-Supervised Machine Learning

This chapter contributes to
Tromp et al. *in preparation*

The underdoped cuprates are infamous for their complex electronic structure in both real and momentum space, such as a pseudogap, disjointed Fermi arcs and nanometer inhomogeneity amongst others. As the doping increases to the overdoped regime the complexity in momentum space decreases through the disappearance of the pseudogap and the restoration of a full Fermi surface, while the real space electronic structure remains highly complex as discussed in Chapter 3. To try to explain how these two distinct views on the electronic structure fit together, we probe the momentum space structure through quasi-particle interference, thereby staying closer to real space inhomogeneity observed by STS. We implement a state-of-the-art self-supervised machine learning algorithm to suppress the noise present in the QPI images. The noise suppressed images reveal a full Fermi surface with an anti-nodal band shifting rigidly with increased doping. They also reveal a backbending of the band due to the superconducting gap and features around the gap edge associated with an additional density wave. These findings raise new questions on how the different probes of the electronic structure fit together.

4.1 Introduction

Of all electronic phases exhibited by the cuprate family, superconductivity in the overdoped regime was often assumed to be relatively straight-forward¹, assuming it to be a d-wave BCS superconductor originating from a Fermi liquid normal state, supported by observations of a full Fermi surface²⁻⁴ and quantum oscillations⁵ absent in the underdoped regime. Recent results however have shown that the overdoped cuprates are less conventional than this early consensus. In particular, the superconducting state has an anomalously low superfluid density⁶⁻⁸ and a large uncondensed spectral weight and the normal state shows residuals of strange metal phase at optimal doping⁹. Furthermore, superconductivity is not the only ordered state in the overdoped regime. The $4a_0$ charge order found in the underdoped regime^{10,11} extends into the overdoped, gradually weakening as the doping is increased further¹⁰. Close to the edge of the superconducting dome a different charge order seemingly appears^{10,12}, concomitant with ferromagnetic fluctuation^{13,14}. Lastly, the breakdown of superconductivity itself is highly unconventional as we have seen in the previous chapter.

The disappearance of superconductivity in $\text{Bi}_2\text{Sr}_2\text{CuO}_{6+\delta}$ occurs concomitantly with a Lifshitz transition^{3,15}. The flat dispersion associated with this transition has been shown to amplify superconducting fluctuations⁴, and plays a major role in the formation of a granular superconductor¹⁶. Previous STM results have shown patches of charge order with a wavelength closely associated with the van Hove Singularity (vHS)^{12,17,18} accompanying the Lifshitz transition, although it should be pointed out that there is little signature of this in momentum space and RIXS study disagree on the wavevector¹⁰. The spectral feature of the vHS, a peak in the density of states, has been shown to be highly inhomogeneous, shifting in energy, and disappearing and reappearing over a nanometer length scale (see Chapter 3). This then poses the question how the real space electronic structure, featuring a highly inhomogeneous LDOS, unusual vHS behavior, and nanometer sized puddles of charge order and metallic behavior in the superconducting state, and the momentum space electronic structure, featuring a full single band Fermi surface, no pseudogap, and no Fermi surface reconstruction due to density waves, combine to form one consistent view.

The ideal tool to bridge this gap between real space and momentum space is quasi-particle interference (QPI), being a real space nanoscale measurement used to extract momentum space information. QPI has a long history of valuable insights into the underdoped cuprates, particularly by mapping the gap structure^{19,20} and observing the transition from Fermi arcs to a full Fermi surface^{2,21}. Furthermore, Fourier transform based analyses of STS data has yielded key results into the charge density and pair density waves^{11,22–25} of this doping regime. An advantage of QPI over other momentum space probes is the ability to directly access unoccupied states, even at low temperatures. This is especially useful when characterizing the vHS. ARPES results have shown the Lifshitz transition associated with the vHS^{3,15} but cannot map the anti-nodal dispersion near this transition as this requires access to the unoccupied states. Furthermore, for momenta farther away from the anti-node or for doping levels further away from the Lifshitz transition the dispersion ARPES measures is heavily influenced by the gap, and extracting information about the normal state dispersion requires elevated temperatures^{26,27}. This too can be circumvented by access to the unoccupied states for which QPI can measure the dispersion for energies high enough that the gap no longer plays a role.

In this chapter we will characterize the anti-nodal dispersion electronic structure of the overdoped cuprates by performing QPI experiments on samples of the single layer cuprate $(\text{Pb,Bi})_2\text{Sr}_2\text{CuO}_{6+\delta}$ with T_c 's of 23K, 12K, and 3K (labeled OD23K, OD12K, and OD3K resp.). To do so, we will implement a self-supervised machine learning model to suppress pixel-independent noise present in the QPI images. Our data reveals a full Fermi surface, consistent with previous reports in this doping range^{2,15}, and a rigid shifting of the bands with increased doping. Furthermore, we observe a back-bending of the band due to the superconducting gap and shoulder-like features near the gap edge previously associated with a coexisting density wave²⁷. We also note the discrepancies between various methods for counting the number of carriers, such as the Luttinger count, the Hall carrier density, or the use of universal doping vs. T_c relations. Finally, we point out that there is no clear candidate for the ordered state responsible for the features around the gap edge.

4.2 Methods

4.2.1 QPI Measurements

We perform the STS measurements using an ultra-stable home built cryogenic STM setup²⁸. All samples are cleaved at cryogenic temperatures before being loaded in the STM head held at a temperature of 4.2K where all experiments are performed. The samples show an atomically flat surface revealing the Bi-O plane (see **Fig. 4.1a** for an example). The STS measurements were taken over a $50 \times 50 \text{ nm}^2$ field of view ($45 \times 45 \text{ nm}^2$ for OD23K) using a fine grid resolving the atomic lattice. The real-space conductance layers (**Fig. 4.1b**) show nm-scale modulations of the LDOS consistent with previous results. All data is drift corrected using the Lawler-Fujita algorithm^{24,29,30} (known as geometric phase analysis in other electron microscopy communities). As in Chapter 2, we normalize the conductance layers with their corresponding current layers by taking $dI/dV(r,eV)/(I(r,eV)/V)$ before taking the FFT to reveal the QPI patterns. **Figs. 4c,d** show the FFT of the $dI/dV(r,eV)$ and the normalized $dI/dV(r,eV)/(I(r,eV)/V)$ for the OD12K sample at $E = 10 \text{ meV}$ side by side. Note that the signal is sharper in **Fig 4.1d** but loses definition close to the Bragg peaks.

4.2.2 Self-supervised Machine Learning for Noise Suppression

The QPI signals shown in **Fig. 4.1** show a considerable amount of noise, making analysis of these images more difficult. The first remedy to limit the amount of noise is to measure longer, take longer or more averages of the spectra that form the initial conductance map. The success of this approach is limited by the maximum measurement time, which is already pushed when taking QPI measurements due to the size of the FOV. An alternative would be to smooth the QPI average by taking a moving average over the image with some window shape (typically a box or Gaussian filter). This however broadens the features in the image, undoing the gain in sharpness by taking the $dI/dV(r,eV)/(I(r,eV)/V)$.

To suppress the noise in the QPI images while preserving the sharpness we implement a machine learning algorithm for noise suppression or denoising. The core principle behind machine learning denoising, or image reconstruction in general, is that the structure of an image can be described with a number of parameters that is much less than the number of pixels of the image. As such, it should be possible to learn the underlying structure and reconstruct a noise free (or at least a noise suppressed) version of the image.

A neural network can be seen as a function f with an input x_i and output y_i governed by a set of parameters θ . The quality of the output y_i is given by the error or loss E calculated by comparing to the desired output or label \hat{y}_i through the loss function L :

$$E = \mathcal{L}(\hat{y}_i, y_i) = \mathcal{L}(\hat{y}_i, f(x_i|\theta)) \quad (4.1)$$

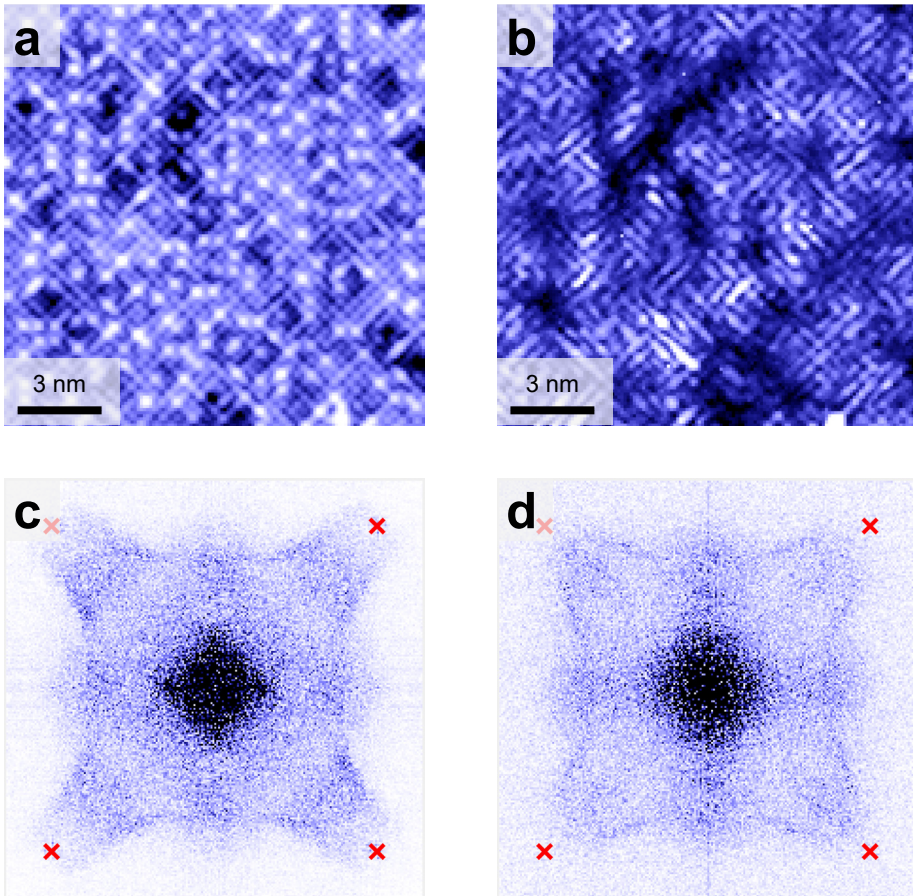


Figure 4.1 Bi2201 Topography and LDOS.

a) High resolution topography of a 15x15 nm field of view of the OD12K sample. The atomic lattice of the Bi-O plane is clearly resolved with the Pb dopants visible as bright white dots. *b)* LDOS modulations at $E = 10$ meV in the same FOV as *a)*. *c,d)* QPI signal of a 45x45 nm FOV of the OD12K sample at $E = 10$ meV revealed by taking the FFT of the dI/dV layer and the $(dI/dV)/(I/V)$ layer respectively after drift correction. The red crosses indicate the Bragg peaks from the atomic lattice.

The best output y_i is then the output that minimizes the error E . Typically this is not the case of the output y_i given by the initial set of parameters θ . To minimize E , during each cycle or epoch the loss is calculated and the parameters θ adjusted to yield a lower loss in the next epoch through gradient descent. When the error has been minimized the network has been trained. When the dataset consists of multiple elements, such as multiple QPI images, the dataset is often split into batches. During an epoch each image within a batch is fed to the network and a loss over the batch is calculated, after which the parameters θ are updated and the next batch is used. Over the course of one epoch each element of the dataset has been fed to the network. It is common practice to split off a part of the dataset into a validation dataset. The loss of the network over the validation network is calculated at regular intervals during training, but is not used to update the network parameters. As such, the loss over the validation dataset, or validation loss, represents the performance of the network on data not used for training, and is closely monitored during the training process.

The most common approach is to use supervised learning³¹⁻³³, i.e. using pairs of corrupted and clean images as inputs and labels (**Fig. 4.1a**). The network is trained by minimizing the loss between the clean example and the output when a noisy image is inputted. When a corrupted image without a clean example is then fed to the network, the output will be a noise-free version of the input provided the underlying structure of the input is similar enough to that of the images used to train the network. Recent work has shown that the clean images don't have to be clean at all³⁴. Having multiple noisy version of the same image can be enough to learn the structure of the image. If one characterizes the noise well enough to generate artificial noise similar enough to the noise in the original image, one can use this to generate the necessary training data to train the network and denoise the original data.

The issue with this approach is that it requires training data that is often not available in a scientific setting. Clean versions of the images are most often not available as scientific measurement setups are often already operating at their limits. Even acquiring multiple noisy copies of the same image is often not possible due to time constraints or changing experimental conditions. To work with STM data we need a self-supervised approach, i.e. one that doesn't require training data. Instead, we will assume some structure of the noise to denoise the QPI images. The method we implement here, called Noise2Void or Noise2Self^{36,37}, assumes that the noise is pixel independent, meaning that

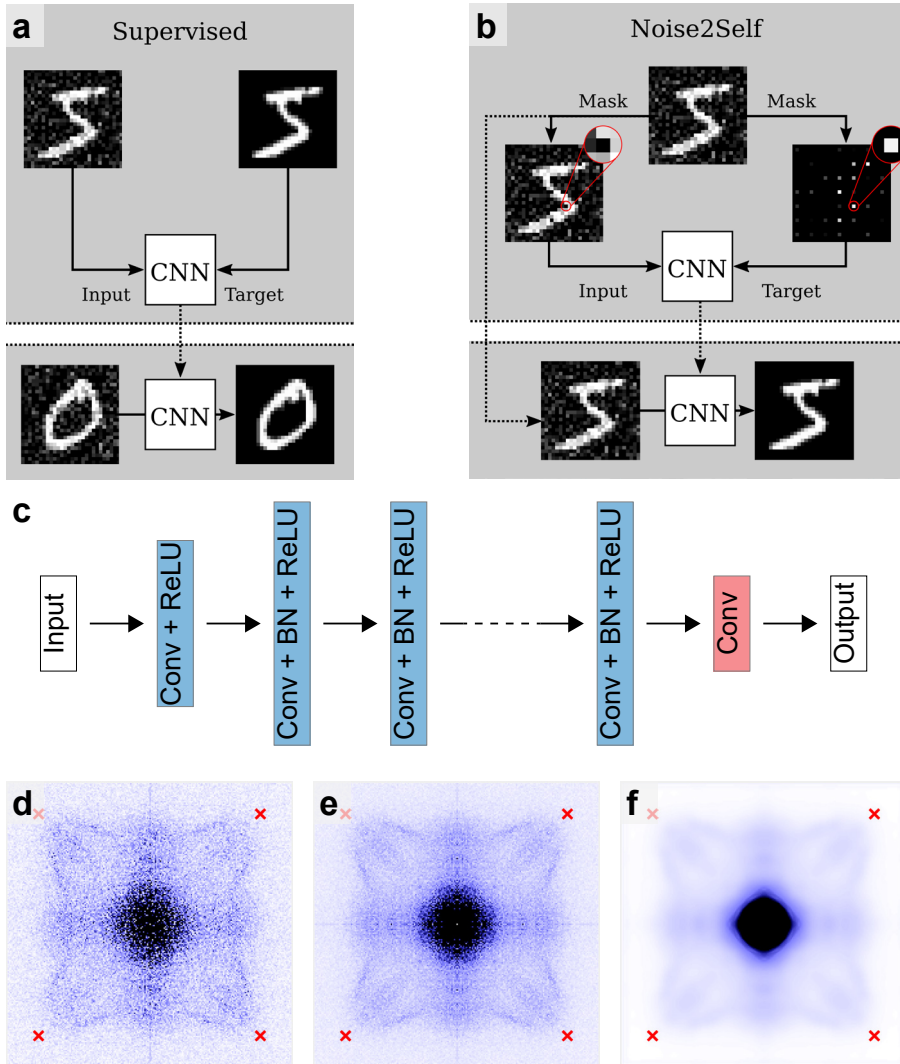


Figure 4.2 Self-supervised denoised QPI images.

a) Schematic of the traditional, supervised approach noise suppression. The network is trained on a pair of noisy inputs and clean targets. A different noisy image not part of the training data can then be denoised using the network. **b)** Schematic of Noise2Self. The input and targets now consist of a noisy image with some pixels masked and those masked pixel. The trained network can now be used to denoise the original image. **a, b** adapted from Ref. 35. **c)** DnCNN architecture used consisting of 17 layers containing each a convolutional (Conv) layer with 64 features, batch normalization (BN, except the first layer), and a ReLU activation function. These are followed by a convolutional layer generating the output. **d)** Example of QPI data before denoising (OD12K sample, $E = 10$ meV, same as Fig. 4.1d). **e)** Symmetrized version of **d)** for comparison to **f)**. **f)** Denoised and symmetrized using **d)** as input. The noise is clearly suppressed with the image slightly blurred.

the strength of the noise on one pixel will not tell anything about the strength of the noise on other pixels, neighbors included. For the mathematical reasoning behind this approach and details of the implementation we refer to the original papers^{36,37}. The idea of Noise2Self (**Fig. 4.2b**) is to alter the value of some pixels during each training step (usually setting the pixel to zero or to the average of its neighbors). The network will then assign new values to those pixels and the training loss is evaluated at those pixels. Which pixels are altered varies during training. The network will fill in the blanks of the missing pixels using the underlying structure it learned, without any pixel independent structure as it doesn't have access to the pixel it is trying to fill in. As such, the network can reconstruct a clean version of the noisy image. This approach to noise suppression has already found successful application in tomography^{35,38} and can also be used to optimize parameters for certain filters or dimension reduction techniques³⁷.

It is important that this approach only works for pixel independent noise. Anything else will be interpreted as part of the structure of the image. If there is structured noise present in the image, for example some repeating pattern, Noise2Self will preserve this structure, while approaches based on clean training data can also suppress this type of noise³⁶. Most notably this also holds for any artifact that might be introduced into the data during the measurement.

The network architecture we will use is a DnCNN network³² (see **Fig. 4.2c**), similar to the one used in the original Noise2Self paper³⁷, implemented using Python's TensorFlow package. We will use 17 layers, with 64 features each. The loss is calculated using the mean squared error, and we will use a learning rate of 0.01 during training. The data is layer-wise mean subtracted before taking the FFT and afterwards normalized to [0,1] layer-wise. The QPI data is split into batches of 10 images which are shuffled each training step. The network is trained for 100 epochs. The noise suppressed images are then symmetrized. An example of the data used as output and fully processed data is shown in **Figs. 4.2d-f**. The algorithm has worked as intended, with the noise in **Fig. 4.2f** suppressed compared to **Fig. 4.2d,e**. The reconstruction is not perfect, as the image is slightly blurred compared to the inputs.

4.3 Results

4.3.1 Fermi surface

We start by looking at the QPI signal at $E = 0\text{meV}$, showing the interference from states on the Fermi surface. In this doping range we expect a full Fermi surface^{2,21}, meaning the QPI signal will trace the shape of the Fermi surface with $q = 2k_F$. The $E = 0\text{meV}$ layers shown in **Fig. 4.3a-c** for the OD3K, OD12K, and the OD23K samples indeed have a signal at $q = 2k_F$ consistent with a full Fermi surface of a single band. In particular there is no sign of octet model scattering vectors characteristic of the pseudogap in the underdoped regime. The horizontal and vertical line through the center in **Fig. 4.3b** are the result of an unknown artifact only present in the OD12K measurement. Note that the signal at the anti-node next to the Bragg peaks are very faint or absent. This seems to be the result of two factors: first, these scattering vectors are already weaker in the dI/dV QPI signals (see **Fig. 4.1c**) and second, these vectors become even weaker after normalizing to $(dI/dV)/(I/V)$. The reason behind these two factors are unclear. Fainter signal at the anti-nodes can be the result of a combination of details of the scattering process and conditions of the STM tip. Why normalization weakens the signal at large q vectors is also not clear, though it should be noted that something similar happens in the rhodates in Chapter 2, as seen in **Fig. 2A.1**.

We trace the Fermi surfaces by fitting the peak position of the $q = 2k_F$ signal along the cuts indicated by the red lines in **Fig. 4.3c**. The result is shown in **Fig. 4.3d**, where we have divided the values for the q vectors by 2 and rotated them to show the band from which the scattering originates in the 1st Brillouin Zone (BZ). We also show a tight binding fit^{2,27} to the Fermi surfaces. There is very little difference between the 3 Fermi surfaces and their fits, especially for the OD3K and OD12K samples. This is due to the fact that the band only moves very little for these doping values, especially in the nodal region, combined with the uncertainty of the fit when extracting the Fermi surface.

To see the shift of the band as a function of doping we plot the ε_0 parameter of the tight binding model, which governs the band shift, as a function of doping in **Fig. 4.4a**, together with the ε_0 parameters determined by He et al.² with the QPI patterns of the same $(\text{Pb,Bi})_2\text{Sr}_2\text{CuO}_{6+\delta}$ compound using the same tight binding model. The doping levels on the x-axis are determined using the T_c of the samples and the Presland formula for the relation between doping and

T_c ³⁹. We find lower values for ε_0 and a different slope as a function of doping. We could fit a straight line through our point to quantify the difference in offset and slope. Given the number of data points however this would not be very reliable. Regardless, our results are not fully consistent with their previous results, where we point out, in addition to the earlier mentioned precision of our Fermi surface extraction, the values for ε_0 determined by He et al. are obtained by ‘fitting’ the tight binding model to their data by eye.

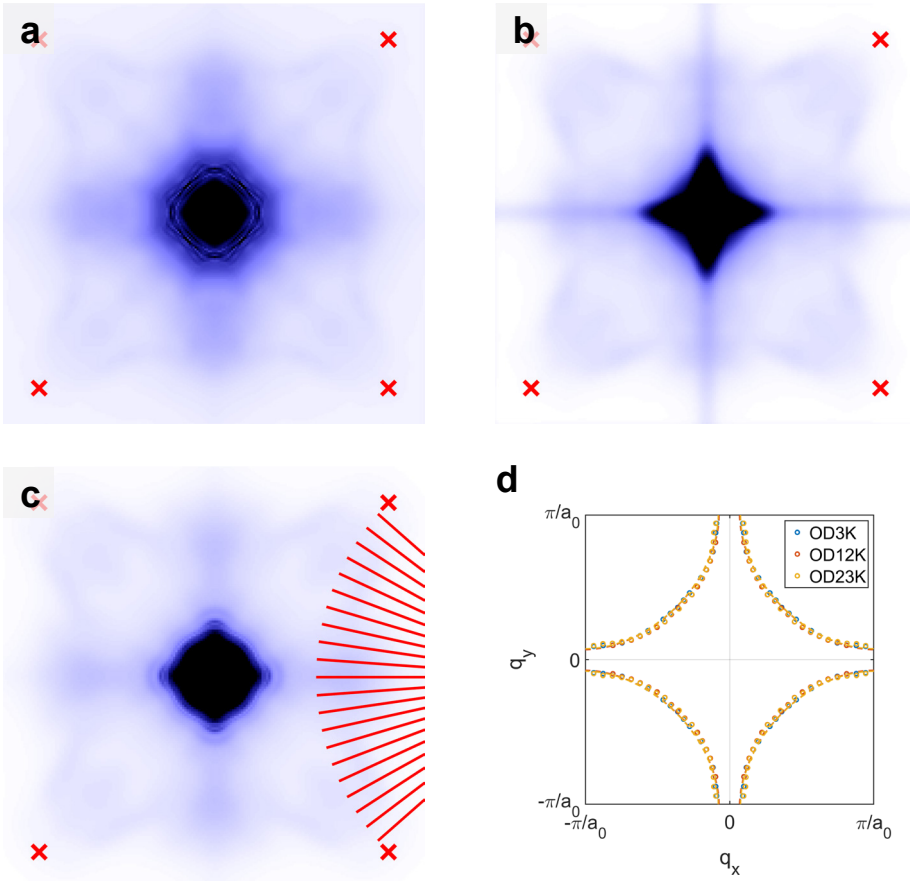


Figure 4.3 Bi2201 QPI Fermi surfaces.

a-c) The QPI signal at $E = 0\text{meV}$ for the OD3K, OD12K, and OD23K samples respectively after normalizing to $(dI/dV)/(I/V)$ and denoising using the Noise2Self algorithm. The red crosses indicate the position of the Bragg peaks. The red lines in **c)** show the cuts used to extract the Fermi surface scattering vectors. **d)** The Fermi surfaces determined using the QPI pattern in **a-c)** by dividing the scattering vectors by two, rotating them and duplicating them to show two parts of the Fermi surface. The dashed lines show the tight binding fits to the Fermi surface for each sample.

A different way to show the shifting of the band is to look at the area of the Fermi surface and calculate the Luttinger count. The result is shown in **Fig. 4.4b**, together with the Luttinger counts determined by He et al. Similarly to the result for ε_0 we find a discrepancy between our result and theirs, not surprisingly given that ε_0 and Luttinger count are related. It is important to note that for $(\text{Pb,Bi})_2\text{Sr}_2\text{CuO}_{6+\delta}$ the Luttinger count does not match the doping levels from the Presland formula³⁹, as was noticed previously for both single layer and double layer Bi-based cuprates $(\text{Pb,Bi})_2\text{Sr}_2\text{CuO}_{6+\delta}$ and $\text{Bi}_2\text{Sr}_2\text{CaCu}_2\text{O}_{8+\delta}$ ^{2,3}. Still this universal formula for doping vs. T_c is useful as long as the relation depicted in **Fig. 4.4b** shows a straight line.

4.3.2 Anti-nodal Dispersion

Next we look at the anti-nodal dispersion by taking a series of cuts perpendicular to the $(0,0)$ - $(2\pi,2\pi)$ line shown in **Fig. 4.5a**. The cuts are taken more towards the midway point between nodal and anti-nodal since the signal fades away moving closer to the anti-node. The cuts, examples of which are shown in **Fig. 4.5b-d**, feature both a gap around Fermi level and a band crossing E_F . The cuts in **Fig. 4.5b,c** have a strongly reduced intensity directly around E_F due to the gap but note that there are still clear QPI for the $E = 0\text{meV}$ layer, as seen in **Fig. 4.3a,b**. The cut in **Fig. 4.5d** also has reduced intensity near E_F but not

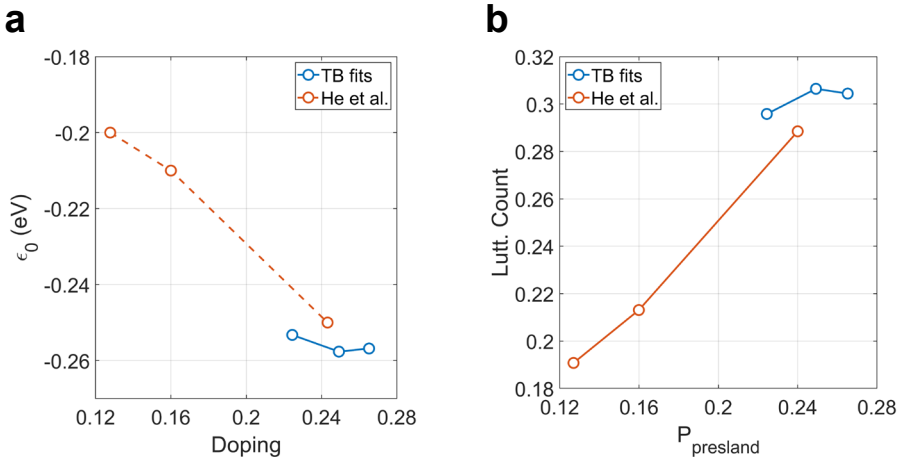


Figure 4.4 Tight binding ε_0 and Luttinger count.

a) The ε_0 parameter of the tight binding fits shown in **Fig. 4.3d** as a function of doping in blue. The doping values on the x-axis are calculated using the T_c of the samples and the Presland formula³⁹. The ε_0 values determined previously² for the same compound are shown in red. **b)** The Luttinger count calculated using the area of the Fermi surface as a function of doping in blue. Previously determined values are shown in red.

at E_F . This is most likely an artifact from the noise suppression, a point we will get back to in section 4.4. The fact that there is still QPI associated with a full Fermi surface at $E = 0\text{meV}$ for superconducting samples is a result of the pronounced gap filling occurring in this doping range described in Chapter 3.

Next, we fit the peak position of momentum distribution curves (MDCs) of the cuts to extract the band crossing E_{pr} shown in **Fig. 4.5b-d** as the blue dots and plotted together in **Fig. 4.6a** for the cut highlighted in **Fig. 4.5a**. For cuts

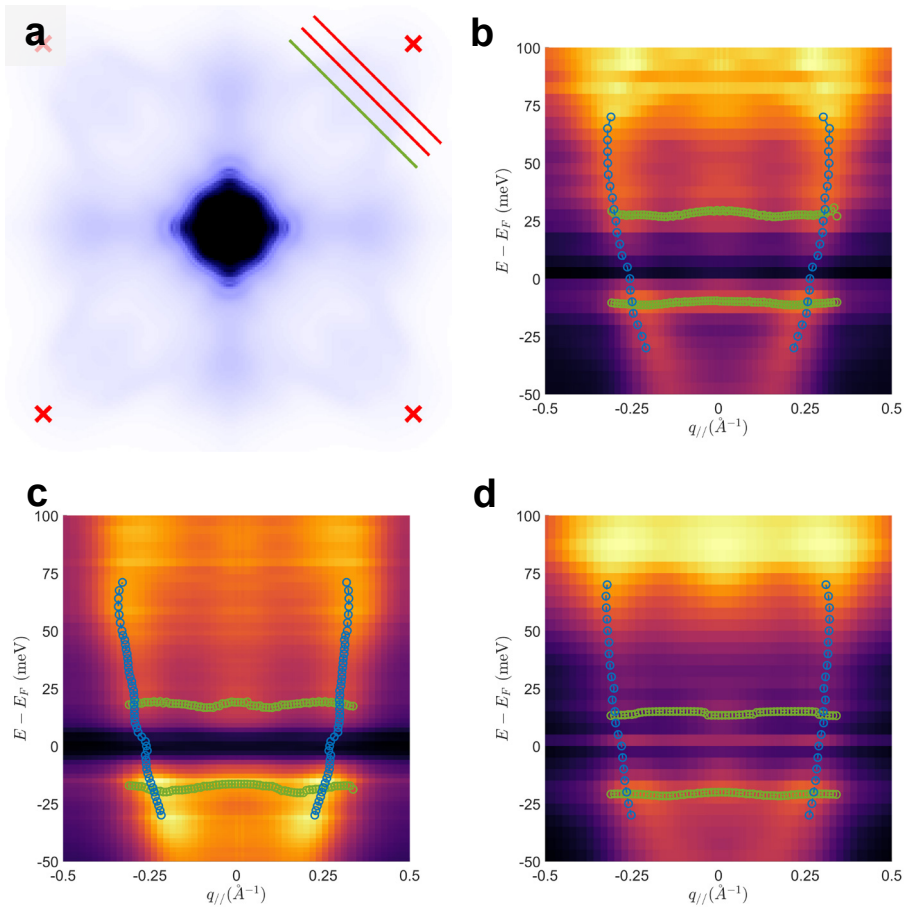


Figure 4.5 Anti-nodal dispersion.

a) The $E = 0\text{meV}$ QPI layer for the OD23K sample indicating the lines along which the cuts are taken used to extract the bandstructure. The green line shows the cut shown in **b-d**. The red crosses indicate the position of the Bragg peaks. **b-d)** The cuts along the green line in **a)** for the OD3K, OD12K, and OD23K sample respectively. The blue points show the peak position of the fitted MDCs, the green points show the peak position of the fitted EDCs.

taken at the anti-node where the bandstructure has a saddle point (the vHS) the dispersion is parabolic, disregarding any possible back bending due to a gap. The cuts in **Fig. 4.5** however are taken away from the anti-node so that

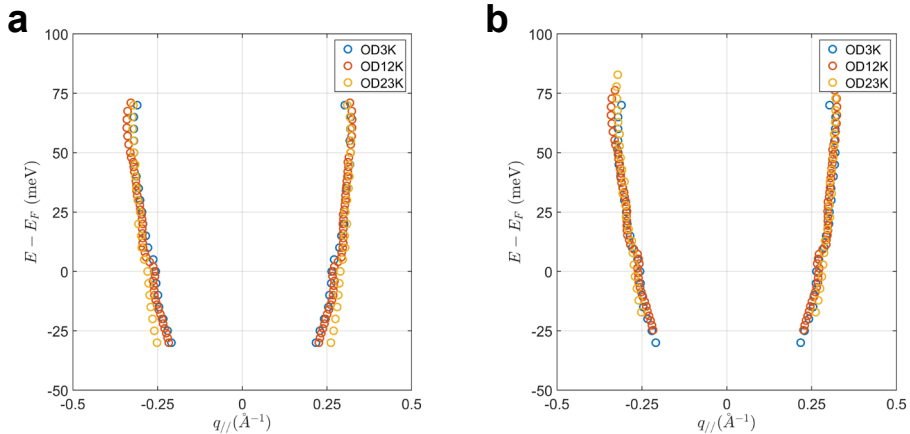


Figure 4.6 Bandshift measurement.

a) The anti-nodal dispersion for the OD3K, OD12K, and OD23K extracted from the cuts shown in **Fig. 4.5b-d** by fitting the MDC peak positions. The bandshifts are measured by finding the shift to the OD12K and OD23K dispersions that minimizes the sum of the point-wise distances to the OD3K dispersion. The result of the shifting procedure for the data shown in **a)** is shown in **b)**.

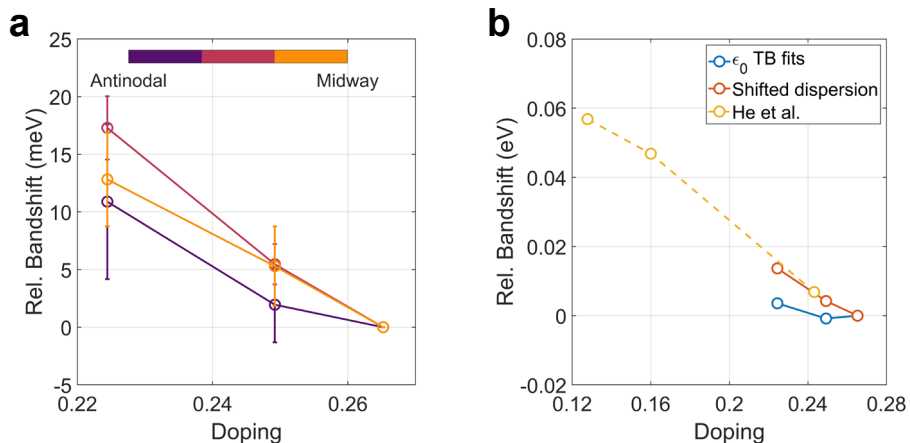


Figure 4.7 Bandshift doping dependence.

a) The extracted QPI bandshifts relative to the OD3K sample for the three cuts indicated in **Fig. 4.5a**, with the cut labeled anti-nodal being closest to the Bragg peaks and the one labeled midway furthest. *b)* The average of the shifts shown in **a)** compared to the shifts determined by tight-binding fits to the QPI Fermi surface, and compared to the shifts determined by Ref. 2.

the dispersion is no longer guaranteed to be parabolic. Therefore we take an agnostic approach to measuring the bandshift. We add a shift manually to the dispersion of the OD12K and OD23K and calculate the relative distance for points at constant q_{\parallel} . The true bandshift is then the shift which minimizes the sum of the squared distances. The shifted dispersion for the highlighted cut in **Fig. 4.5a** are shown in **Fig. 4.6b**. We then repeat this procedure for all cuts taken. The resulting bandshifts relative to the OD3K sample are shown in **Fig. 4.7a** for each cut, where the errorbars give the 95% confidence interval for the calculated shifts. We find that, within error, the shifts follow a straight line, where the caution of the number of data points again holds. The straight line of the shifts, or the rigidity of the bandshifts, becomes more apparent when we average the calculated values over the different cuts used and plot them against previous results², as we have done in **Fig. 4.7b**. We find a good agreement with the slope of the $\varepsilon_0(p)$ line determined by He et al. Note that the data points for ε_0 were shifted so that all the curves coincide at a shift of 0 for the OD3K sample. This is done as the shift measured from movement of the bandstructure only gives relative values of this shift, versus more absolute values when calculating ε_0 from tight-binding model.

Another feature of the anti-nodal electronic structure becomes apparent when we look at the peak positions of the energy distribution curves (EDCs, green points in **Fig. 4.5b-d**). We find shoulder features at lower q near both gap edges for all samples. The shoulder above the Fermi level can be attributed to back bending of the band due to the band, although it should be noted that this occurs at unusually large energies for the OD3K sample. The exact shape of the backbended band reveals important information on the nature of the gap. For a purely superconducting gap we expect a particle-hole symmetric bending of the band, while for other ordered states the bending does not necessarily have this symmetry. The data presented here however lacks the resolution to conclusively determine whether the bending is particle-hole symmetric.

Another clue to the nature of the gap stems from the feature near the gap edge below the Fermi level. Here, for a superconducting gap, we expect band bending only to occur for momenta larger than k_F (or q_F in our case). We find that this shoulder is present in all cuts for each sample. The large extension in q and its lack of dispersion means it is unlikely to stem from purely bandstructure QPI. Such a feature has been observed before by ARPES in the same compound²⁷, where it was attributed to superconductivity co-

existing with an additional density wave. The precise nature of the density wave determines some of the details of the back bending, but all scenarios share this additional low momentum feature. There are indications of an additional ordered state next to superconductivity in this doping range for Bi2201, however their link to this feature remains to be investigated

4.4 Discussion

4.4.1 Artifacts of Noise Suppression

The observation that the shoulder feature above E_F occurs at an unusually large energy for the OD3K sample warrants a closer examination of the denoising algorithm. Another unusual aspect of the OD3K data is that the gap seems to be asymmetric. The suppression of intensity due to the gap seems to extend to larger energies above E_F than below. A comparison of the anti-nodal cuts from noise suppressed data with the $(dI/dV)/(I/V)$ data used as input, shown in **Fig. 4.8**, shows that the asymmetry is a result of the noise suppression. The comparison shows that the dispersion is well-preserved by the noise suppression, together with the shoulder features around the gap, although the one above E_F has moved up in energy. The comparison also shows that the relative intensities of the energy layers is changed quite drastically, a point

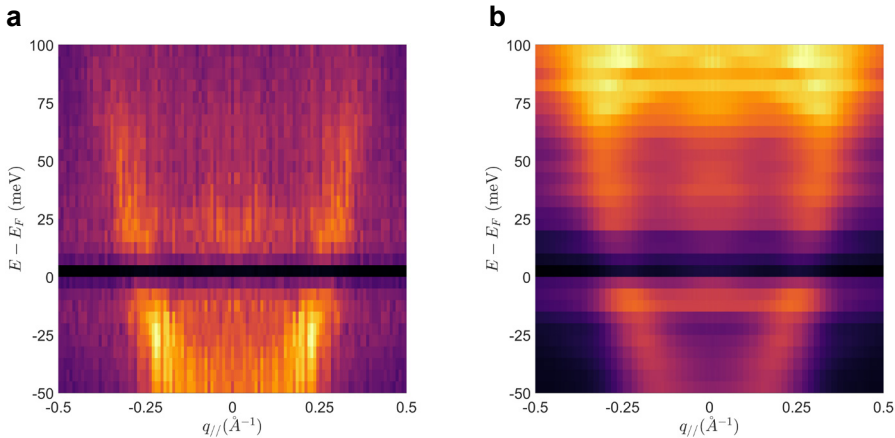


Figure 4.8 Before and after comparison anti-nodal cuts.

a) Anti-nodal cut taken from the OD3K $(dI/dV)/(I/V)$ data before noise suppression along the green line indicated in **Fig 4.5a**. **b)** The same cut after noise suppression of the full data set. The main features are preserved (dispersion, shoulders at the gap edge), but the relative intensities of the energy layers has changed drastically.

emphasized when we plot the average value of the energy layers, shown in **Fig. 4.9a**. It is clear that relative layer intensities are not preserved during the noise suppression. This is a result of the 2D network design used combined with an imperfect reconstruction of the images. Ultimately, the images are fed one by one to the network and shuffled between epochs. Any information about the relative information of the image in the 3D dataset, or any information about neighboring layers is lost during the denoising. As a result, the intensity of a layer relative to the other layers is can exhibit sharp jumps or vary more freely than pixel intensities within a layer, for which neighborhood information is provided to the network to suppress sharp jumps. The fact that there is still some gap structure present in the noise suppressed data is in part due to the normalization applied before the data is fed to the network. The data is layer-wise normalized to the interval $[0, 1]$, which is then applied in reverse to the network output. The application of the reverse normalization restores some of the relative intensity, but not all.

The remedy for this would be to implement a 3D network, which takes the dataset as a whole as input. Training such a network would require unreasonably long computation times for anything but a very small dataset, or require running on a supercomputer. A good intermediate solution is a 2.5D network, as was done for the Noise2Self tomography implementation³⁸. In such a network, the input is comprised of three images: the image to be denoised and its neighbors in the 3D dataset. The addition of the neighboring layers to the actual input does two things: first it improves the overall quality of the denoising as more information is known to the network through the addition of extra neighbors to the masked pixels. Second it can add context to the input in the third dimension not present for a strictly 2D network. As such, a 2.5D network can suppress sharp changes in intensity along the third direction.

Further improvements to the network are possible. While common for image reconstruction tasks, the DnCNN architecture used here is but one of many. Other common architectures include Red30⁴⁰ and U-Net⁴¹. As for the layers used within DnCNN there is room to optimize the number of layers used, the number of feature per layer, or the use of dropout. Other optimizations include the activation function or the loss function. The mean squared error used here is a default choice for image reconstruction, but given the size of the images, switching to loss functions which tries to capture structural similarity might be worthwhile.

In the current implementation of the noise suppression the network is trained on each dataset separately. A possible route towards improved performance and more general applicability is to pool the data together and train the network once on the new bigger dataset. The rationale being that, the samples being from the same compound family, the QPI images across the samples share enough of a common underlying structure. For the current data this would require down sampling some images to ensure equal image size throughout the whole dataset. This approach would open the door to a more generally applicable network for QPI images from distinct compounds having distinct bandstructures through transfer learning. Transfer learning extends the range of applicability by training a deep network on a large dataset (e.g. a collection of QPI dataset from different samples and/or compound families). This network can then be applied to a dataset not seen before, and not necessarily having a structure present in the training dataset, by retraining only the top layer(s) of the network. The deep parts of the network then encode the general common elements of QPI images (e.g. common noise sources) while the top layers take care of dataset specific structures. This would also have the added benefit of speeding up the computation time for each new dataset once the deep network has been trained.

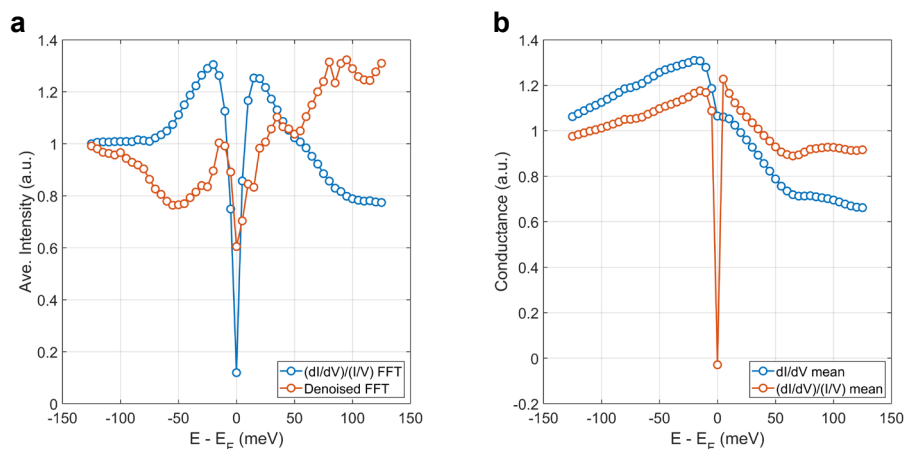


Figure 4.9 Layer intensities before and after noise suppression.

a) The average intensity of the QPI layers of the OD3K sample before and after noise suppression as a function of energy. While the averages for the $(dI/dV)/(I/V)$ before denoising resembles the real space average, the averages after denoising have lost that resemblance. **b)** Comparison of the real space averages for the dI/dV data and the $(dI/dV)/(I/V)$ data for the OD3K sample. Normalizing layer-wise by the current has made the gap much more pronounced.

As a side note, the uncharacteristically deep gap for the OD3K sample shown by the blue curve in **Fig. 4.9a** is a result of the normalization of the dI/dV spectra with the current layers I , as shown by the comparison of the real space averages of the dI/dV spectra and the $(dI/dV)/(I/V)$ spectra shown in **Fig. 4.9b**. The current I and the bias voltage V are in principle roughly linearly related in the small energy window around $V = 0$, so that the ration I/V remains constant even as V and with it I approach zero. Even so, small fluctuations in the value for I registered by the STM hardware can lead to large differences in the normalized $(dI/dV)/(I/V)$. To temper these differences we add a $10\mu\text{V}$ offset to the bias during normalization, to only partial success as seen by the sharpness of the gap in the $(dI/dV)/(I/V)$ average depicted in **Fig. 4.9b**.

4.4.2 Carrier Concentration and Bandshifts

Bandshifts in overdoped cuprates have been reported before in both $\text{Bi}_2\text{Sr}_2\text{CuO}_{6+\delta}$ ^{2,42} and $\text{La}_{2-x}\text{Sr}_x\text{CuO}_4$ ^{42,43}, although their doping dependence is not trivial. The magnitude of the shifts increase strongly past overdoping at $p=0.16$, for $\text{La}_{2-x}\text{Sr}_x\text{CuO}_4$ even becoming non-zero only then⁴². Interestingly, this occurs before the closing of the pseudogap around $p^* = 0.19 - 0.20$ ⁴⁴, suggesting the bandshifts are decoupled from the restoration of the full Fermi surface. Instead, the increased magnitude of the bandshifts seems to coincide with the start of a gradual change in the Hall carrier density from $n_{\text{H}} = p$ to $n_{\text{H}} = 1+p$ ⁴⁵. The rigidity of the shift, behavior typical of a Fermi liquid combined with the gradual change of n_{H} to $n_{\text{H}} = 1+p$ and the emergence of a T^2 component of the resistivity⁴⁵ suggests that these doped carriers constitute a coherent Fermi liquid-like normal state, coexisting with an incoherent electron fluid with T-linear resistivity, $n_{\text{H}} = p$, and little to no shifts in the chemical potential^{42,45}. This tentative relation between bandshift magnitude and n_{H} would imply another change in shift magnitude at the end of the superconducting dome, where n_{H} saturates to $n_{\text{H}} = 1+p$. QPI investigation beyond the superconducting dome will test this relation in the metallic state past the Lifshitz transition.

Future STM work can relate these two fluids to spectral features (superconducting or pseudogap, vHS) by identifying the real space distribution of these features and applying masks to the dI/dV data before taking the FFT to reveal the QPI patterns, a technique used previously to study charge order in $\text{Bi}_2\text{Sr}_2\text{CuO}_{6+\delta}$ ^{11,23}. The machine learning techniques detailed in this chapter can help overcome the challenges of the additional noise introduced by such real space masking.

Interestingly, there is a mismatch between the Luttinger count extracted from STM and ARPES and universal formulas for doping vs T_c , as was noted before^{2,42,44}. Adding to the puzzle, the relation between Luttinger count and universal doping formulas does appear to be linear across the full superconducting dome², implying that the amount of holes doped per dopant is constant over this part of the phase diagram. This appears at odds with the doping dependence of the bandshifts and Hall carrier concentration, which feature a sharp change at optimal doping^{42,45}. The former discrepancy is especially concerning as both the Luttinger count and the bandshifts are typically determined by a tight-binding characterization of the Fermi surface, although we have shown that the bandshift still holds without the use of tight-binding models. A possible solution to this is by noting that the tight-binding hopping parameters can be doping dependent, for which there is precedent^{42,43}. This doping dependence seems to smooth however, rather than featuring a pronounced change at $p = 0.16$ the bandshift and n_H have. Why the drastic increase in free carrier deduced from n_H is not reflected in a similarly rapid change in the Fermi surface area remains an open question. One proposal that the Luttinger count only counts coherent carriers⁴⁴ seems unlikely as the relation between Luttinger count and universal formulas is linear over a doping range larger than the one in which coherent carriers are added. Investigation into the non-superconducting overdoped regime will reveal how these relations hold when there are no incoherent carriers present. Alternatively, the high Luttinger count is the result of surface effects, to which both STM and ARPES are susceptible, versus bulk measurement on which n_H and the universal doping formulas are based. These surface effects would then most likely be caused or enhanced by the physics of the cuprates, as we have shown in Chapter 2 that bulk and surface probes of the bandstructure are in agreement with each other for Fermi liquid systems.

4.4.3 Density Waves in Overdoped $\text{Bi}_2\text{Sr}_2\text{CuO}_{6+\delta}$

The observation of the shoulder features at the gap edge (**Fig. 4.5b-d**) has been attributed to the presence of some density wave in addition to the backbending of the band due to superconductivity. This raises the question what that density wave is. There are two main candidates in overdoped single layer cuprates: a charge density wave (CDW) or ferromagnetic fluctuations (FMF). CDW order has been observed across the overdoped regime in both $\text{Bi}_2\text{Sr}_2\text{CuO}_{6+\delta}$ ¹⁰⁻¹² and $\text{La}_{2-x}\text{SrCuO}_4$ ⁴⁶, albeit with markedly different doping dependence. In the latter compound X-ray diffraction

studies have found CDW order extending over the entirety of the overdoped superconductivity regime with a nontrivial doping dependence, but only disappearing concomitantly with superconductivity at the edge of the dome. In contrast, in $\text{Bi}_2\text{Sr}_2\text{CuO}_{6+\delta}$ the overdoped CDW shows re-entrant behavior, being disconnected from the underdoped CDW that gradually disappears in the overdoped¹¹. The re-entrant behavior only starts to show around a T_c of 15K^{10,12}. The fact that we observe the shoulder feature for the OD23K sample disqualifies the strongly overdoped CDW as the cause for all three samples. It could be possible that the feature in the OD23K sample is caused by remnants of the overdoped CDW, while for the higher doped samples it is caused by the re-entrant CDW. More detailed calculations investigating the difference in band bending between these two CDWs combined with QPI or ARPES measurements with high enough resolution to resolve those differences are needed to resolve this issue. The shoulder-like feature above E_F accessible by QPI or high-temperature ARPES (if the appropriate temperature range exists) can provide additional information on the exact structure of the backbending. It should be noted that X-ray diffraction and STM disagree on the wavevector of re-entrant CDW^{10,12}. Particularly, the STM observation can be interpreted as QPI resulting from anti-nodal scattering, given that a clear momentum space signature of this CDW is absent in the STM measurements¹². Also note that there is a gap in the doping range in the available X-ray data, leaving room for an interpretation where the proposed CDW is not re-entrant, but a continuation of the underdoped CDW. As the observation of the shoulder-like feature only provides indirect evidence for a CDW, the question whether a CDW exists across the overdoped regime in $\text{Bi}_2\text{Sr}_2\text{CuO}_{6+\delta}$ remains open.

An alternative explanation involves the FMF found in overdoped $\text{La}_{2-x}\text{SrCuO}_4$ ^{13,14} and $\text{Bi}_2\text{Sr}_2\text{CuO}_{6+\delta}$ ⁴⁷. In the latter case the FMF appear to extend over a doping range compatible with the samples studied here. The FMF have not however been shown to form static order at higher doping or lower temperatures. How fluctuating order impacts the backbending remains to be investigated.

4.5 Conclusion & Outlook

In conclusion, we have investigated the anti-nodal electronic structure of overdoped $\text{Bi}_2\text{Sr}_2\text{CuO}_{6+\delta}$ using QPI. We have implemented a state-of-the-art self-supervised machine learning algorithm to suppress the noise in the QPI

images. Using the noise suppressed data we have shown that the anti-nodal band shows a rigid bandshift with overdoping. Additional studies into the non-superconducting regime are needed to resolve discrepancies between the doping dependences of the bandshifts^{42,43}, the Luttinger count^{2,44}, and the Hall carrier density⁴⁵. The backbending of the band due to the superconducting gap features shoulder-like features near the gap edge associated with the presence of a density wave²⁷, whose nature remains unknown. More detailed calculations, focused particularly on the types of CDW with a doping dependent scattering vector and weak coherence proposed by X-ray and STM experiments combined with higher resolution experiments are needed to reveal the origins of the band bending and the associated density wave. The findings presented here reveal a picture where QPI and ARPES appear in agreement over the momentum space electronic structure, but in disagreement with other probes such as transport and X-ray diffraction over the carrier density and the presence and doping dependence of an additional ordered state next to superconductivity. More detailed studies of the electronic structure around the gap from both experimental and theoretical/computational viewpoint over an extended doping range are needed to bridge the gap between the various probes.

4.6 References

- [1] Keimer, B., Kivelson, S. A., Norman, M. R., Uchida, S. & Zaanen, J. From quantum matter to high-temperature superconductivity in copper oxides. *Nature* **518**, 179–186 (2015).
- [2] He, Y. *et al.* Fermi surface and pseudogap evolution in a cuprate superconductor. *Science* **344**, 608–611 (2014).
- [3] Drozdov, I. K. *et al.* Phase diagram of $\text{Bi}_2\text{Sr}_2\text{CaCu}_2\text{O}_{8+\delta}$ revisited. *Nat. Commun.* **9**:5210 (2018).
- [4] He, Y. *et al.* Superconducting Fluctuations in Overdoped $\text{Bi}_2\text{Sr}_2\text{CaCu}_2\text{O}_{8+\delta}$. *Phys. Rev. X* **11**, 031068 (2021).
- [5] Vignolle, B. *et al.* Quantum oscillations in an overdoped high- T_c superconductor. *Nature* **455**, 952–955 (2008).
- [6] Uemura, Y. J. *et al.* Magnetic-field penetration depth in $\text{Tl}_2\text{Ba}_2\text{CuO}_{6+\delta}$ in the overdoped regime. *Nature* **364**, 605–607 (1993).
- [7] Lemberger, T. R., Hetel, I., Tsukada, A., Naito, M. & Randeria, M. Superconductor-to-metal quantum phase transition in overdoped $\text{La}_{2-x}\text{Sr}_x\text{CuO}_4$. *Phys. Rev. B* **83**, 140507 (2011).

- [8] Bozovic, I., He, X., Wu, J. & Bollinger, A. T. Dependence of the critical temperature in overdoped copper oxides on superfluid density. *Nature* **536**, 309–311 (2016).
- [9] Mahmood, F., He, X., Božović, I. & Armitage, N. P. Locating the Missing Superconducting Electrons in the Overdoped Cuprates $\text{La}_{2-x}\text{Sr}_x\text{CuO}_4$. *Phys. Rev. Lett.* **122**, 027003 (2019).
- [10] Peng, Y. Y. *et al.* Re-entrant charge order in overdoped $(\text{Bi,Pb})_{2.12}\text{Sr}_{1.88}\text{CuO}_{6+\delta}$ outside the pseudogap regime. *Nat. Mater.* **17**, 697–702 (2018).
- [11] Webb, T. A. *et al.* Density wave probes cuprate quantum phase transition. *Phys. Rev. X* **9**, 021021 (2019).
- [12] Li, X. *et al.* Evolution of Charge and Pair Density Modulations in Overdoped $\text{Bi}_2\text{Sr}_2\text{CuO}_{6+\delta}$. *Phys. Rev. X* **11**, 11007 (2021).
- [13] Kopp, A., Ghosal, A. & Chakravarty, S. Competing ferromagnetism in high-temperature copper oxide superconductors. *Proc. Natl. Acad. Sci.* **104**, 6123–6127 (2007).
- [14] Sonier, J. E. *et al.* Direct search for a ferromagnetic phase in a heavily overdoped nonsuperconducting copper oxide. *Proc. Natl. Acad. Sci.* **107**, 17131–17134 (2010).
- [15] Ding, Y. *et al.* Disappearance of Superconductivity and a Concomitant Lifshitz Transition in Heavily-Overdoped $\text{Bi}_2\text{Sr}_2\text{CuO}_6$ Superconductor Revealed by Angle-Resolved Photoemission Spectroscopy. *Chinese Phys. Lett.* **36**, 017402 (2019).
- [16] Li, Z. X., Kivelson, S. A. & Lee, D. H. Superconductor-to-metal transition in overdoped cuprates. *npj Quantum Mater.* **6**:36 (2021).
- [17] Piriou, A., Jenkins, N., Berthod, C., Maggio-Aprile, I. & Fischer. First direct observation of the Van Hove singularity in the tunnelling spectra of cuprates. *Nat. Commun.* **2**:221 (2011).
- [18] Li, X. *et al.* Quasiparticle interference and charge order in a heavily overdoped non-superconducting cuprate. *New J. Phys.* **20**, 063401 (2018).
- [19] McElroy, K. *et al.* Relating atomic-scale electronic phenomena to wave-like quasiparticle states in. *Nature* **422**, 592–596 (2003).
- [20] Kohsaka, Y. *et al.* How Cooper pairs vanish approaching the Mott insulator in $\text{Bi}_2\text{Sr}_2\text{CaCu}_2\text{O}_{8+\delta}$. *Nature* **454**, 1072–1078 (2008).
- [21] Fujita, K. *et al.* Simultaneous transitions in cuprate momentum-space topology and electronic symmetry breaking. *Science* **344**, 612–616 (2014).
- [22] Kohsaka, Y. *et al.* An intrinsic bond-centered electronic glass with unidirectional domains in underdoped cuprates. *Science* **315**, 1380–1385 (2007).
- [23] Wise, W. D. *et al.* Imaging nanoscale Fermi-surface variations in an inhomogeneous superconductor. *Nat. Phys.* **5**, 213–216 (2009).
- [24] Lawler, M. J. *et al.* Intra-unit-cell electronic nematicity of the high-T_c copper-oxide pseudogap states. *Nature* **466**, 347–351 (2010).

- [25] Hamidian, M. H. *et al.* Detection of a Cooper-pair density wave in $\text{Bi}_2\text{Sr}_2\text{CaCu}_2\text{O}_{8+x}$. *Nature* **532**, 343–347 (2016).
- [26] Hashimoto, M. *et al.* Particle-hole symmetry breaking in the pseudogap state of Bi2201 . *Nat. Phys.* **6**, 414–418 (2010).
- [27] He, R. H. *et al.* From a single-band metal to a high-temperature superconductor via two thermal phase transitions. *Science* **331**, 1579–1584 (2011).
- [28] Battisti, I., Verdoes, G., Van Oosten, K., Bastiaans, K. M. & Allan, M. P. Definition of design guidelines, construction, and performance of an ultra-stable scanning tunneling microscope for spectroscopic imaging. *Rev. Sci. Instrum.* **89**, 123705 (2018).
- [29] Zeljkovic, I. *et al.* Scanning tunnelling microscopy imaging of symmetry-breaking structural distortion in the bismuth-based cuprate superconductors. *Nat. Mater.* **11**, 585–589 (2012).
- [30] Fujita, K. *et al.* Direct phase-sensitive identification of a d-form factor density wave in underdoped cuprates. *Proc. Natl. Acad. Sci.* **111**, (2014).
- [31] Jain, V. & Seung, H. S. Natural image denoising with convolutional networks. *Adv. Neural Inf. Process. Syst. 21 - Proc. 2008 Conf.* 769–776 (2009).
- [32] Zhang, K., Zuo, W., Chen, Y., Meng, D. & Zhang, L. Beyond a Gaussian denoiser: Residual learning of deep CNN for image denoising. *IEEE Trans. Image Process.* **26**, 3142–3155 (2017).
- [33] Weigert, M. *et al.* Content-aware image restoration: pushing the limits of fluorescence microscopy. *Nat. Methods* **15**, 1090–1097 (2018).
- [34] Lehtinen, J. *et al.* Noise2Noise: Learning image restoration without clean data. *Proc. 35th Int. Conf. Mach. Learn.* PMLR **80**:2965–2974 (2018).
- [35] Hendriksen, A. A., Pelt, D. M. & Batenburg, K. J. Noise2Inverse: Self-supervised deep convolutional denoising for linear inverse problems in imaging. *IEEE Trans. Comp. Imag.* **6**, 1320–1335 (2020).
- [36] Krull, A., Buchholz, T. O. & Jug, F. Noise2void-Learning denoising from single noisy images. *Proc. IEEE/CVF Conf. Comput. Vis. Pattern Recognit.* 2124–2132 (2019).
- [37] Batson, J. & Royer, L. Noise2Self : Blind Denoising by Self-Supervision. *Proc. 36th Int. Conf. Mach. Learn.* PMLR **97**:523–533 (2019).
- [38] Hendriksen, A. A. *et al.* Deep denoising for multi-dimensional synchrotron X-ray tomography without high-quality reference data. *Sci. Rep.* **11**:11895 (2021).
- [39] Presland, M. R., Tallon, J. L., Buckley, R. G., Liu, R. S. & Flower, N. E. General trends in oxygen stoichiometry effects on T_c in Bi and Tl superconductors. *Physica C* **176**, 95–105 (1991).
- [40] Mao, X.-J., Shen, C. & Yang, Y.-B. Image Restoration Using Very Deep Convolutional Encoder-Decoder Networks with Symmetric Skip Connections. *Adv. Neural Inf. Process. Syst. 29 - Proc. 2016 Conf.* 2802–2810 (2016).

- [41] Ronneberger, O., Fischer, P., Brox & T. U-Net: Convolutional Networks for Biomedical Image Segmentation. In: International Conference on Medical Image Computing and Computer-Assisted Intervention. 234-241 (Springer 2015).
- [42] Hashimoto, M. *et al.* Doping evolution of the electronic structure in the single-layer cuprate $\text{Bi}_{2-x}\text{Sr}_{2-x}\text{La}_x\text{CuO}_{6+\delta}$: Comparison with other single-layer cuprates. *Phys. Rev. B*, **77**, 094516 (2008).
- [43] Zhong, Y. *et al.* Differentiated roles of Lifshitz transition on thermodynamics and superconductivity in $\text{La}_{2-x}\text{Sr}_x\text{CuO}_4$. *Proc. Natl. Acad. Sci.* **119**:32 (2022).
- [44] Berben, M. *et al.* Superconducting dome and pseudogap endpoint in Bi2201. *Phys. Rev. Mater.* **6**, 044804 (2022).
- [45] Putzke, C. *et al.* Reduced Hall carrier density in the overdoped strange metal regime of cuprate superconductors. *Nat. Phys.* **17**, 826–831 (2021).
- [46] Miao, H. *et al.* Charge density waves in cuprate superconductors beyond the critical doping. *npj Quantum Mater.* **6**:31 (2021).
- [47] Kurashima, K. *et al.* Development of Ferromagnetic Fluctuations in Heavily Overdoped $(\text{Bi,Pb})_2\text{Sr}_2\text{CuO}_{6+\delta}$ Copper Oxides. *Phys. Rev. Lett.* **121**, 57002 (2018).

5 Hydrodynamic Transport Description of the Strongly Correlated Electron System Sr_2RuO_4

In sufficiently strongly interacting and clean electron systems transport phenomena are determined by hydrodynamic effects in contrast to diffusion dominated transport due to disorder. Successful efforts in showing these hydrodynamic effects relied primarily on clean systems with extremely large disorder length scales¹⁻³. Here we take the opposite approach by focusing our attention on a system with a short interaction length scale, i.e. a strongly interacting system, which is still clean enough to show hydrodynamic transport. Built on a previous result² we propose an experiment to observe nanoscale vortices in the strongly interacting superconductor Sr_2RuO_4 , spurred on by its cleanliness of both the bulk crystal and structured mesoscopic devices. Our calculations indicate the existence of a crossover from diffusive to hydrodynamic transport in Sr_2RuO_4 . The crossover exists over a wide range of disorder levels, and is robust against boundary effects. These results suggest a new probe into the strongly interacting normal state of Sr_2RuO_4 . Implementing the calculations for a cuprate strange metal system, proposed to be hydrodynamic through holography⁴, shows no hydrodynamic effects for realistic disorder levels, pointing towards the importance of disorder in strange metal systems.

5.1 Introduction

The emergence of complex electronic behavior is tied to the number of electrons and the strength of their mutual interactions⁵. It is therefore reasonable to expect that transport in mesoscopic devices is a prime candidate to observe such complex behavior due to large number of electrons in such a device while still being on the small length scales at which complexity often arises (see for example the emergence of superconducting puddles in Chapter 3). One telltale sign of complex or collective behavior in mesoscopic devices is the observation of hydrodynamic transport phenomena^{1,3,6-8}, as these phenomena rely on a conserved momentum of all electrons involved. Such behavior however is quickly drowned out by interactions which destroy this collective momentum, such as phonon interactions or impurity scattering, reducing transport physics to single particle physics.

Transport phenomena are thus split into several regimes, based on which of the above interactions are dominant. When impurity scattering, phonon scattering, or some other momentum non-conserving interaction dominates, transport is said to be in the diffusive or Ohmic regime (**Fig. 5.1a**). In this case a sense of collective electron momentum is destroyed over length- or time scales smaller than the system being probed. A lack of conserved momentum is also the case for the second transport regime, the ballistic regime (**Fig. 5.1b**). In this regime there are no interactions present, in the sense that the time it takes for an electron to engage in any interaction (either momentum conserving or non-conserving) is larger than the time it takes for an electron to cross the system. As such, while there are no interactions to destroy the conserved momentum, there are also no interactions to establish a collective momentum. This only happens in the last regime, the hydrodynamic regime (**Fig. 5.1c**). Here electron-electron interactions dominate, conserving the total momentum of the electron fluid, while momentum non-conserving processes are largely absent within the system. The fact that the total momentum is conserved allows for more complex transport behavior to exist, with phenomena often associated with everyday fluid dynamics such as laminar flow, vortex formation, and possibly even the onset of turbulence.

Examining which transport regime is relevant is most conveniently done by estimating the relevant length scales involved. These fall into three categories. First there is the size of the system or device, typically denoted L . Second, there

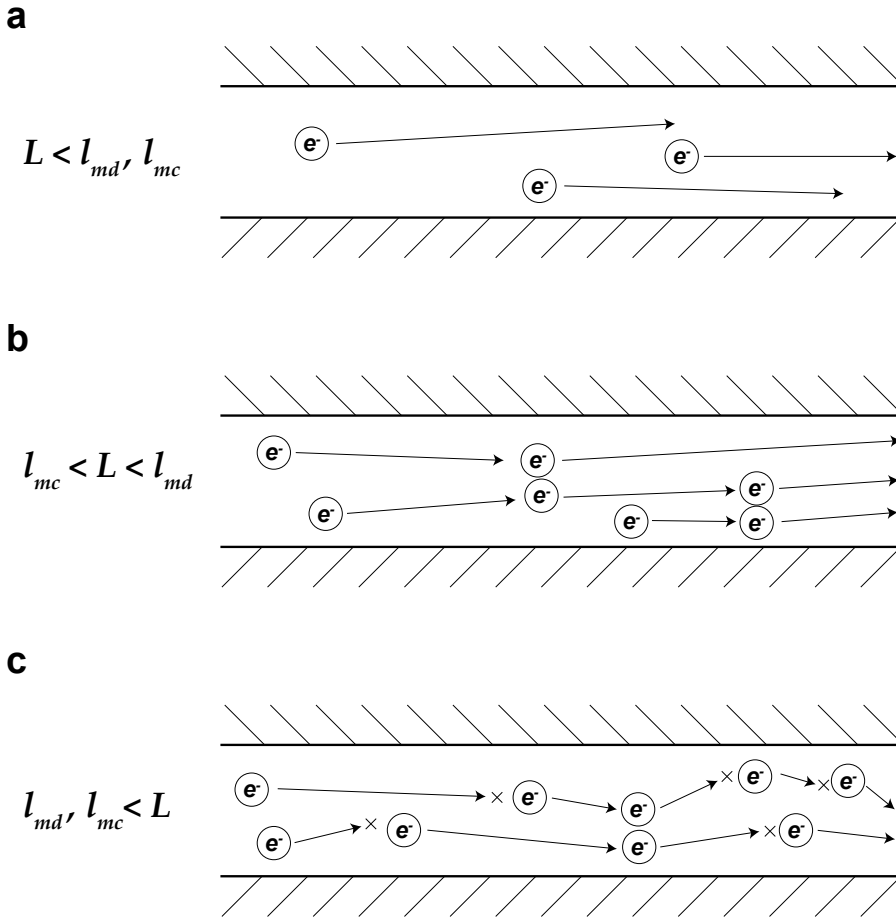


Figure 5.1: Transport regimes.

Schematics of the transport regime which are determined by the relative sizes of the length scales involved. **a)** When the system size L is the smallest length scale, transport is ballistic: electrons can cross the system without scattering. **b)** When the length scale for momentum conserving scattering l_{mc} is smallest, and the length scale for momentum diffusion l_{md} is largest the electron fluid as a whole carries a single conserved momentum and transport is governed by hydrodynamics. **c)** When l_{md} becomes smaller than L the momentum of the electron fluid can diffuse away during transport, losing its conserved nature. Transport is now diffusive.

is the length scale over which momentum of the electron fluid is lost to the lattice (or some other subsystem). This momentum diffusion length l_{md} bundles scattering events such as impurity scattering and electron-phonon scattering (although there are exceptions to the latter^{3,8}). Lastly, the momentum conserving length l_{mc} characterizes the processes conserving the electron momentum fluid, typically electron-electron interactions. The system size L is under control of the experimentalists, while l_{md} and l_{mc} depend on the materials involved and external factors such as temperature and applied pressure.

Observing hydrodynamic electron flow is no easy feat, primarily because the required combination of length scale is difficult to achieve. For hydrodynamic flow to occur l_{mc} needs to be the smallest length scale, while L needs to be at least on the order of l_{md} if not smaller:

$$l_{mc} < L < l_{md} \quad (5.1)$$

This way the electron fluid momentum can equilibrate within the device and without being disrupted by momentum diffusion.

First attempts and successes of observing hydrodynamic flow were achieved using semiconducting systems, such as GaAs and graphene^{1,2,9}. The main advantage of these systems is that l_{md} can be made quite large (several microns). This way, $l_{mc} < l_{md}$ is easier to guarantee even with very little electron-electron interactions, as is the case for these semiconducting systems. Furthermore, with modern lithography tools it is possible to make devices of the right shape and dimensions out of these materials to show signatures of hydrodynamic flow. Indeed, in such devices scientists have observed a unique temperature dependence of the resistivity called the Gurzhi effect¹⁰, the formation of backflow vortices^{2,11,12}, Poiseuille flow^{8,13,14}, and distinct effects of the device geometry on transport¹⁵⁻¹⁷.

More recently, the hunt for hydrodynamic electron behavior has shifted to more complex (semi-)metallic systems, such as PdCoO_2 , WP_2 , and WTe_2 ^{3,6,8}. Their mean free paths, while still remarkably long, are significantly shorter than those of the semiconducting systems mentioned above. Instead, their stronger electron-electron interactions, and therefore shorter l_{mc} , enable hydrodynamic flow. In the case of PdCoO_2 , being an oxide system, an additional challenge is to structure the devices while preserving their l_{md} . Nevertheless, observations of hydrodynamic flow have offered interesting windows into these systems, in particular the observation of phonon drag in WTe_2 ⁸.

The endpoint for the move towards increasingly strongly correlated systems is transport in strange metal systems. In these systems it is widely believed that the quasi-particles that would otherwise constitute electrical flow are no longer present due to the exceedingly large electron-electron interactions¹⁸⁻²⁰. As such, any definitive theory on the nature of these systems, and transport therein, is still lacking. One proposal inspired by string theory called AdS/CFT posits on general grounds that transport is of hydrodynamic nature with an extremely low viscosity^{4,21}. Observing such flow would present a major step forwards in understanding strange metal systems.

In this chapter we present a stepping stone towards hydrodynamic experiments in strange metal systems by proposing and examining experiments in the normal state Fermi liquid of Sr_2RuO_4 . We believe that hydrodynamic flow is observable in this state due to a unique combination of lengthscales. Firstly, the normal state, albeit a Fermi liquid, is a strongly correlated one. This is evidenced by transport properties such as the strongly enhanced effective mass²²⁻²⁴ or the recently observed nematic behavior²⁵. Secondly, the mean free path l_{md} can reach up to $1\mu\text{m}$, remarkably long for an oxide superconductor. We will examine several device designs which can give clear evidence of hydrodynamic flow, and we will calculate the expected signatures in experiments. Finally, we will take a closer look at what such an experiment would look like for a strange metal system.

5.2 Sr_2RuO_4 as a Hydrodynamic System: the Relevant Length Scales

Sr_2RuO_4 is perhaps best known for its highly unconventional superconducting state emerging below a T_c of 1.5K. While we focus mainly on the normal state rather than the superconducting state (reviews into the superconductivity of Sr_2RuO_4 can be found here²⁶⁻²⁸), one aspect is worth pointing out. The superconducting state is highly sensitive to disorder due to its unusual pairing symmetry (the exact pairing symmetry is still an ongoing debate²⁸). This mainly shows as a reduction of T_c for more disordered crystals. In fact, there is a clear relation between T_c and the residual resistivity ρ_0 , which serves as a proxy for the amount of disorder. The T_c is thus a useful diagnostic tool to determine sample quality. Samples with a T_c around 1.5K have a mean

free path (extracted from ρ_0) of around $1\mu\text{m}$. It is this extremely long mean free path which motivates the choice of Sr_2RuO_4 as a candidate for showing hydrodynamic transport behavior.

The first of the relevant length scales, or time scales which appear more naturally in the Navier-Stokes equations, are most easily calculated from the resistivity $\rho(T)$. As Sr_2RuO_4 is a quasi-2D system, with resistivity anisotropies ranging from 10^2 to 10^3 ^{24,26,29}, we can use the following relation between the residual resistivity and a scattering time from Boltzmann transport²⁹:

$$\rho(T) = \frac{2\pi\hbar\delta}{e^2} \frac{1}{\sum_i k_{F,i} v_{F,i} \tau_i(T)} \quad (5.2)$$

Where δ is the distance between the RuO planes and e is the electron charge. Sr_2RuO_4 is a multiband system, with three bands called the α, β , and γ bands, so the summation runs over the Fermi vector k_F and Fermi velocity v_F of each of the bands, and in principle we also need to take into account that the scattering time can differ between the bands. For the latter, we will assume that the scattering time is independent of the band index, and treat this as an effective scattering time for the whole system:

$$\tau(T) = \frac{2\pi\hbar\delta}{e^2} \frac{1}{\rho(T) \sum_i k_{F,i} v_{F,i}} \quad (5.3)$$

The Fermi vectors and velocities are readily available from literature^{22,23,30}, as is the interplanar distance³¹. It turns out that the Fermi velocities of the three bands are roughly similar, so we can calculate a length from the scattering time by simply using an average Fermi velocity:

$$l(T) = v_F \tau(T) \quad (5.4)$$

To get a sense of the size of the device needed to observe hydrodynamic transport, we look at two different scattering processes: impurity scattering and electron-electron scattering. These two are the only relevant ones, as the low temperature resistivity behavior is purely quadratic in T ²⁹:

$$\rho(T) = \rho_0 + AT^2 \quad (5.5)$$

At low enough temperatures impurity scattering dominates the resistivity, as this is the only process which is temperature independent. As such, the

impurity length scale l_{md} is calculated using the residual resistivity ρ_0 by extrapolating the resistivity to $T = 0K$. High quality Sr₂RuO₄ crystals can have a ρ_0 as low as $0.1\mu\Omega\text{ cm}$ ^{24,32}, which using the formulas above yield a length scale of $l_{md} = 960\text{nm}$.

The electron-electron scattering length l_{mc} is extracted from the T^2 term of the total resistivity by simply plugging in AT^2 into equation 5.3. Using a value for A of $7.3\text{ n}\Omega\text{ cm}/\text{K}^2$ ³³ we find an electron-electron scattering length of $l_{mc} = 60\text{ nm}$ at a temperature of 15K (see Fig. 5.2a). Note that this length scale has a T^2 temperature dependence, meaning this length diverges towards $T=0$. In order to observe hydrodynamic effects not only is it needed that $L < l_{md}$ but also $l_{mc} < L$. The former will be the main reason behind the size of the geometry, while the latter will determine the temperature window of the experiment. For a size of a few hundred nm, a temperature of around 15K will satisfy both conditions.

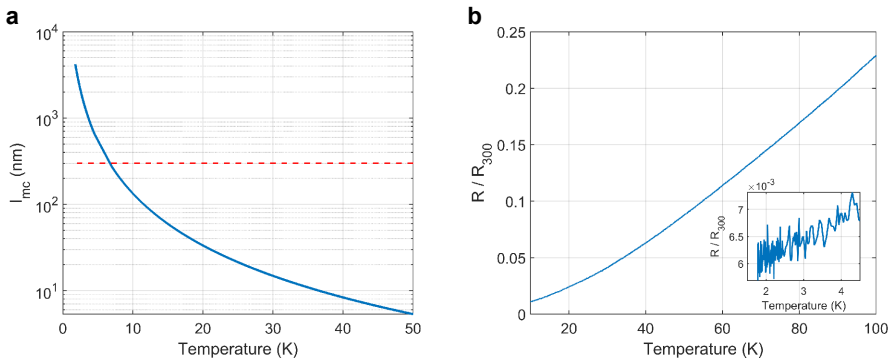


Figure 5.2 Electron-electron length scale.

a) The temperature dependence of the electron-electron scattering length scale associated with momentum conservation, calculated using the T^2 coefficient and Fermi momenta and velocities given in the main text. The red dashed lines indicates the device width of 300nm. When l_{mc} exceeds the device width, which occurs at 6.7K here, transport crosses over to the ballistic regime. **b)** The resistance data used for a FIB-structured Sr₂RuO₄ device used in this chapter to estimate the total scattering time τ . The resistance is normalized to the room temperature value R_{300} . Source: Remko Fermin, private communication.

5.3 Hydrodynamic Transport Simulations

5.3.1 Momentum Diffusion in the Navier-Stokes Equation

A more precise value for both these quantities, the geometry size and the appropriate temperature window, can be given first by examining the Navier-Stokes equations appropriate for electron flow, and solving the numerically for the envisioned device geometry. As we will see, the earlier estimates turn out to be fairly accurate.

In general, the transport behavior will be some combination of hydrodynamic effects and regular Ohmic flow. As such, the Navier-Stokes equations dealing with hydrodynamic flow are modified in the following way^{2,12,17}:

$$\frac{\tau}{ne} (\mathbf{J} \cdot \nabla) \mathbf{J} + \frac{ne^2\tau}{m^*} \nabla \Phi - \nu \tau \nabla^2 \mathbf{J} + \mathbf{J} = 0 \quad (5.6)$$

Where n is the carrier density, e the electron charge, m^* the effective mass, ν the kinematic viscosity, and τ the total scattering time. The variables to solve the equations for are the current density $J(x,y)$ and the electrical potential $\Phi(x,y)$, where we use the quasi-2D nature of Sr_2RuO_4 to approximate as being fully 2D. The addition of the final term encodes the Ohmic behavior in our system. Furthermore, we are looking for steady-state solutions which reduces the continuity equation to:

$$\nabla \cdot \mathbf{J} = 0 \quad (5.7)$$

The carrier density is calculated by using 4 electrons per unit cell^{22,34} and the volume of said unit cell³¹, yielding a density of $n = 2.1 \cdot 10^{28} \text{ m}^{-3}$. For the effective mass m^* we will use an average of the effective mass of each band of $8.5 m_e$. The viscosity ν is related to the length scale l_{mc} through^{2,12,17}:

$$\nu = \frac{1}{4} v_F l_{mc} \quad (5.8)$$

Where we again use the averaged Fermi velocity v_F . At a temperature of 15K, ν is roughly $0.005 \text{ m}^2 \text{ s}^{-1}$. This quantity, together with the total scattering time,

is temperature dependent, and the relative sizes of the two will determine the type of electron flow in the device. The scattering time τ we will estimate from the total resistivity at the temperature of interest. For this we will use the resistance data below (see **Fig. 5.2b**). Note that we will use the full resistivity. The scattering time in equation 5.6 is introduced through the inclusion of resistivity via the Ohmic term. As such, this scattering time includes any process which contributes to the resistivity. Also it is interesting to note that for the resistivity the exponent of the temperature dependence goes down at higher temperatures^{29,34}. This is unusual as in regular metals electron-phonon coupling sets in at higher temperatures which as a T^5 dependence (below the Debye temperature which is above 400K for Sr_2RuO_4 ³⁵). The drop of the exponent is associated with the presence of a Van Hove singularity close to E_F in the γ band, which enhances scattering rates³⁶. How this enhancement fits into the momentum conserving versus momentum diffusing framework is unclear. Therefore we opt to overestimate the amount of momentum diffusion and use the total resistivity for the scattering time.

The data we use to calculate the total scattering time τ is resistance data, not resistivity data. We convert between the two by assuming a value for the residual resistivity ρ_0 and scale the finite resistivity according to the resistance data. This also means that ρ_0 is a free parameter of the simulations. We will use this to get a sense of the influence of disorder on the backflow.

Equation 5.6 features a new length scale as the coefficient of the Laplacian term:

$$D_\nu = \sqrt{\nu\tau} = \frac{1}{2} \sqrt{l_{mc}l_m d} \quad (5.9)$$

This length scale determines the size of the hydrodynamic effects. The size of the geometry needs to be large enough to accommodate this, while the size of the probes (the contacts used to measure the hydrodynamic effects) needs to be small enough to be sensitive to this size. For the estimates given in section 5.2 D_ν is 120nm. This is thankfully compatible with the earlier estimate for the geometry size.

For the device geometry we propose to use the vicinity geometry, which was originally proposed and used to demonstrate the presence of hydrodynamic effects in graphene². In this setup the current is injected into the device through a small opening (see **Fig. 5.3a**). When the flow follows solely Ohm's law the current follows the edges of the device (**Fig. 5.3b**). When hydrodynamic effects

are present, a negative pressure directly next to the point of injection causes the formation of a backflow or whirlpool (**Fig. 5.3c**). As such, the current flows in a different direction depending on the transport regime, and the voltage across two contacts where the backflow can occur will have the opposite sign. The change of sign is the signature of crossing over from purely Ohmic behavior to hydrodynamic behavior.

Important in considering which geometry to use is considering what type of hydrodynamic flow is expected, codified in the Reynolds number:

$$RE = \frac{uL}{\nu} \quad (5.10)$$

For low Reynolds numbers (<1) the flow will be laminar, while for high Reynolds number (>1000) the flow will be dominated by turbulent effects, with a crossover or pre-turbulent regime for intermediate values. The fluid velocity is given by the drift velocity $u = J/ne$, on the order of 10ms^{-1} for a total current of 1mA in mesoscopic devices. The typical length scale is order 100nm , and using a viscosity of $\nu = 0.005\text{m}^2\text{s}^{-1}$ gives a Reynolds number of $RE = 2 \cdot 10^{-4}$. This means the flow will be deep in the laminar regime. As such, many effects associated with hydrodynamics will not occur in Sr_2RuO_4 . In particular, experiments relying on the merging several flow paths will not show the desired effects, as we demonstrate in Appendix 5A.

The geometry we use in our simulation has a main channel with a length L and a width H of $1\mu\text{m}$ and 300nm respectively. The current injector has a width W of 50nm , same for the voltage contacts used to measure the backflow voltage. Devices of Sr_2RuO_4 of such sizes can be fabricated using state-of-the-art techniques, by first exfoliating a bulk crystal into film flakes and then by creating the structure with focused ion beam milling (FIB), which has been shown to preserve the sample quality as measured by ratio of low temperature and high temperature resistance³⁷. Using thin flakes for the device, a necessity for using FIB, has the added benefit of increasing the current densities, which enhances the voltage signal. We will assume a flake thickness of 500nm for the conversion between current density and total current.

5.3.2 COMSOL Implementation

We numerically solve equation 5.6 for this geometry using the COMSOL Coefficient Form PDE interface. This package solves a general PDE of the

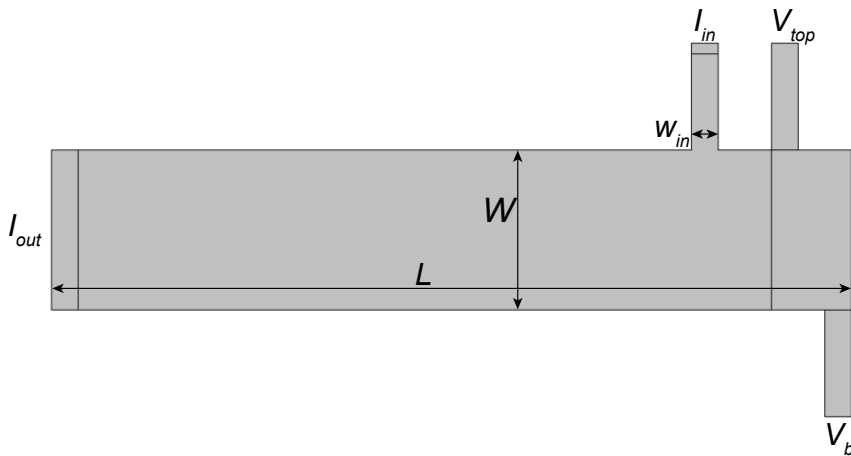
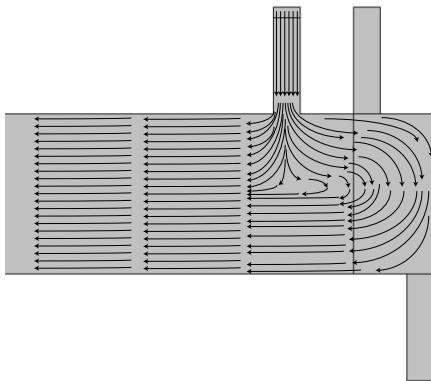
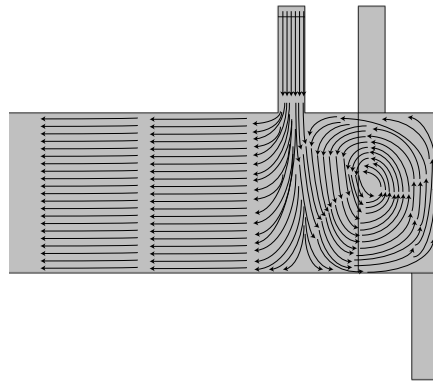
a**b****c**

Figure 5.3 The vicinity geometry.

a) The geometry of the device as used in the COMSOL simulations. The current enters the main device of width W and length L through the contact I_{in} of width w_{in} and flows out of the device at I_{out} . The backflow voltage is measured between the contacts V_{top} and V_{bot} . The sign of this voltage depends of the flow regime. In the diffusive or Ohmic regime shown schematically **b)** this voltage is positive as the current flows from V_{top} to V_{bot} . In the hydrodynamic regime depicted in **c)** the sign reverses as the backflow reverses direction due to the formation of negative pressure immediately next to I_{in} .

following form for a user defined geometry:

$$e_a \frac{\partial^2 u}{\partial t} + d_a \frac{\partial u}{\partial t} + \nabla \cdot (-c \nabla u - \alpha u + \gamma) + \beta \cdot \nabla u + a u = f \quad (5.11)$$

Where $u = (u_1, u_2, u_3)$ is the vector containing the independent variables, $(\sigma\Phi, J_x, J_y)$ in our case. This equation maps onto equations 5.6 and 5.7 by setting the coefficients as follows:

$$\begin{aligned} e_a = d_a = \alpha = \gamma = f = 0 \\ a = \begin{pmatrix} 0 & 0 & 0 \\ 0 & 1 & 0 \\ 0 & 0 & 1 \end{pmatrix} \\ c = \begin{pmatrix} 0 & 0 & 0 \\ 0 & \nu\tau & 0 \\ 0 & 0 & \nu\tau \end{pmatrix} \\ \beta = \begin{pmatrix} \begin{pmatrix} 0 \\ 0 \\ 1 \end{pmatrix} & \begin{pmatrix} 1 \\ 0 \\ 0 \end{pmatrix} & \begin{pmatrix} 0 \\ 1 \\ 0 \end{pmatrix} \\ \frac{\tau}{ne} \begin{pmatrix} u_2 \\ u_3 \end{pmatrix} & & \\ \begin{pmatrix} 0 \\ 1 \end{pmatrix} & \begin{pmatrix} 0 \\ 0 \end{pmatrix} & \frac{\tau}{ne} \begin{pmatrix} u_2 \\ u_3 \end{pmatrix} \end{pmatrix} \end{aligned} \quad (5.12)$$

The boundary conditions are set so that no current flows through the edges of the sample, and that the flow along the edges is allowed to slip, encoded via a slip-length:

$$\begin{aligned} \mathbf{J}_\perp &= 0 \\ \mathbf{J}_\parallel &= L_{slip} n \cdot \nabla \mathbf{J}_\parallel \end{aligned} \quad (5.13)$$

Where \mathbf{J}_\perp is the current perpendicular to the boundary, the current along the boundary, and n the vector normal to the boundary. The slip-length L_{slip} captures the interaction between the boundary and the fluid. Using a slip-length allows us to interpolate between two commonly used boundary conditions in fluid mechanics: no-slip condition ($L_{slip} = 0$) and no-stress condition (L_{slip} to infinity). This does come at the cost of another parameter

whose value is initially unknown. An estimate for L_{slip} can be given through the following argument³⁸: The slip-length should encode interactions with the boundary. Therefore for distances to the boundary smaller than the slip-length electrons are more likely to scatter off the boundary than off anything else (including other electrons). The estimate for the slip-length is then the smallest of the scattering length scales of the system, in our case the electron-electron scattering length. In our simulations we will use a temperature independent slip-length of $L_{\text{slip}} = 50\text{nm}$. At the current inlet and outlet we fix the potential, being 1mV at the inlet and 0mV at the outlet. Fixing the potential drop over the device turns out to give the least artifacts at the current inlet and outlet, though in principle it is also possible to fix the total current through the device and measure the potential drop between inlet and outlet.

The temperature dependence of the backflow voltage is solely determined by the temperature dependence of the viscosity ν and the scattering time τ . The temperature dependence of the former is T^2 via equations 5.4 & 5.8, and the temperature dependence of the latter is given by the resistance data used to extract the scattering time. For each temperature point we calculate these two quantities and use them to simulate the flow profile of the vicinity geometry. From this we calculate the backflow voltage between the two voltage contacts. Finally we express the result as a backflow resistance by dividing the backflow voltage by the total current injected. The reason to do this is that by fixing the voltage drop between the current contacts via the boundary conditions the total current can in principle vary as a function of temperature. This effect is separated out by using the backflow resistance as the final result. Then we repeat the simulations for various values of q_0 to examine the effects of disorder on the result.

5.4 Hydrodynamic Transport in Sr_2RuO_4

5.4.1 Negative Backflow Resistance

The results of the Sr_2RuO_4 simulations are shown in **Fig. 5.4** and **Fig. 5.5**. In **Fig. 5.4a** we show current distributions typical for the high temperature (**Fig. 5.4a**) and the low temperature (**Fig. 5.4b**) transport behaviour in the backflow section of the device. The distributions are qualitatively different, having

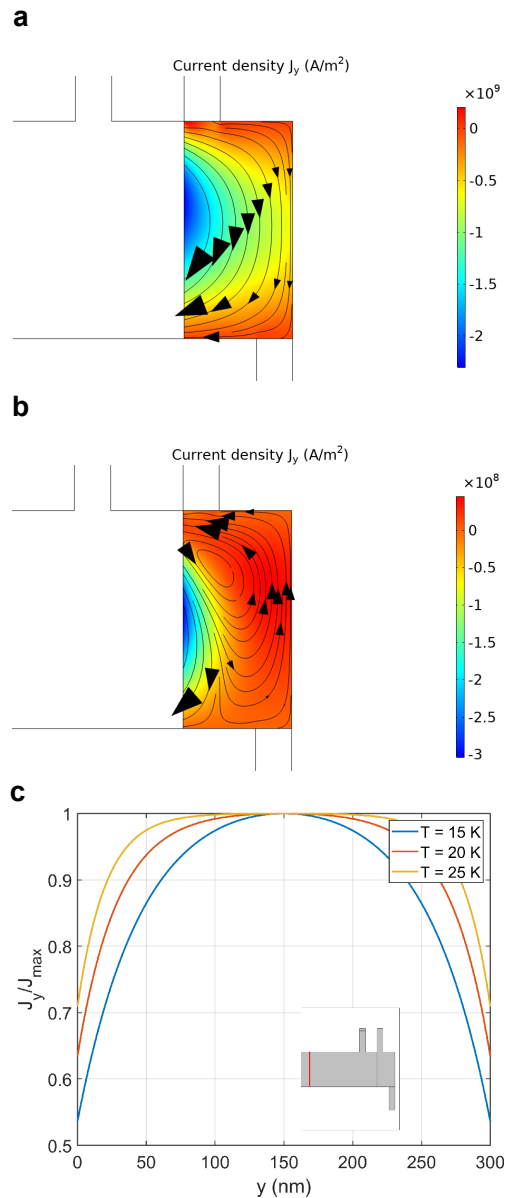


Figure 5.4 Sr_2RuO_4 Flow Profiles .

a,b) The flow profiles in the backflow section of the device at high temperature ($T=25\text{K}$) and low temperature ($T=5\text{K}$) resp. for $\rho_0 = 0.25\mu\Omega\text{cm}$. The appearance of a whirlpool at low temperature marks a qualitative difference between the two transport behaviors. **c)** The flow profiles for J_y across the main channel of the device as a function of temperature for the same ρ_0 . At low temperature the flow follows a roughly parabolic profile which flattens out as the temperature increases. The red line in the inset shows the line on the geometry along which J_y is measured.

an opposite flow direction in the two different regimes. The emergence of a whirlpool at low temperature is a sign of hydrodynamic dominated transport. The crossover between these two regimes is also apparent from the current distribution across the main channel of the device in Fig 5.4c. The high temperature calculation shows a nearly flat distribution, dropping near the edges of the device. As the temperature is lowered the distribution smoothly deforms towards the parabolic Poiseuille flow typical for hydrodynamic transport. The finite current at the boundaries is a result of the finite L_{slip} used in the simulations. The smooth evolution of the current distributions emphasizes that in general the transport is a mixture of both Ohmic and hydrodynamic effects, and any calculation needs to address them simultaneously.

The crossover from Ohmic to hydrodynamic transport, and the influence of disorder on the crossover, is apparent in both the forward and backflow resistances of the device shown in Fig. 5.5. In Fig. 5.5a we show the total or forward resistance of the device, calculated by measuring the total injected current and dividing by the 1mV potential drop fixed as boundary conditions. At low temperatures the resistance shows an upturn with decreasing temperature, departing from more usual metallic behavior at higher temperatures. This upturn is reminiscent of the Gurzhi effect¹⁰, one of the signs of hydrodynamic behavior.

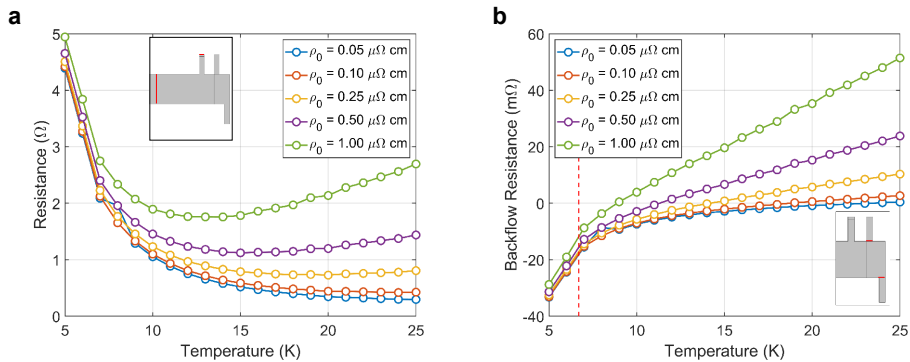


Figure 5.5 Sr_2RuO_4 Backflow resistance.

a) The total resistance of the device as a function of temperature for multiple values of ρ_0 , using the current flowing through the red lines shown in the inset. The upturn in the resistance is a sign of hydrodynamic effects¹⁰. **b)** The backflow resistance for the Sr_2RuO_4 vicinity geometry for various values of the residual resistance ρ_0 . A positive resistance is indicative of the diffusive regime, a negative resistance of hydrodynamic regime (see Fig. 5.3). The red line indicates the temperature below which ballistic effects set in^{2,39} (see Fig. 5.2a). The inset shows the vicinity geometry, with the red lines showing where the voltage is measured.

The crossover is perhaps most evident when looking at the backflow resistance shown in **Fig. 5.5b**. At higher temperature we find a positive backflow resistance, consistent with Ohmic transport. As the temperature drops, the backflow resistance eventually drops below zero, indicating a crossover into the hydrodynamic regime. The temperature at which the zero crossing occurs depends on the level of disorder in the device, encoded in ρ_0 . For clean samples ($\rho_0 = 0.1 \mu\Omega \text{ cm}$) the crossover occurs at $T=19\text{K}$, a temperature which drops to $T=9\text{K}$ for $\rho_0 = 1\mu\Omega \text{ cm}$. This is a surprisingly broad range of disorder levels at which the crossover should still be observable. While this wide margin seems to offer some leniency for the fabrication processes of the samples, some care should be taken with this result. At the top of this range ($\rho_0 = 1\mu\Omega \text{ cm}$) the T_c of bulk Sr_2RuO_4 has dropped to zero due to disorder²⁶. This dramatic change due to disorder warrants a more careful look into the appropriate transport description when l_{mc} roughly equals l_{md} .

When the temperature drops even further, the geometry size becomes the smallest length scale of the system. The flow becomes predominantly ballistic characterized by an upturn in the backflow resistance as the temperature is reduced^{2,39}. While the backflow resistance remains negative during this upturn, the system is in a quasi-ballistic regime where interaction still play a role³⁹. Fully ballistic transport sets in when the backflow resistance becomes positive. The physics of the crossover between hydrodynamic and ballistic, governed by the Knudsen number $Kn = l_{mc}/L$, is not captured in our transport description., though we can estimate when it occurs: $l_{mc} = L$ occurs at roughly 6.5K , marked by the red dashed line in **Fig. 5.5b**.

5.4.2 Boundary Effects: the Slip-length

There is still one free parameter left unexamined: the slip-length L_{slip} . To study its effect on the backflow voltage we fix the total scattering time to $\tau = 1 \cdot 10^{-10}$ s and the temperature to $T=15\text{K}$ so that we are in the hydrodynamic regime where we expect L_{slip} to have the largest effect. We then vary L_{slip} over a range of 1nm to $1\mu\text{m}$. **Fig. 5.6a,b** show the backflow patterns for both $L_{\text{slip}} = 1\text{nm}$ and $L_{\text{slip}} = 1\mu\text{m}$. We find that while the exact size and shape of the whirlpool does change with the slip length, its presence is remarkably stable against a changing L_{slip} . Over a range of at least 3 orders of magnitude we still expect a negative backflow resistance. To check that the slip length is indeed properly incorporated we show the flow distributions across the main channel in **Fig. 5.6c** and find that indeed the curvature of the distribution flattens and the

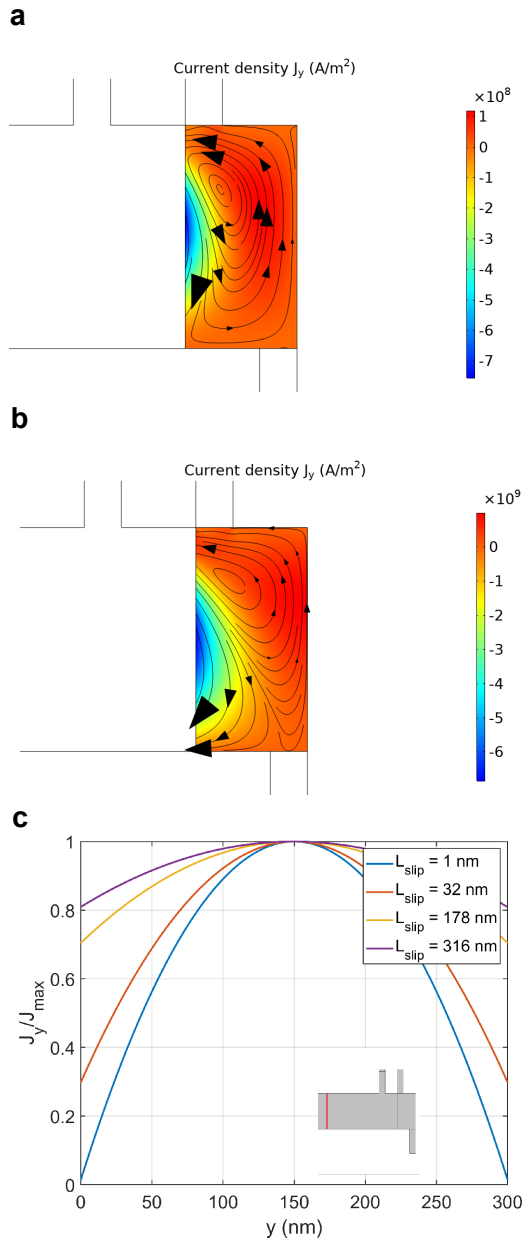


Figure 5.6 L_{slip} dependent Flow Profiles.

a,b) The flow patterns in the backflow section of the device for $L_{\text{slip}} = 1 \text{ nm}$ and $L_{\text{slip}} = 1 \mu\text{m}$ respectively. Despite the large difference in L_{slip} the flow direction remains stable. *c)* The flow profile across the main channel of the device for several values of L_{slip} . The flattening of the profile and the increasingly large current along the boundaries are consistent with a gradual change from no-slip conditions to no-stress conditions.

current at the boundary increases for larger L_{slip} , consistent with a change from no-slip boundary conditions ($L_{\text{slip}} = 0$) towards no-stress boundary conditions (L_{slip} towards infinity). The changes in the current distribution due to the slip length imply that the forward resistance does not have a similar stability as the backflow resistance seems to have.

These two predictions about the forward and backflow resistances are confirmed in **Fig. 5.7** where we show the effect of L_{slip} on the forward and backflow resistance. The total resistance shows a strong dependence of the slip length, as we expected from **Fig. 5.6c**. The drop in resistance as L_{slip} increases can be attributed to the decreased curvature of the flow profile, as the friction between adjacent fluid layers decreases when their relative velocity decreases. As anticipated from **Fig. 5.6a,b** the backflow resistance indeed remains negative over the full range of slip lengths. Not only that, its magnitude also remains nearly unchanged. The remarkable stability of the backflow resistance against the slip length improves the feasibility of a vicinity geometry experiment. Determining the slip length experimentally is quite difficult, especially when the flow profile cannot be directly measured. The fact that L_{slip} does not influence not only the sign but also the magnitude of the backflow resistance eliminates the need for an accurate determination of L_{slip} .

These result together indicate that hydrodynamic effects on the low temperature transport of Sr_2RuO_4 are not only possible in principle, but also fall within the technical abilities of modern experimental techniques. The approach we use

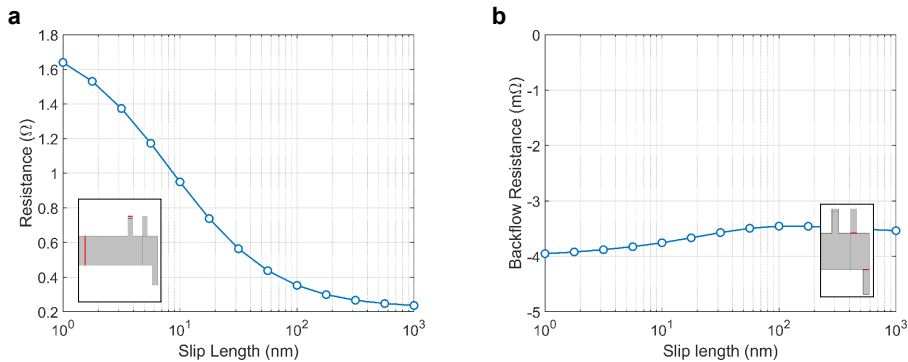


Figure 5.7 L_{slip} dependent resistances.

a) The total resistance of the device as a function of slip length. The resistance shows a strong dependence resulting from the changing current distribution as the slip length changes. **b)** The backflow resistance as a function of slip length. Remarkably, the backflow resistance remains nearly constant over a wide range of values for L_{slip} , despite the changes in the total resistance.

to calculate the backflow resistance also offer a degree of internal consistency with future experiments, as most important input parameters (such as the residual resistivity ρ_0 and the T^2 coefficient) can be extracted from a simple R-T curve of the crystal the device is created from. The use of COMSOL allows for more realistic simulations as the exact device geometry is more easily incorporated in the simulations. Since the existence of hydrodynamic effects rely heavily on the presence and the strength of electron correlations the observation of the effects described above offer a novel window into the correlated physics of Sr_2RuO_4 . It would also represent a step forwards for the use of hydrodynamics in the description and probing of correlated electron systems, for which other transport frameworks may fall short.

5.5 Towards Strange Metal Hydrodynamics

5.5.1 Transport Parameters

One example of such a system, and an extreme example of a correlated system, is a strange metal. This metallic phase, characterized by a linear-in-T resistivity for all temperatures, is most well known as the normal state of cuprate superconductors at optimal doping^{19,40}, although it is also found in other strongly correlated superconductors^{41–43}. One important aspect of the linear-in-T resistivity is that it violated the Mott-Ioffe-Regel limit, defined as the resistivity at which the mean free path is on the same order as the lattice constant⁴⁴. This violation seems to imply that the current is not carried by the quasi-particles we have come to expect from a Fermi liquid. This striking hypothesis is supported by ARPES experiments which find a clear lack of quasi-particles^{18,20}. How to deal with this absence of quasi-particles and how to describe the (transport) properties of such a system is one of the most profound mysteries of correlated electron physics.

One proposal makes use of the AdS/CFT correspondence^{4,21}. This mathematical machinery creates a bridge between certain models in general relativity (Anti-de Sitter spaces, the AdS part) and certain quantum theories (conformal field theories, the CFT part). The idea being that a hard problem on one side of the bridge translates to a more tractable problem on the other side. Then after solving the more tractable problem, the solution is translated

back. In particular, one can create metallic systems with this construction with properties reminiscent of strange metal behavior, particularly the linear-in-T resistivity. Additionally, transport in these systems is governed by the laws of hydrodynamics. In what follows we sketch what an experiment using the vicinity geometry would look like for a strange metal system with properties deriving from the AdS/CFT correspondence. We will follow the review ref⁴ when determining the relevant hydrodynamic system parameters.

A core concept of the AdS/CFT strange metal is minimal viscosity. Metals in this phase have a very particular relation between their dynamic viscosity η and their entropy density s :

$$\frac{\eta}{s} = A \frac{\hbar}{k_b T} \quad (5.14)$$

Where A is some numerical prefactor, equal to $1/4\pi$ in the AdS/CFT setting, although real systems have a value closer to 1. The entropy density takes a Sommerfeld like form of

$$s = \frac{k_b^2 n T}{\mu} \quad (5.15)$$

with n the number density, and μ the chemical potential. This leads to the following expression for the kinematic viscosity ν which we will use in our simulations:

$$\nu = \frac{A \hbar k_b T}{m_e \mu} \quad (5.16)$$

Where we used the mass density $\rho = n m_e$ to convert the dynamic viscosity η to the kinematic viscosity ν . Plugging in the numbers, we find a viscosity of $\nu = 2 \cdot 10^{-7} \text{m}^2 \text{s}^{-1}$, using $\mu = 1 \text{eV}$ appropriate for optimally doped cuprates⁴⁵, 4 orders of magnitude lower than the Sr_2RuO_4 case! This also means that the Reynolds number RE is 4 orders of magnitude larger, meaning it is on the order of 1. This means that pre-turbulent phenomena might be a possibility.

There is a scattering time associated with the minimal viscosity under the name of Planckian dissipation:

$$\tau = A \frac{\hbar}{k_b T} \quad (5.17)$$

However, even a strange metal system is not immune to disorder scattering. In fact, the cuprates, perhaps the most well-known example of a strange metal system, is notorious for its high levels of disorder. The highest quality cuprate samples have a residual resistance of $\rho_0 = 1.5\mu\Omega\text{cm}$ in the case of $\text{La}_{2-x}\text{Sr}_x\text{CuO}_4$ ⁴⁶. This is remarkably low for a cuprate, but still an order of magnitude worse than Sr_2RuO_4 . Translating this to a scattering time, this corresponds to $\tau = 1.8 \cdot 10^{-12}\text{s}$.

5.5.2 Absence of Whirlpool Formation

In our simulations for the strange metal system, we will use the same geometry size as the Sr_2RuO_4 case, as this size is already pushing the limitations of modern FIB techniques. Unlike the Sr_2RuO_4 we will assume a temperature independent scattering time given by the residual resistivity ρ_0 , representing a more optimistic scenario compared to including Planckian dissipation into τ . Also unlike the previous simulations we no longer fix the potential drop over the device. Instead we fix the total current flowing through the device. As such we have better control over the Reynolds number during the simulations, and we can avoid accidentally entering the turbulent regime as a result of a sudden increase in the current due to a drop in the forward resistance when hydrodynamic effects take over. The drawback is that fixing the current through the device is more susceptible to artifacts in the current distribution, as can be seen in **Fig 5.8a**, where the flow through the main channel of the device is skewed to one side of the channel.

Using a value of $\nu = 1 \cdot 10^{-7}\text{m}^2\text{s}^{-1}$, $\tau = 1.8 \cdot 10^{-12}\text{s}$, and $L_{\text{slip}} = 50\text{nm}$, our simulation yields the flow distribution shown in **Fig. 5.8a**. This flow profile is consistent with Ohmic transport, meaning the higher levels of disorder has drowned out the effects of the minimal viscosity. To observe a sign of the minimal viscosity, we show the flow profile for $\tau = 1.8 \cdot 10^{-10}\text{s}$ and $\tau = 1.8 \cdot 10^{-9}\text{s}$ in **Fig. 5.8b,c**. In the former case the first signs of a whirlpool emerge, but it fails to encompass the entirety of the backflow section, meaning the backflow resistance is most likely still positive in this case. Only when the scattering time is increased higher does the whirlpool cover the full width of the geometry, and do we expect a negative backflow resistance. It is also only for these values of τ that we see the effects of minimal viscosity. The higher Reynolds numbers associated with this flow shows itself through the emergence of additional whirlpools on the left of the current injector. In this case it is worth considering adding additional voltage contacts on the left of the current injector to check whether these additional whirlpools indeed appear.

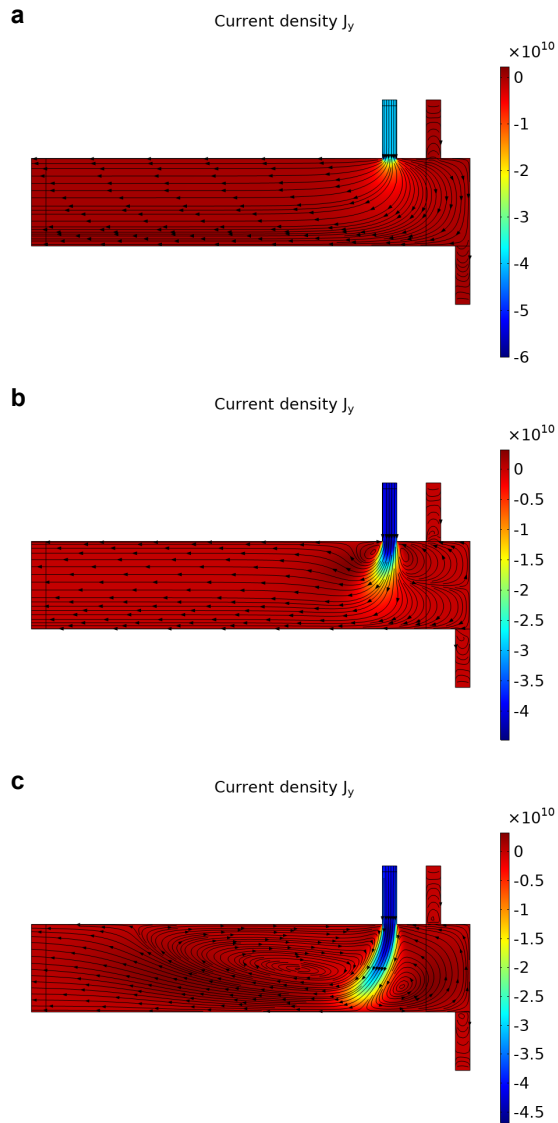


Figure 5.8 Minimal Viscosity Flow Profiles.

Flow profiles in the vicinity geometry using minimal viscosity and a scattering time of $\tau = 1.8 \cdot 10^{-12}$ s, $1.8 \cdot 10^{-9}$ s, and $1.8 \cdot 10^{-8}$ s (**a**, **b**, **c** respectively). The extremely low viscosity requires large scattering times for hydrodynamic effects to appear.

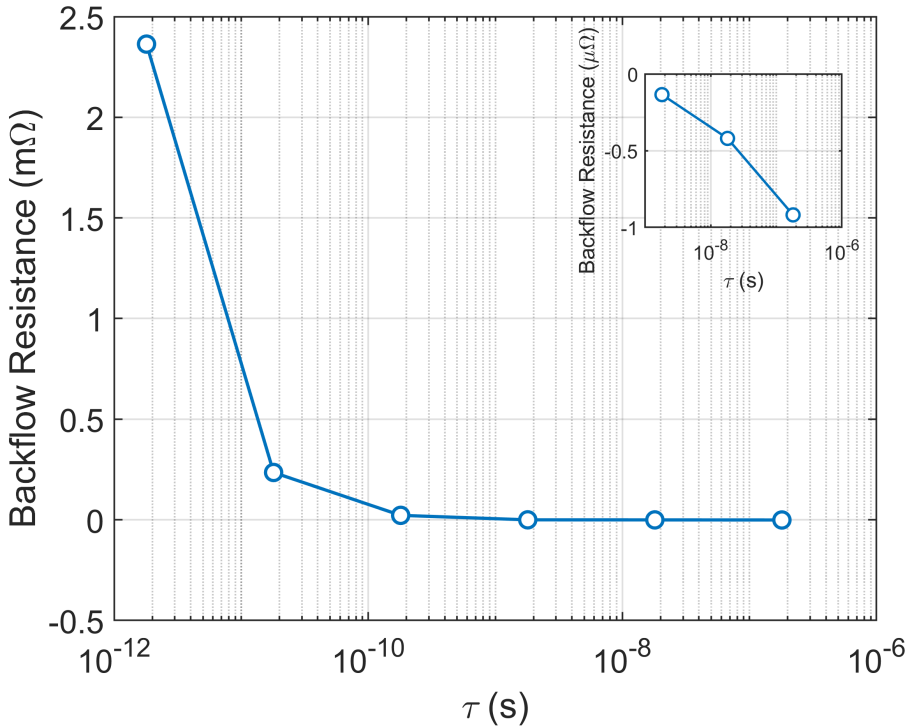


Figure 5.9 Minimal Viscosity Backflow Resistance.

The backflow resistance as a function of scattering time using a viscosity $\nu = 1 \cdot 10^{-7} \text{m}^2 \text{s}^{-1}$ in line with minimal viscosity. The inset shows the backflow resistance for the highest values of τ , where the resistance changes sign.

The difficulty of observing hydrodynamic flow for a minimal viscosity system is summarized in **Fig 5.9**, where we show the backflow resistance as a function of scattering time for the above simulations. A negative backflow resistance would require extremely large scattering times, unrealistic not only for cuprate systems but for any system. These difficulties can be traced back to the length scale D_ν over which hydrodynamic effects can be seen. For systems much larger than this, Ohmic effects dominate. For $\nu = 1 \cdot 10^{-7} \text{m}^2 \text{s}^{-1}$ and $\tau = 1.8 \cdot 10^{-12} \text{s}$, realistic values for a cuprate system, $D_\nu = 5 \text{\AA}$, barely two unit cells! Only when τ increases by several orders of magnitude does this length scale approach the system size. It turns out that the extremely low viscosity might actually be a drawback in a system that also includes disorder. The linear temperature dependence of ν is too slow to make much of a difference, even when ignoring any detrimental temperature dependence of τ .

These results stress the importance of disorder in strange metal systems. Taking a straight forward approach to the role of disorder, similar to the approach for Fermi liquid systems, we find that hydrodynamic effects get washed out by disorder for a strange metal system. A more detailed examination of disorder in holography or other strange metal descriptions will need to determine whether such a straight-forward approach is warranted. Despite this negative result, we still believe it is worth performing such an experiment for a strange metal system. Given how little is known for certain about these system, any new information is valuable even if it is the absence of hydrodynamic transport. We also remark that this result is a consequence of the proposed minimal viscosity. In the hypothetical case that the viscosity of a strange metal is more in line with that of a Fermi liquid (such as Sr_2RuO_4) hydrodynamic transport would become more likely.

5A Appendix

The low Reynolds number for a Fermi liquid ($RE \sim 1 \cdot 10^{-4}$, see Chapter 5.3) limits the design space for experiments attempting to show hydrodynamic transport. An illustrative example is the Tesla valve⁴⁷(**Fig. 5A.1**), a one-way valve without any moving parts. The operating principle relies on splitting off the flow into a main channel and an arced section, and merging again the two parts of the flow. How much flow is split off and how the two flows merge is fully controlled by the exact design. When properly designed, the Tesla valve has an easy axis, where only a small part is split off and the flow resistance is low (**Fig. 5A.1a**), and a hard axis, where more flow is split off and the flow resistance is higher (**Fig. 5A.1b**). However as we demonstrate this design is unsuitable for the demonstration of hydrodynamic transport in Fermi liquids, as it relies on higher Reynolds numbers.

To do so we will simulate the liquid flow through a nm sized Tesla valve. We will use a viscosity typical of $\nu = 0.005 \text{m}^2\text{s}^{-1}$ typical for Sr_2RuO_4 and vary the Reynolds number by varying the flow velocity. We will only simulate hydrodynamic behavior, meaning we will omit the last term of eq. 5.6 from the simulations. This allows us to use the standard COMSOL hydrodynamics package, speeding up the calculation drastically. We will pick the size of the Tesla valve such that inequality 5.1 is still satisfied, despite momentum diffusion being absent from the simulation. The width of the Tesla valve we

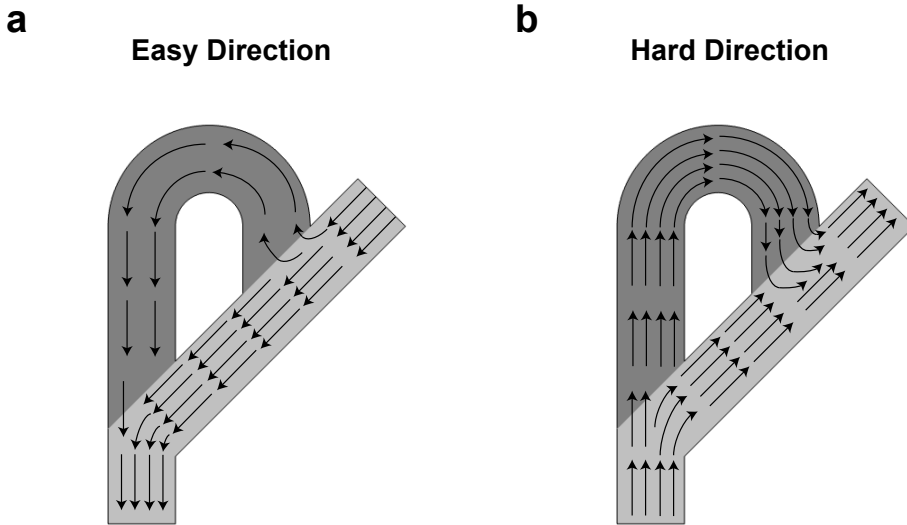


Figure 5A.1 Tesla Valve Geometry.

Sketch of the Tesla valve geometry and the flow along the easy (a) and the hard (b) flow direction. The difference in split and subsequent merger of flow between the two directions result in a different resistance between the two.

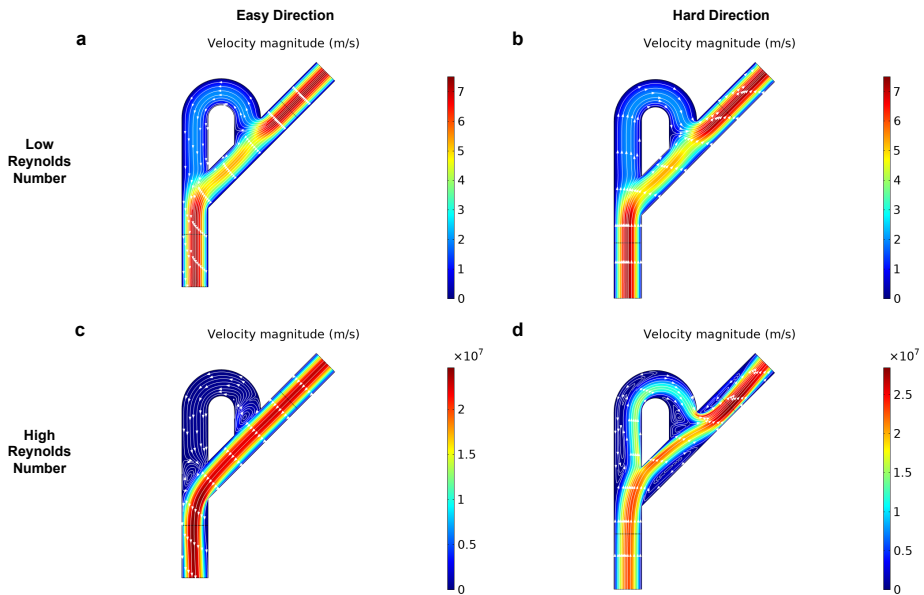


Figure 5A.2 Tesla Valve Flow Profiles.

Flow profiles through the Tesla valve for the easy (a,c) and hard (b,d) directions for $RE = 1 \cdot 10^{-4}$ (a,b) and $RE = 316$ (c,d). Only for the higher RE does the proposed diode function occur.

set to be 100nm. The length of the loop arm is 200nm, and the loop itself has an inner radius of 50nm. The flow velocity will range from roughly $u = 10\text{ms}^{-1}$ ($RE \sim 1 \cdot 10^{-4}$) to $u = 1 \cdot 10^7\text{ms}^{-1}$ ($RE \sim 1 \cdot 10^2$).

In **Fig. 5A.2** we show the results for these simulations for flow in the easy and hard direction for both low Reynolds number ($RE = 1 \cdot 10^{-4}$, **Fig. 5A.2 a,b**) and high Reynolds number ($RE = 316$, **Fig. 5A.2 c,d**). We find that in the low RE case the flow profiles in the easy and hard direction look very similar, meaning that their associated flow resistances are also very similar. This implies that in this case the Tesla valve does not act as a diode as it was designed to do. The case of high RE is quite different. Here, the flow profiles show large differences between the two flow directions. This can be attributed to the formation of whirlpools at the points where the flow is split off and merged. The size of the whirlpools depend significantly on the overall flow direction. As such we can expect the Tesla valve to function as a diode in this regime.

We can put the expectations about diode function on more solid ground by quantifying the flow resistance for each calculated flow profile. This can be done by using¹⁷

$$R_\nu = \frac{\nu \rho d}{2I^2} \int \sum_{i=1}^2 \sum_{j=1}^2 \left(\frac{\partial v_j}{\partial x_i} + \frac{\partial v_i}{\partial x_j} \right)^2 d^2x \quad (5A.1)$$

Where ν is the kinematic viscosity, ρ the fluid mass density, d the device thickness, and I the total current flowing through the device. The dependence of the exact flow profile is captured by taking the integral running over the full geometry of the derivatives of the fluid velocity $v_{x,y}$ with respect to the spatial coordinates x,y . We can use this expression to define a measure of how well the Tesla valve acts as a diode, the diodicity:

$$D = \frac{R_{\nu,hard}}{R_{\nu,easy}} \quad (5A.2)$$

This quantity solely depends on the shape of the fluid profiles, as all the prefactors to the integral in eq 5A.1 cancel out (the total current we keep the same when switching between easy and hard flow axis). A diodicity of $D = 1$ means there is no difference between the flow directions, and the valve does not work, while $D > 1$ means the Tesla valve works as intended. For each Reynold number we simulate we calculate the diodicity D , and track its evolution as a function of Reynolds number. The results are shown in **Fig.**

5A.3. We find that at low Reynolds numbers $D = 1$, as we anticipated from **Fig. 5A.2 a,b**. Only at roughly $RE = 20$ does the diodicity deviate from 1, reaching a value of 2.14 for $Re = 316$, the flow shown in **Fig. 5A.2 c,d**.

From this we conclude that the Tesla valve only works for moderate Reynolds number >10 . The space to change the Reynolds number for a Fermi liquid system is only limited, meaning this geometry design is unsuitable for Sr_2RuO_4 systems. The limited space is a result of all three components of the Reynolds number being subject to limitations. The system size L is limited by having to satisfy inequality 5.1, typically meaning there is at most 1 order of magnitude design space. The fluid viscosity ν is a system property whose temperature dependence is of little help as there is only a limited temperature range over which hydrodynamic flow is present. This leaves the fluid velocity v , given by the current through the device. A fluid velocity of roughly 10ms^{-1} ($RE \sim 1 \cdot 10^{-4}$)

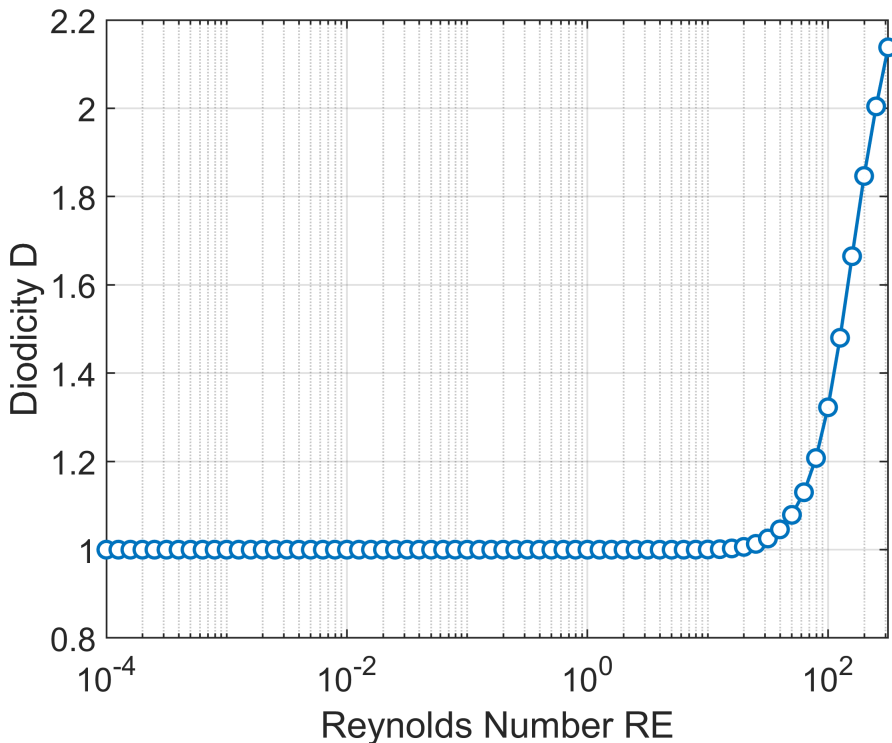


Figure 5A.3 Diodicity.

Diodicity D of the Tesla valve as a function of the Reynolds number RE . The onset of diode functionality ($D > 1$) only occurs around $RE = 20$, much larger than the $RE = 10^{-4}$ typical for flow in a Fermi liquid system.

corresponds to a total current of roughly 1mA. This would have to increase by 4 order of magnitude to 10A to start seeing some sort of diode function, a current which a mesoscopic device will typically not survive.

This is exemplary for the limited design space for hydrodynamic experiments for Fermi liquid systems caused by an extremely low Reynolds number and little room to increase it. Hydrodynamic flow is most pronounced when whirlpools start to form, an effect unique to the hydrodynamic regime. These only start to appear generically at moderate Reynolds numbers. Deep in the laminar regime the geometry has to be design specifically to allow for a whirlpool to form. The vicinity geometry achieves this by forcing the fluid to flow through a very narrow constriction, whereas the Tesla valve solely relies on the Reynolds number for whirlpool formation.

5

Interestingly, the minimal viscosity proposed for strange metals opens more design space at first glance. The extremely low viscosity means that the Reynolds number is automatically higher, already having $RE \sim 1$ for $v \sim 10\text{ms}^{-1}$, a velocity at which a Fermi liquid is still deep within the laminar flow regime. The effects of this comparatively high Reynolds number on the formation of whirlpools is clear by comparing **Fig. 5.4b** and **Fig 5.8c** This is however discounting the limits placed by the presence of momentum diffusion discussed in Chapter 5.4.

5.6 References

- [1] de Jong, M. J. M. & Molenkamp, L. W. Hydrodynamic electron flow in high-mobility wires. *Phys. Rev. B* **51**, 389–402 (1995).
- [2] Bandurin, D. A. *et al.* Negative local resistance caused by viscous electron backflow in graphene. *Science* **351**, 1055–1058 (2016).
- [3] Gooth, J. *et al.* Thermal and electrical signatures of a hydrodynamic electron fluid in tungsten diphosphide. *Nat. Commun.* **9**:4093 (2018).
- [4] Zaanen, J. Planckian dissipation, minimal viscosity and the transport in cuprate strange metals. *SciPost Phys.* **6**, 061 (2019).
- [5] Anderson, P. W. More is Different. *Science* **177**, 393–396 (1972).
- [6] Moll, P. J. W., Kushwaha, P., Nandi, N., Schmidt, B. & Mackenzie, A. P. Evidence for hydrodynamic electron flow in PdCoO_2 . *Science* **351**, 1061–1064 (2016).
- [7] Lucas, A. & Fong, K. C. Hydrodynamics of electrons in graphene. *J. Phys. Condens. Matter* **30**, 053001 (2018).

- [8] Vool, U. *et al.* Imaging phonon-mediated hydrodynamic flow in WTe_2 . *Nat. Phys.* **17**, 1216–1220 (2021).
- [9] Crossno, J. *et al.* Observation of the Dirac fluid and the breakdown of the Wiedemann-Franz law in graphene. *Science* **351**, 1058–1061 (2016).
- [10] Gurzhi, R. N. Hydrodynamic effects in solids at low temperature. *Sov. Phys. Usp.* **11**, 255 (1968).
- [11] Levitov, L. & Falkovich, G. Electron viscosity, current vortices and negative nonlocal resistance in graphene. *Nat. Phys.* **12**, 672–676 (2016).
- [12] Aharon-Steinberg, A. *et al.* Direct observation of vortices in an electron fluid. *Nature* **607**, 74–80 (2022).
- [13] Sulpizio, J. A. *et al.* Visualizing Poiseuille flow of hydrodynamic electrons. *Nature* **576**, 75–79 (2019).
- [14] Ku, M. J. H. *et al.* Imaging viscous flow of the Dirac fluid in graphene. *Nature* **583**, 537–541 (2020).
- [15] Krishna Kumar, R. *et al.* Superballistic flow of viscous electron fluid through graphene constrictions. *Nat. Phys.* **13**, 1182–1185 (2017).
- [16] Gusev, G. M., Jaroshevich, A. S., Levin, A. D., Kvon, Z. D. & Bakarov, A. K. Stokes flow around an obstacle in viscous two-dimensional electron liquid. *Sci. Rep.* **10**:7860 (2020).
- [17] Keser, A. C. *et al.* Geometric Control of Universal Hydrodynamic Flow in a Two-Dimensional Electron Fluid. *Phys. Rev. X* **11**, 031030 (2021).
- [18] Damascelli, A., Hussain, Z. & Shen, Z. X. Angle-resolved photoemission studies of the cuprate superconductors. *Rev. Mod. Phys.* **75**, 473–541 (2003).
- [19] Keimer, B., Kivelson, S. A., Norman, M. R., Uchida, S. & Zaanen, J. From quantum matter to high-temperature superconductivity in copper oxides. *Nature* **518**, 179–186 (2015).
- [20] Chen, S. Di *et al.* Incoherent strange metal sharply bounded by a critical doping in Bi2212 . *Science* **366**, 1099–1102 (2019).
- [21] Hartnoll, S. A., Lucas, A. & Sachdev, S. Holographic quantum matter. *arXiv:1612.07324* (2016).
- [22] Mackenzie, A. P. *et al.* Quantum oscillations in the layered perovskite superconductor Sr_2RuO_4 . *Phys. Rev. Lett.* **76**, 3786 (1996).
- [23] Mackenzie, A. P. *et al.* The Fermi Surface Topography of Sr_2RuO_4 . *J. Phys. Soc. Japan* **67**, 385–388 (1998).
- [24] Bergemann, C., Mackenzie, A. P., Julian, S. R., Forsythe, D. & Ohmichi, E. Quasi-two-dimensional Fermi liquid properties of the unconventional superconductor Sr_2RuO_4 . *Adv. Phys.* **52**, 639–725 (2003).
- [25] Wu, J. *et al.* Electronic nematicity in Sr_2RuO_4 . *Proc. Natl. Acad. Sci.* **117**, 10654–10659 (2020).

- [26] Mackenzie, A. P. & Maeno, Y. The superconductivity of Sr_2RuO_4 and the physics of spin-triplet pairing. *Rev. Mod. Phys.* **75**, 657 (2003).
- [27] Kallin, C. Chiral p-wave order in Sr_2RuO_4 . *Rep. Prog. Phys.* **75**, 042501 (2012).
- [28] Mackenzie, A. P., Scaffidi, T., Hicks, C. W. & Maeno, Y. Even odder after twenty-three years: The superconducting order parameter puzzle of Sr_2RuO_4 . *npj Quantum Mater.* **2**:40 (2017).
- [29] Hussey, N., Mackenzie, A., Cooper, J., Maeno, Y. & Nishizaki, S. Normal-state magnetoresistance of Sr_2RuO_4 . *Phys. Rev. B.* **57**, 5505 (1998).
- [30] Bergemann, C., Julian, S. R., Mackenzie, A. P., Nishi Zaki, S. & Maeno, Y. Detailed topography of the fermi surface of Sr_2RuO_4 . *Phys. Rev. Lett.* **84**, 2662 (2000).
- [31] Gardner, J. S., Balakrishnan, G. & Paul, D. M. Neutron powder diffraction studies of Sr_2RuO_4 and SrRuO_3 . *Physica C* **252**, 303–307 (1995).
- [32] Mackenzie, A. P. *et al.* Extremely Strong Dependence of Superconductivity on Disorder in Sr_2RuO_4 . *Phys. Rev. Lett.* **80**, 161 (1998).
- [33] Maeno, Y. *et al.* Two-Dimensional Fermi Liquid Behavior of the Superconductor Sr_2RuO_4 . *J. Phys. Soc. Japan* **66**, 1405–1408 (1997).
- [34] Maeno, Y., Nishizaki, S., Yoshida, K., Ikeda, S. & Fujita, T. Normal-State and Superconducting Properties of Sr_2RuO_4 . *J. Low Temp. Phys.* **105**, 1577–1586 (1996).
- [35] Paglione, J. *et al.* Elastic tensor of Sr_2RuO_4 . *Phys. Rev. B* **65**, 220506(R) (2002).
- [36] Barber, M. E., Gibbs, A. S., Maeno, Y., Mackenzie, A. P. & Hicks, C. W. Resistivity in the Vicinity of a van Hove Singularity: Sr_2RuO_4 under Uniaxial Pressure. *Phys. Rev. Lett.* **120**, 076602 (2018).
- [37] Yasui, Y. *et al.* Spontaneous emergence of Josephson junctions in homogeneous rings of single-crystal Sr_2RuO_4 . *npj Quantum Mater.* **5**:21 (2020).
- [38] Squires, T. M. & Quake, S. R. Microfluidics: Fluid physics at the nanoliter scale. *Rev. Mod. Phys.* **77**, 977 (2005).
- [39] Bandurin, D. A. *et al.* Fluidity onset in graphene. *Nat. Commun.* **9**:4533 (2018).
- [40] Cooper, R. A. *et al.* Anomalous Criticality in the Electrical Resistivity of $\text{La}_{2-x}\text{Sr}_x\text{CuO}_4$. *Science* **323**, 603 (2009).
- [41] Custers, J. *et al.* The break-up of heavy electrons at a quantum critical point. *Nature* **424**, 524–527 (2003).
- [42] Grigera, S. A. Magnetic Field-Tuned Quantum Criticality in the Metallic Ruthenate $\text{Sr}_3\text{Ru}_2\text{O}_7$. *Science* **294**, 329–332 (2001).
- [43] Hashimoto, K. *et al.* A sharp peak of the zero-temperature penetration depth at optimal composition in $\text{BaFe}_2(\text{As}_{1-x}\text{P}_x)_2$. *Science* **336**, 1554–1557 (2012).
- [44] Hussey, N. E., Buhot, J. & Licciardello, S. A tale of two metals: Contrasting criticalities in the pnictides and hole-doped cuprates. *Rep. Prog. Phys.* **81**, 052501 (2018).

- [45] Loram, J. W., Mirza, K. A., Cooper, J. R. & Liang, W. Y. Electronic specific Heat of $\text{YBa}_2\text{Cu}_3\text{O}_{6+x}$ from 1.8 to 300 K. *Phys. Rev. Lett.* **71**, 1740 (1993).
- [46] Giraldo-Gallo, P. *et al.* Scale-invariant magnetoresistance in a cuprate superconductor. *Science* **361**, 479–481 (2018).
- [47] Tesla, N. Valvular Conduit. *US Patent 1329559*. Feb. 1920

Summary

A common strategy to explain the electronic properties of most everyday materials is the reductionist approach. This strategy involves identifying and thoroughly studying the smallest building block of the system, electrons in this case, and scaling the properties of the building blocks to the size of the full system. Crucially, how the building blocks fit together, or how the electrons interact with each other, is ignored. The application of this approach works remarkably well to explain the properties of most materials, despite the strong Coulomb repulsion that electrons should experience between each other.

Modern research is increasingly focused on a class of materials called strongly correlated electron systems whose properties the reductionist approach struggles to explain. In these systems the Coulomb interaction between electrons is a crucial factor in determining the properties of the material. One of the consequences is that the number of electrons present in the system can play a major role in ways that go beyond the reductionist approach. One of the most notorious examples of such a system are the copper-oxide high-temperature superconductors. These superconductors emerge from an insulating system where the Coulomb interaction freezes the electrons in place. A slight change in the number of electrons in this system leads to a number of unconventional electronic states, among which a superconducting state with the highest known critical temperature at ambient pressure. How this superconducting state forms and disappears again, and its relation to the strongly insulating parent state, has eluded physicists ever since its discovery, and remains a highly active field of research.

The nanometer length scale offers a unique window into strongly correlated systems. The electronic properties can vary on these relevant length scales, and the flow of electrons on such length scales can feature hydrodynamic phenomena not possible on larger scales. In this thesis we present our contribution to the field of strongly correlated electrons system by exploring exactly this nano-scale. We employ the technique of scanning tunneling microscopy (STM) which allows us to measure the local distribution of electrons, or local density of states, with subatomic precision. We also explore how electrons flow through a mesoscopic structure of a strongly correlated material.

In Chapter 2 we take a closer look at how we study correlated systems, by comparing three spectroscopic techniques. The three techniques in question, ARPES, STM, and quantum oscillations, all measure (aspects) of the bandstructure of a material. To see how these techniques compare we apply them to Sr_2RhO_4 , which acts as a model system, a metaphorical drosophila, of Fermi liquids. We measure the Fermi surface using ARPES and the quasi-particle interference (QPI) observed by STM, and compare this with the Fermi surface pocket sizes determined by quantum oscillations. The Fermi velocities determined by each of these techniques is given the same treatment, as are the quasi-particle lifetimes measured by ARPES and STM. In all of these cases we find that the three techniques are in agreement. This leads us to conclude that the disagreement between these measurement techniques that occurs in other strongly correlated systems is a reflection of their physics.

Next, we turn our attention to copper-oxide high-temperature superconductors, in particular the overdoped superconductors where the critical temperature decreases with increases doping. In Chapter 3 we measure the local density of states using STM of multiple samples covering a broad range of critical temperature, including a sample which is no longer superconducting due to the high doping level. This allows us to carefully study the disappearance of superconductivity in this material. We find that an increasingly large number of nanometer sized metallic regions emerge in the superconducting state as the critical temperature goes down. In particular we find superconducting regions in the sample that no longer superconducts on a macroscopic scale. We also find that the spectroscopic gap associated with superconductivity does not disappear through a reduction of the gap magnitude, but rather by acquiring an increasingly large density of states at the Fermi level, a filling of the gap. The breaking of Cooper pairs responsible for the gap filling is found to have a highly unusual relation with the gap magnitude. These observations combined lead to a picture of emergent granular superconductivity in the strongly overdoped copper-oxide superconductors governed by a pair breaking process which the most common theoretical approach fails to accurately describe.

In Chapter 4 we study the electronic structure in momentum space of the same copper-oxide superconductor samples by measuring the quasi-particle interference with STM. To increase the signal-to-noise ratio of our STM images we implement a machine learning algorithm for noise suppression. The use of self-supervised learning allows for effective noise reduction without the

large amounts of data necessary for more traditional supervised learning. Our QPI images of the overdoped copper-oxide superconductors reveal a full Fermi surface and rigid shift of the anti-nodal band as a function of doping. We note that different determinations of the exact doping level by various measurement techniques do not agree. We also observe the bending of the band due to superconducting gap and find an unusual feature near the gap edge associated with the presence of an additional ordered state. The presence of this feature of a broad doping range appears to be a poor fit with previous claims of charge density waves of ferromagnetic fluctuations in overdoped copper-oxide superconductors.

In Chapter 5 we move away from measurements of the electronic structure in either real or momentum space, and instead examine electrical transport in mesoscopic structures. On such a length scale the interactions between electrons can lead to transport phenomena typically associated with hydrodynamics, provided the disorder is not too strong. We argue that the strongly correlated unconventional superconductor Sr_2RuO_4 provides the right combination of strong interaction and low disorder to observe hydrodynamic behavior. Using modified Navier-Stokes equations to include a disorder term we simulate the flow of electrons in Sr_2RuO_4 through a structure previously used to successfully demonstrate hydrodynamic behavior, and calculate the expected voltage drop over the device. We then do the same for the strange metal phase of copper-oxide superconductors using results from the holographic description of this phase. Using our framework for hydrodynamic transport in the presence of disorder, we find that the higher amounts of disorder compared to Sr_2RuO_4 and the extremely low viscosity this state is proposed to have make hydrodynamic behavior highly unlikely. Despite this result we argue that it is still worthwhile carrying out this experiment in copper-oxide superconductors, given the limited amount of available data on mesoscopic transport in these systems.

Samenvatting

Een veel voorkomende strategie om de elektronische eigenschappen van de meeste alledaagse materialen te verklaren is de reductionistische invalshoek. Deze strategie begint met het identificeren en grondig bestuderen van de kleinste bouwsteen van het systeem, elektronen in dit geval, om vervolgens de eigenschappen van die bouwsteen op te schalen naar de schaal van het gehele systeem. Cruciaal is dat hierbij wordt genegeerd hoe deze bouwstenen samen passen, hoe de elektronen onderling wisselwerken. Deze aanpak werkt verrassend goed in het beschrijven van de meeste materialen, ondanks de sterke Coulomb afstoting die elektronen tussen elkaar zouden moeten voelen.

Hedendaags onderzoek focust steeds meer op een groep materialen, genaamd sterk gecorreleerde elektron materialen, waarmee de reductionistische strategie steeds meer moeite heeft om die te verklaren. In zulke systemen is de Coulomb wisselwerking een cruciale factor in de eigenschappen van het materiaal. Een van de consequenties hiervan is dat het aantal elektronen in het systeem een belangrijke rol can spelen op manieren die voorbij gaan aan de reductionistische strategie. Een van de meest notoire voorbeelden hiervan zijn de koperoxide hogetemperatuursupergeleiders. Deze supergeleiders komen voort uit een isolerend systeem waar de Coulomb afstoting dusdanig sterk is dat de elektronen op hun plaats zijn vast gevoren. Een kleine verandering in het aantal elektronen in dit systeem veroorzaakt een verscheidenheid aan onconventionele elektronische toestanden, waaronder een supergeleidende toestand met de hoogst bekende kritische temperatuur bij omgevingsdruk. Hoe supergeleiding hier vormt en weer verdwijnt, en de relatie met het originele, sterk isolerend systeem, is een open vraag sinds de ontdekking van deze systemen die zeer actief onderzocht wordt.

De nanometer lengteschaal biedt een unieke blik op sterk gecorreleerde systemen. De elektronische eigenschappen kunnen sterkt variëren op deze schaal, en het vloeien van elektronen op deze schaal kan worden gekenmerkt door hydrodynamische fenomenen die niet mogelijk zijn op grotere lengteschalen. In dit proefschrift presenteren wij onze bijdrage aan het sterk gecorreleerde elektronsystemen vakgebied door precies deze nanoschaal te onderzoeken. Hiervoor maken wij gebruik van scanning tunneling microscopie (STM) die ons in staat stelt om de lokale verdeling van elektronen, of de lokale toestandsdichtheid, te meten met subatomaire precisie. Ook zullen

we onderzoeken hoe elektronen stromen door mesoscopische structuren van sterk gecorreleerde materialen.

In hoofdstuk 2 bestuderen we nader hoe we precies onderzoek doen aan sterk gecorreleerde systemen door drie spectroscopische technieken met elkaar te vergelijken. De drie technieken in kwestie, ARPES, STM, en kwantum oscillaties, meten ieder (aspecten) van de bandenstructuur van een materiaal. Om te zien hoe deze technieken vergelijken passen we ze ieder toe op Sr_2RhO_4 , een modelsysteem, een metaforische drosophila, voor Fermi vloeistoffen. We brengen het Fermi oppervlak in kaart met behulp van zowel ARPES als quasideeltjes interferentiepatronen (QPI) waargenomen door STM, en vergelijken deze met de Fermi oppervlaktes bepaald aan de hand van kwantum oscillaties. De Fermi snelheden bepaald door deze drie technieken krijgen dezelfde behandeling, alsmede quasideeltjes vervaltijd bepaald door ARPES en STM. In al deze gevallen zijn de drie technieken in overeenkomst. Dit leidt ons tot de conclusie dat de discrepanties tussen deze technieken die zich voordoen voor andere sterk gecorreleerde systemen een reflectie zijn van de onderliggende fysica.

Vervolgens verleggen wij onze aandacht naar de koperoxide hogetemperatuur-supergeleiders, in het bijzonder de overgedoteerde supergeleiders voor welke de kritische temperatuur omlaag gaat bij hogere doteringsniveaus. In hoofdstuk 3 meten we de lokale toestandsdichtheid met STM voor verscheidene monsters die een breed bereik aan doteringsniveaus beslaan, inclusief een monster met een dusdanig veel gedoteerd dat hij niet meer supergeleidend is. Dit stelt ons in staat om nauwkeurig het afbreken van supergeleiding in dit materiaal te bestuderen. Wij observeren de formatie van steeds meer nanometer grote metallische regio's in de supergeleidende toestand wanneer de kritische temperatuur daalt. In het bijzonder zien we supergeleidende regio's in het monster dat niet meer supergeleidend is op een macroscopische schaal. Ook zien we dat het spectroscopische gat waar supergeleiding mee geassocieerd is niet verdwijnt door het sluiten van dat gat, maar door een toenemende toestandsdichtheid op het Fermi niveau, het dempen van dat gat. Het opbreken van de Cooperparen verantwoordelijk voor het dempen blijkt een zeer ongebruikelijke correlatie te hebben met de grootte van het supergeleidend gat. Deze waarnemingen vormen samen een beeld van een emergente granulaire supergeleider in de sterk overgedoteerde koperoxide supergeleiders waarin een paarbrendend proces bepalend is dat niet door de meest gangbare theoretische modellen kan worden gevat.

In hoofdstuk 4 bestuderen wij de elektronische structuur van dezelfde koperoxide supergeleiders in de momentumruimte door de interferentiepatronen van de quasideeltjes waar te nemen met STM. Om de signaal-ruisverhouding van onze STM beelden te verhogen implementeren we een machine learning algoritme om de ruis te onderdrukken. Het gebruik van een zelfsupervisie tijdens het trainen maakt het mogelijk om effectief de ruis te onderdrukken zonder de grote hoeveelheden aan data die de meer traditionele supervisie van machine learning nodig heeft. Onze QPI beelden van de overgedoteerde koperoxide supergeleiders laten een volledig Fermi oppervlak zien met een band bij de antinodi die rigide verschuift als functie van doteringsniveau. We merken op dat verschillende bepalingen van het exacte doteringsniveau door verschillende meetmethodes niet overeen komen. We zien ook dat de band nabij het Fermi niveau wordt omgebogen door het supergeleidend gat, en de aanwezigheid van een kenmerk die geassocieerd kan worden met een bijkomende geordende toestand. De aanwezigheid van dit kenmerk over een breed bereik van doteringsniveaus is in tegenspraak met eerdere claims van ladingsdichtheidsgolven of ferromagnetische fluctuaties in overgedoteerde koperoxide supergeleiders.

In hoofdstuk 5 nemen we afstand van metingen van de toestandsdichtheid, en bestuderen we in de plaats daarvan elektrisch transport door mesoscopische structuren. Op deze schaal kunnen de wisselwerkingen tussen de elektronen onderling leiden tot transportverschijnselen die typisch geassocieerd worden met hydrodynamica, ervan uitgaande dat de wanorde in het materiaal niet te groot is. We beargumenteren dat de sterk gecorreleerde onconventionele supergeleider Sr_2RuO_4 de juiste combinatie van sterke wisselwerking en weinig wanorde heeft om zulk hydrodynamisch gedrag te vertonen. Gebruik makend van de Navier-Stokes vergelijking aangepast om ook wanorde te beschrijven simuleren we het vloeien van elektronen door een Sr_2RuO_4 structuur wiens ontwerp eerder is toegepast om hydrodynamisch gedrag aan te tonen, en rekenen we het verwachte voltage verschil uit over de structuur. We herhalen dit proces voor de vreemde metaal toestand van de koperoxide supergeleiders gebruik makend van resultaten van een holografische omschrijving van die toestand. Het toepassen van ons model voor hydrodynamisch transport in combinatie met wanorde laat zien dat de sterkere aanwezigheid van wanorde in vergelijking met Sr_2RuO_4 in combinatie met de extreem lage viscositeit die de vreemde metalen hebben volgens de holografische omschrijving ertoe leiden dat hydrodynamische verschijnselen zeer onwaarschijnlijk zijn. Ondanks dit resultaat vinden we het nog steeds de moeite waard om zulk

soort experimenten te doen voor koperoxide supergeleiders, gegeven de beperkte hoeveelheid data beschikbaar voor mesoscopisch transport voor deze systemen.

Acknowledgements

No accomplishment is achieved alone, least of all a PhD. I am eternally grateful for all the people who made the work in this thesis possible and otherwise supported me over these years.

First of all I would like to thank my supervisor Milan Allan. Your keen insights and our discussions have provided me with invaluable teachings over the years. I would also like to thank Jan Aarts for keeping an eye out and for your experience, wisdom, and support.

I have had the pleasure of working together with amazing collaborators during my PhD. Firstly I would like to thank Felix Baumberger and Anna Tamai, who I got to know during my time as a MSc student with them, for the wonderful work we did on the Sr_2RhO_4 project. That project would also not have been possible without the indispensable insights of Robin Perry and Andrew Mackenzie. Our work on the cuprates would not have been possible without the strange metal consortium, which we had the pleasure to partake in. A special thanks goes to Jan Zaanen, Miguel Sulangi, Nigel Hussey, Steef Smit, Lewis Bawden, Erik van Heumen, Yingkai Huang, and Mark Golden for all the work we did together, for your thoughtful discussions, and your unparalleled knowledge of physics. The strange metal meetings discussing all the latest news and progress were truly inspirational.

I would also like to thank Sense-Jan van der Molen for our discussions and our work as the PhD platform together with Alessandra Silvestri, Thomas Schmidt, Celine Alkemade, Jeremy Ernst, Ludwig Hoffman, and Corné Koks. Special thanks also go out to Tjerk Oosterkamp for providing early guidance and embarking on the occasional musical adventure with me.

The research we do is simply impossible without the contributions of the support staff here in Leiden. The people of the FMD and the ELD with all the technical know-how, in particular Kees van Oosten, Gijbert Verdoes, Freek Groenewoud, and Hugo van Bohemen without whom the lab would crumble. I would also like to thank Wilfred van der Geest for providing us with liquid helium, even if it would mean overthrowing your schedule for us. Thanks go out to Ellie van Rijsewijk and Michelle Wijffe for your administrative support and the infinite patience you have shown me.

Life in the lab would not be possible without all the amazing members of the Allan lab. You have taught me all the lab skills I know, and were an endless source of laughs, fun, and support. I have nothing but fond memories of our time and nothing but my deepest gratitude to Irene Battisti, Koen Bastiaans, Doohee Cho, Maarten Leeuwenhoek, Damianos Chatzopoulos, Tjerk Benschop, Vincent Stalman, Jacky Ge, Jinwon Lee, Jiasen Niu, Amber Mozes, and Maialen Ortego. In the last year I had the pleasure to work again with Kaveh Lahabi on the hydrodynamics project showing me your infinite capacity for kindness and support. It's amazing to think this all started 6 years ago when I set foot in your lab as a BSc student. I also had the opportunity to supervise some great students during my PhD. Amber Vervloet, Evert Stolte, Thijs van Stralen, Jasper Steenbergen, Marijn van der Horst, and Ilse Kuijf. I can only hope you enjoyed our time as much as I have.

Over the course of my PhD I got to know some wonderful people who made LION into a wonderful place to be. A special thanks to Kaveh Lahabi, Tobias de Jong, Martin de Wit, Freek Hoekstra, Tim Fuchs, Norman Blümel, Jimi de Haan, Remko Fermin, Peter Neu, Guido Stam, Corné Koks and Sergi Campos Jara for bringing the institute to life. I would also like to thank Jelle, Freek, Auke, Lina, and Joël for setting the PhD experience to music.

Tenslotte wil ik mijn familie bedanken voor hun grenzeloze liefde en ondersteuning. Pa, Ma, Jan, ik mag me gelukkig prijzen met zulke geweldig ouders en broer op wie ik altijd kan rekenen.

Curriculum Vitae

Willem Olivier Tromp

Born on 13 September 1994 in Hilversum, The Netherlands

2006 – 2012 Highschool

Sint-Maartenscollege, Maastricht, The Netherlands

2012 – 2016 BSc. in Physics and Astronomy

Universiteit Leiden, The Netherlands

Thesis: “Confinement effects in triplet superconducting systems”
under supervision of Prof. dr. J. Aarts

2016 – 2018 MSc. in Experimental Physics, Quantum Matter and Optics

Universiteit Leiden, The Netherlands

Thesis: “Laser ARPES study of the thickness-dependent electronic
structure of LaNiO_3 thin films” at Université de Genève under
supervision of Prof. dr. F. Baumberger

Thesis: “Quasi-particle Interference in Sr_2RhO_4 ” under
supervision of dr. M.P. Allan

2018 – 2022 PhD in Physics

Universiteit Leiden, The Netherlands

Thesis: “*Nano-scale electronic structure of strongly correlated electron
systems*” under supervision of dr. M.P. Allan

List of Publications

1. Edoardo Cappelli, Willem O. Tromp, Siobhan McKeown Walker, Anna Tamai, Marta Gilbert, Felix Baumberger and Flavio Y. Bruno, *A laser-ARPES study of LaNiO_3 thin films grown by sputter deposition*, *APL Materials* **8**, 051102 (2020).
2. Irene Battisti, Willem O. Tromp, Sara Riccò, Robin S. Perry, Andrew P. Mackenzie, Anna Tamai, Felix Baumberger and Milan P. Allan, *Direct Comparison of ARPES, STM, and quantum oscillation data for band structure determination in Sr_2RhO_4* , *npj Quantum Materials* **5**:91 (2020).
3. Koen M. Bastiaans, Damianos Chatzopoulos, Jian-Feng Ge, Doohee Cho, Willem O. Tromp, Jan M. van Ruitenbeek, Mark H. Fischer, Pieter J. de Visser, David J. Thoen, Eduard F.C. Driessen, Teunis M. Klapwijk and Milan P. Allan, *Direct evidence for Cooper pairing without spectral gap in a disordered superconductor above T_c* , *Science* **347**, 608-611 (2021)
4. Willem O. Tromp*, Tjerk Benschop*, Jian-Feng Ge, Irene Battisti, Koen M. Bastiaans, Damianos Chatzopoulos, Amber Vervloet, Steef Smit, Erik van Heumen, Mark S. Golden, Yingkai Huang, Takeshi Kondo, Yi Yin, Jennifer E. Hoffman, Miguel Antonio Sulangi, Jan Zaanen and Milan P. Allan, *Puddle formation, Persistent gaps, and non-mean-field breakdown of superconductivity in overdoped $(\text{Pb,Bi})_2\text{Sr}_2\text{CuO}_{6+\delta}$* , accepted in *Nature Materials*, arXiv:2005.09740 (2022)
5. Jian-Feng Ge, Koen M. Bastiaans, Damianos Chatzopoulos, Doohee Cho, Willem O. Tromp, Tjerk Benschop, Jiasen Niu, Genda Gu and Milan P. Allan, *Determination of the charge transfer when tunneling into putative Majorana modes in individual vortices in $\text{FeTe}_{0.55}\text{Se}_{0.45}$* under review, arXiv: 2205.10346 (2022)
6. Willem O. Tromp, Ilse Kuijff, Yingkai Huang, Mark S. Golden, and Milan P. Allan, *Quasi-particle interference in overdoped $(\text{Pb,Bi})_2\text{Sr}_2\text{CuO}_{6+\delta}$: Application of noise suppression through self-supervised machine learning*, in preparation

* These authors contributed equally

